Surgical Instruments based on Flexible Micro-Electronics

TECHNISCHE UNIVERSITÄT
CHEMNITZ

Leibniz-Institut
für Festkörper- und
Werkstoffforschung
Dresden

IFW

ABSTRACT

This dissertation explores strategies to create micro-scale tools with integrated electronic and mechanical functionalities. Recently developed approaches to control the shape of flexible micro-structures are employed to fabricate micro-electronic instruments that embed components for sensing and actuation, aiming to expand the toolkit of minimally invasive surgery. This thesis proposes two distinct types of devices that might expand the boundaries of modern surgical interventions and enable new bio-medical applications.

First, an electronically integrated micro-catheter is developed. Electronic components for sensing and actuation are embedded into the catheter wall through an alternative fabrication paradigm that takes advantage of a self-rolling polymeric thin-film system. With a diameter of only 0.1 mm, the catheter is capable of delivering fluids in a highly targeted fashion, comprises actuated opposing digits for the efficient manipulation of microscopic objects, and a magnetic sensor for navigation. Employing a specially conceived approach for position tracking, navigation with a high resolution below 0.1 mm is achieved. The fundamental functionalities and mechanical properties of this instrument are evaluated in artificial model environments and *ex vivo* tissues. The second development explores reshapeable micro-electronic devices. These systems integrate conductive polymer actuators and strain or magnetic sensors to adjust their shape through feedback-driven closed loop control and mechanically interact with their environment. Due to their inherent flexibility and integrated sensory capabilities, these devices are well suited to interface with and manipulate sensitive biological tissues, as demonstrated with an *ex vivo* nerve bundle, and may facilitate new interventions in neural surgery.

TABLE OF CONTENTS

LIST OF ABBREVIATIONS

2D	two-dimensional	**HG**	hydrogel
3D	three-dimensional	**IPMC**	ionic polymer-metal composite
AA	acrylic acid	**ISAC**	integrated self-assembled catheter
ACF	anisotropic conductive film		
ADC	analog-to-digital converter	**MC**	methylcellulose
aFM	antiferromagnetic	**MIS**	minimally invasive surgery
AFM	atomic force microscopy	**MOKE**	magneto-optic Kerr effect
a-IGZO	amorphous indium gallium zinc oxide	**OP**	output
		PAA	polyacrylic acid
ALD	atomic layer deposition	**PBS**	phosphate buffered saline
AM	active-matrix	**PCB**	printed circuit board
AMR	anisotropic magnetoresistance	**PI**	polyimide
BP	barber pole	**PID**	proportional-integral-derivative
CP	conductive polymer	**PMMA**	polymethacrylate acid
CV	cyclic voltammetry	**PPy**	polypyrrole
DAC	digital-to-analog converter	**PR**	Photoresist
DBS	dodecylbenzene sulfonate	**r.m.s.**	root mean square
DC	direct current	**RAMS**	robot-assisted microsurgery
DOF	degrees-of-freedom	**RF**	radio frequency
EAP	electro-active polymer	**RIE**	reactive ion etching
e-beam	electron beam	**RMED**	reshapeable micro-electronic device
EMT	electromagnetic tracking		
e-skin	electronic skin	**SD**	standard deviation
FB	feedback	**SG**	strain gauge
FE	flexible electronics	**SL**	sacrificial layer
FG	field generator	**SMU**	source-measure-unit
FM	ferromagnetic	**SNR**	signal-to-noise ratio
GF	gauge factor	**SP**	setpoint
GMR	giant magnetoresistance	**SVMS**	spin valve magnetic sensors
GSSG	gold stripe strain gage	**TFT**	thin-film transistor
GUI	graphical user interface	**US**	ultrasound

1 INTRODUCTION

Minimally invasive surgery (MIS) plays a decisive role in the ongoing effort to improve the life expectancies and well-beings of patients through modern healthcare[1]. Emerging materials and manufacturing strategies can contribute to the development of novel surgical instruments that will enable increasingly safer and more effective medical interventions.

1.1 MOTIVATION

Medical interventions have been aimed to prevent death, to terminate illness, pain, or suffering, or to improve well-being, among other goals, since the dawn of medicine in pre-historic times. Medical practitioners needed to weight up the expected benefit against the involved side effects and risks before carrying out any intervention at all times. Among the earliest recorded surgical interventions, for instance, we find the treatment of wounds[2] and injured limbs[3]. To avert the severe risk of deadly infections, fractured skull bones (Figure **1.1**a) were surgically treated and injured limbs were amputated (Figure **1.1**b), even long before the invention of effective sterilization methods or anesthetics. These procedures carried a significant risk to the life of the patient and were immeasurably painful, in the best of cases. Hence, only the most threatening conditions were treated. Throughout the past centuries, progress in various fields, including anatomy, physiology, pharmacy, bio-chemistry, material science, and engineering, succeeded to shift the risk-benefit balance of a variety of medical interventions[4]. Today (Figure **1.1**c), highly effective low-risk procedures are available to treat various conditions, even those which are not immanently life-threatening, and contribute to rising life expectancies in the developed world, improving the well-being of patients into an old age. This trend is expected to continue into the future, where upcoming technologies might support medical practitioners during diagnostics and therapy (Figure **1.1**d). Key drivers of shifting the balance between risk and benefit are the tools that enable minimally invasive surgical interventions. Instruments such as catheters or robotic micro-surgery systems allow to greatly minimize the trauma inflicted on healthy tissue and thereby reduce recovery times and the risk of complications[5–7]. Especially when reaching out towards the smallest and most intricate anatomies within the human body, micro-sized surgical tools such as tubes, rods, and wires, extend the reach of surgeons. Although each decade seems to offer novel and exciting minimally invasive treatments, several

challenges persist till today. One key difficulty is the perceptual gap between the surgeon and the site of operation[8]. Whereas medical practitioners can see and feel targeted tissues during classical interventions, these paths of observation are obstructed during keyhole surgeries. Surgical tools with embedded electronics, in tandem with data processing and visualization software, can provide supporting visual or haptic information. However, the demand for small-scale tools makes it increasingly difficult to integrate these electronic components at the micro-scale. Even modern electronically enhanced instruments, due to their size or rigidity, cannot operate in the smallest and most remote regions of the human body, or carefully interface with soft and sensitive tissues. A second challenge is the control and usage of surgical instruments at very small scales. Purely mechanical solutions relying e.g. on pull-wires[9,10], as they are successfully used in conventional large-scale devices, do not apply readily at the micro-scale. A radically new generation of surgical instruments is required to address these challenges and conquer the remaining frontiers within the human body in the context of MIS.
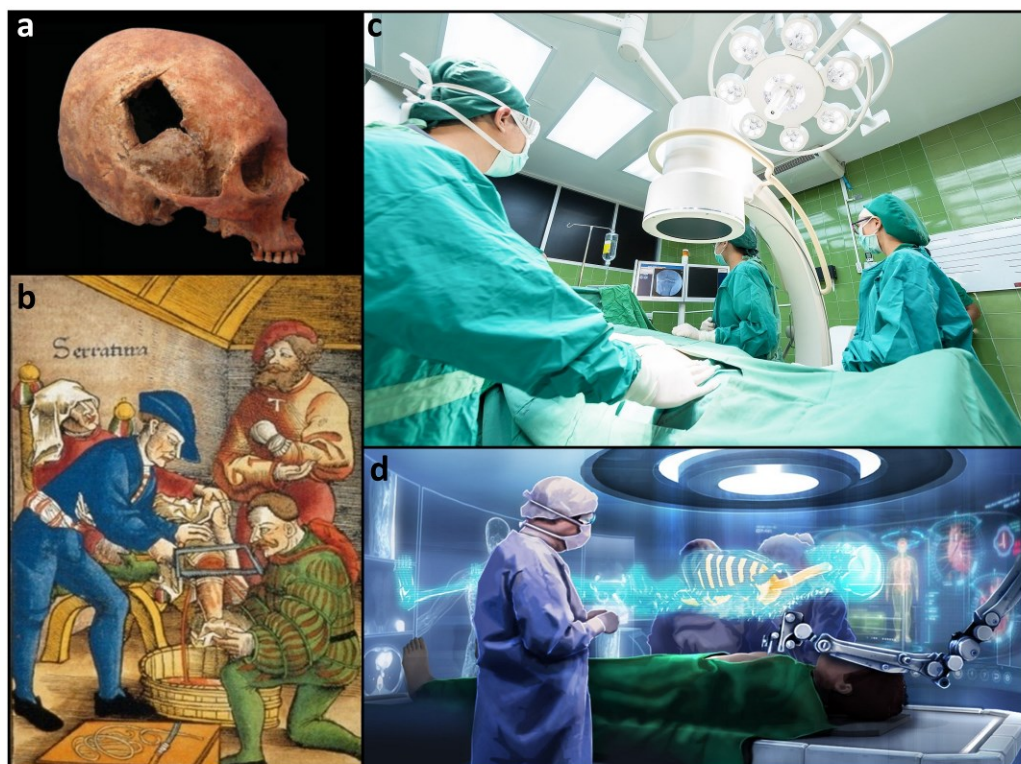
Figure 1.1: Timeline of surgery: (a) A piece of skull bone was surgically removed. Reproduced with permission from John Wiley and Sons[11]. **(b)** A medieval surgeon amputates a limb. Image courtesy of the Reynolds-Finley Historical Library[12]. **(c)** Modern day surgeons work in a sterile environment and use tools for diagnostics, such as medical imaging. Image courtesy of Sasin Tipchai. **(d)** Futuristic vision of a surgeon supervising robotic surgery, having access to comprehensive real time diagnostics. Image courtesy of Brother Ltd.[13].

New technologies based on *flexible electronics* (FE)[14–16] might give rise to this new generation of surgical instruments. FE, which has emerged as a research field at the interface between electronics and polymer chemistry, is envisioned to decisively contribute to modern healthcare. The first bio-medical applications, flexible and compliant skin patches, show promising results for physiological monitoring and might contribute to decentralized and personalized healthcare[17–19]. Related developments aim at soft electronic implants that are placed permanently within a patient, where they cause less disruption and trauma compared to their rigid counterparts[20–22]. Since flexible electronic devices can seamlessly comply not only to biological anatomies, but also artificial structures, they have been applied onto conventional surgical instruments to enhance them with electronic functionalities. This approach allowed to bridge the gap between the requirements of planar electronics fabrication, and three-dimensional (3D), mechanically functional tools. Surgical instruments such as catheters or robotic tools can now be engineered to monitor their environment and offer insights to their operator[23,24]. To prolong the progress of MIS, however, a new generation of tools with ever decreasing sizes, yet increasing complexity, will be required. Conventional fabrication and manufacturing strategies are reaching their limits to further improve surgical instruments. Intelligent and adaptive small-scale tools with higher integration density and wider sets of functionalities must be rooted in novel device concepts and fabrication paradigms.

Recent years have witnessed the development of novel strategies that allow to create complex 3D shapes and structures at the micro-scale through *self-assembly*. To this end, specialized material systems including organic and inorganic substances, rigid and soft, are processed in planar on wafer substrates to subsequently undergo a deterministic shape transformation such as folding[25], buckling[26], or rolling[27,28], to name a few. For the first time since the revolutionary development of micro-electronics, numerous electronic components were freed from their two-dimensional (2D) manufacturing constrains and extend into the third dimension through efficient monolithic wafer-scale processes.

While traditional small-scale surgical instruments fulfill mechanical functionalities, but lack electronic capabilities, the opposite is true for flexible and self-assembled 3D electronics. The application of micro-scale actuation and self-assembly approaches onto flexible electronic devices can provide them with useful mechanical properties and make

them suitable for usage as electronically integrated, small-scale instruments for bio-medical interventions.

1.2 OBJECTIVES AND STRUCTURE OF THIS DISSERTATION

This thesis explores the possibilities offered by emerging material systems to develop electronically integrated micro-scale instruments for MIS. The integration of established technologies for actuation and sensing onto novel flexible platforms creates mechanically and electronically functional devices. A key aspect of this integration effort is the identification of compatible materials and processing techniques, as well as suitable strategies for device operation. In this work, two distinct types of devices are developed. First, a new type of electronically **i**ntegrated **s**elf-**a**ssembled micro-**c**atheter (ISAC) is discussed. ISACs are tubular devices that are based on the self-rolling shapeable polymer stack. Therefore, the first objective is to define a suitable device geometry and to adapt the design of the planar polymer stack to achieve the desired form. ISACs are expected to carry out conventional tasks of catheters, as well as offer new functionalities through integrated electronic components. To this end, electronic components that enable actuation and navigation are selected, adapted, and integrated into the self-rolling platform, creating devices with closely intertwined geometries and functionalities. The deviation from the conventional component designs regarding size, composition, and geometry, which was imposed by the system integration, requires the formulation of suitable modes of operation. The performance of individual functionalities is then evaluated under appropriate conditions using artificial and natural models. The second development is centered around **r**e-shapeable **m**icro-**e**lectronic **d**evices (RMEDs). Aiming to introduce directly controlled actuation to FE at the micro-scale requires the identification and adaptation of appropriate material systems, including mechanically active and passive polymers. Feedback-driven shape control is a desired feature for such potential micro-robotic systems that has not been available previously. The next objective thus comprises the integration of suitable sensors, enabling RMEDs to carry out tasks without supervision. The integration effort strongly relies on the incorporation of compatible material systems, processing techniques, and an optimized design to prevent interference between components. Finally, the operation of these systems requires the development of appropriate hardware and software, enabling versatile manual and procedural control through the implementation of algorithms, and their evaluation. This dissertation is structured as follows:

Chapter 2 introduces instruments that enable modern MIS, and the potential contributions offered by flexible electronics. Moreover, the chapter discusses the state-of-the-art of shapeable and self-assembling electronics based on the shapeable polymer stack, as well as actuation and sensor technologies employed throughout this thesis.

Chapter 3 provides a detailed introduction into the recently developed materials, as well as the diverse set of additive and subtractive thin-film processing techniques that are involved in the fabrication of the herein reported technologies.

Chapter 4 highlights the development of ISACs. After their design and functionalities are introduced, their performance is evaluated in artificial model environments and *ex vivo* tissue.

Chapter 5 is devoted to the development and evaluation of RMEDs. The chapter highlights the design considerations and optimization of these micro-systems and demonstrates feedback-driven shape control of soft micro-scale devices. Moreover, the heterogeneous integration of active electronic components and soft micro-actuators is demonstrated.

This dissertation is concluded with the **Theses**, which recapitulate the scientific insights gained throughout this work.

2 BACKGROUND

This dissertation attempts to introduce surgical micro-scale instruments based on self-shaping flexible material systems, aiming to expand the toolkit of medical practitioners. The development of such tools requires an understanding of currently available devices and their limitations to evaluate the potential contribution of emerging technologies. This chapter lays down the background of this interdisciplinary development. Section 2.1 provides a brief review of established instruments for MIS, namely vascular catheters and robotic micro-surgery systems, and outlines trends to enhance these tools with electronic capabilities using flexible electronics. Section 2.2 highlights modern approaches towards the creation of 3D electronic devices at the micro-scale through the integration of stimuli responsive materials, as well as actuation technologies that are applicable at small scales. As the instruments developed in this work rely on sensors to monitor their position or shape, related technologies are introduced in Section 2.3.

2.1 TOOLS FOR MINIMALLY INVASIVE SURGERY

Several types of surgical interventions have been established during the 20th century and are now collectively known as MIS. MIS can target almost all body parts, including the treatment of cardio-vascular diseases, treatment of microscopic nerve bundles, and interventions within the abdomen, thorax, and brain[29–31]. When compared to classical open surgeries, MIS can be just as, or more effective[5–7]. The reduced trauma that is inflicted on healthy tissue reduces pain and shortens recovery time. In some cases, MIS can be carried out preemptively to investigate or treat potentially threatening conditions, such as colon cancer screenings or embolizations of non-ruptured aneurysms[32], where open surgery would be discarded for its higher risk and substantial tissue damage.

The overwhelming success of MIS decisively depends on the toolkit of surgeons and medical practitioners. The following sections will briefly introduce two important categories, i.e. catheters and robotic micro-surgery systems, and provide a glimpse into upcoming developments in these fields that are driven by the emergence of flexible electronics.

2.1.1 CATHETERS

Catheters are tubes that are introduced through natural or artificial orifices into a patient's body, allowing access for drug injection, diagnostics and treatment, biopsies, or the delivery of implants, with minimal damage to healthy tissue[31,33–35]. Catheter procedures are carried out in a variety of vessel systems and cavities, including the gastro-intestinal tract, the urinary tract, the uterus, or the respiratory system. In the cardio-vascular and cerebro-vascular systems, minimally invasive catheter interventions are especially attractive due to the facile and relatively safe access through blood vessels that serve as natural channels. Catheters can be introduced into major arteries or veins and advanced through the blood vessel towards the heart or brain, two regions where classical open surgery is highly invasive and risky. While preceding studies laid down a foundation using animal models, the first human heart catheterization was carried out by Werner Forßmann on himself in 1929 using a regular rubber tube[36]. Since then, a plethora of vascular catheters was developed with different sizes and shapes, as displayed in Figure **2.1**a and Figure **2.1**b, to enable a variety of interventions: Tools such as wires, coils, or meshes can be introduced to retrieve blood clots (Figure **2.1**c); Platinum coils or liquids are delivered into aneurysms such that the subsequent embolization reduces the risk of rupturing; And balloon catheters are applied to widen constricted vessel and expand stents (Figure **2.1**d). Maneuvering catheters through the intricate blood vessel network of the human body is a challenging task. Traditional approaches to steer the tip of catheters towards the desired direction include guidewires and pull-wire systems[9,10], while recently developed and commercialized systems can employ magnetic fields[37–39]. Catheters are available with different mechanical properties and sizes, and need to be selected based on the targeted part of the vascular system and the task. Small vessels, e.g. inside the brain, are normally accessed with the smallest instruments, so-called micro-catheters, that have sizes above 0.45 mm or 1.5 Fr (1 Fr = $\frac{1}{3}$ mm)[40]. The biggest blood vessels and cavities, such as the vena cava, the aorta, and heart chambers, can be accessed with bigger catheters. For instance, cardiac arrythmia can be treated through radio-frequency (RF) ablation, which is carried out using electronically integrated catheters with diameters around 9 Fr (3 mm). These devices (Figure **2.1**e) offer sufficient space to accommodate electronic components for RF ablation, as well as sensors that assess contact with tissue, impedance, electrophysiological properties of heart tissue, and the position and orientation of the catheter tip[41,42]. This electronic integration makes

such modern catheters highly potent tools within their area of operation by allowing simultaneous anatomic and electrophysiological measurements[43]. Surgeons are provided detailed information about diseased tissue fast and *in situ*, enabling them to make better decisions, preserve healthy tissue, and reduce operation time. Other catheter interventions targeting areas that are accessed through smaller and more delicate vessels would benefit from electronically integrated catheters in multiple ways. However, current manufacturing strategies are not suitable to create electronically integrated instruments with the desired small sizes and flexibility.
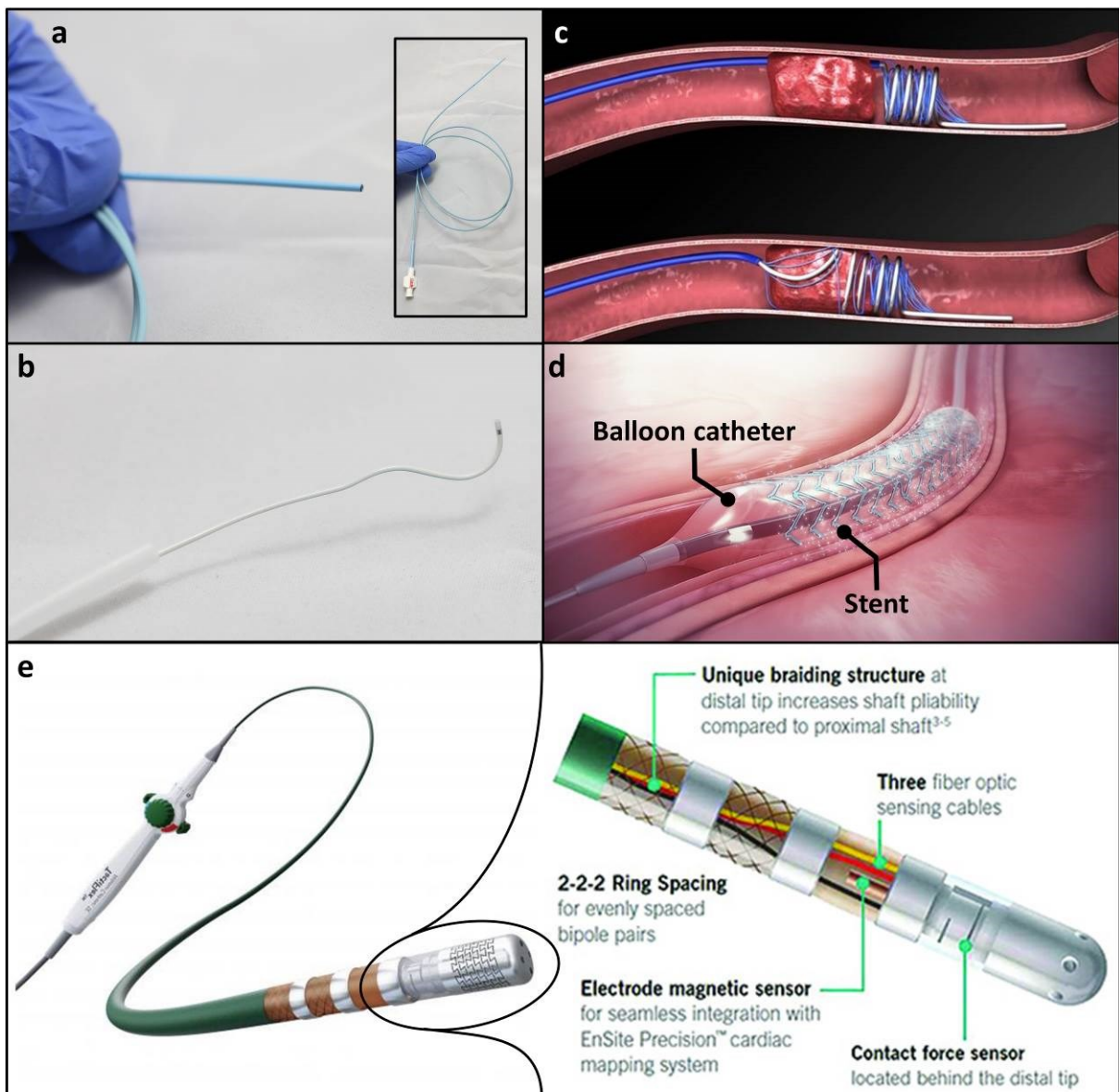
Figure 2.1: Conventional catheters and their applications: (a) A clinical 4 Fr (ø 1.6 mm) vascular catheter. **(b)** A 2 Fr (ø 0.8 mm) micro-catheter. **(c)** Retrieval of blood clots using a catheter. Image by Neilbarman[44]. **(d)** Placement of a stent. Image by Scientific Animations[45]. **(e)** An electronically integrated and steerable catheter for coronary ablation, including various functionalities. Image courtesy of Abbott Laboratories[46].

15

One key functionality that is offered by catheters with integrated electronics is position tracking and navigation[47–50]. State-of-the-art vascular catheter interventions generally rely on fluoroscopy for navigation, a medical imaging technique based on x-rays. Fluoroscopy informs the surgeon about the location of tools within the patient quickly and accurately, and can even indicate blood flow when a contrast agent is injected. The repeated exposure to ionizing radiating, however, imposes a significant health liability on patients and medical personnel. Thus, alternative strategies that are not based on harmful agents are highly sought-after. Magnetic or electromagnetic tracking (MT or EMT) is an established approach to achieve real time tracking without the need for harmful radiation or contrast agents[51,52]. Instead, magnetic or inductive sensors are attached to the medical tool to measure an alternating or static reference magnetic field. The reference field is emitted by a field generator (FG) and thus has a known distribution in time and space. The picked-up electromagnetic signals are then used to reconstruct the 3D position and orientation of the medical tool with up to six degrees-of-freedom (DOF) with below-millimeter precision. This approach was applied using pick-up coils to detect magnetic reference fields and track instruments such as biopsy needles[53] or bulky ablation catheters[35]. Despite the appealing properties of EMT, however, the required sensors have prohibitively big sizes[54] and established applications are limited to big vessels or the heart chambers. New materials, technologies and manufacturing strategies need to be developed to integrated small scale catheters with electronic functionalities that will offer diverse methods for physical and physiological sensing, navigation, and interaction with tissue.

2.1.2 TOOLS FOR ROBOTIC MICRO-SURGERY

Another important category within MIS is robot-assisted microsurgery (RAMS). In RAMS, surgical small-scale tools including grippers (forceps), knifes, and clamps are not operated directly by the surgeon, but attached to robotic arms (Figure **2.2**a)[55]. The procedure is usually monitored with an endoscopic high-resolution microscope camera and displayed at a console, from where a surgeon controls the robotic system (Figure **2.2**b). Downsizing the surgical tools allows to interact with smaller structures, e.g. connect small vessels with sizes of about 2 mm[56]. The surgical tools are mechanically coupled with wires to external actuators, through which they are controlled with superhuman dexterity. The compact arrangement of robotic arms allows to insert multiple tools inside a patient in a laparoscopic or key-hole manner, i.e. through a single

small opening, thereby minimizing tissue damage, scar formation, and recovery time. These benefits to patients come at the cost of new challenges for the medical operator. In classical surgery, surgeons rely on their senses to assess the mechanical response of tissue and regulate the applied forces and pressures correspondingly. This direct feedback is not available when using robotic surgical systems and this shortcoming is regarded as one of the key challenges concerning RAMS[57]. Efforts were directed towards the integration of force and slip sensors to provide haptic feedback. Given the small scale of these tools, however, the attachment of sensing components only adds to the manufacturing complexity, impedes the further miniaturization of these systems, and ultimately further increase the already high cost for acquisition and maintenance. Novel robotic small-scale surgical tools that naturally provide feedback through integrated sensors could decisively contribute to the field, advance the possibilities offered by RAMS and further improve medical treatment.
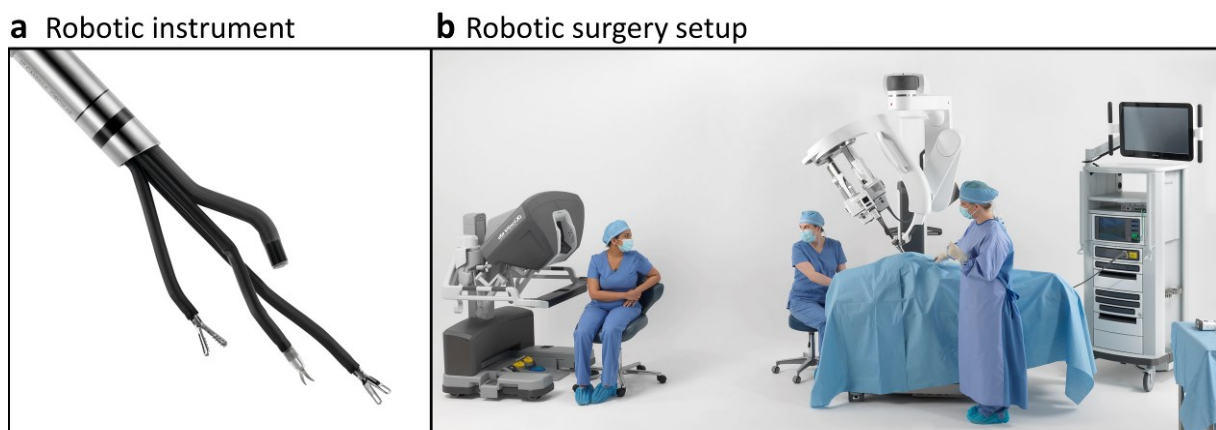
Figure 2.2: System for robot-assisted microsurgery: (a) An endoscopic tool for keyhole micro-surgery with three tools and a camera. **(b)** The *DaVinci Xi* robotic surgery system comprises a control panel for the surgeon, a control tower, and a robotic system with multiple remote-controlled tools. Images curtesy of ©2021 Intuitive Surgical, Inc.[58]

An intriguing application for RAMS is the treatment of small-scale nerve bundles[59], leading to the repair of injured tissues, or the placement of implants for neural interfacing. Nerves are amongst the softest and most sensitive tissues within the human body. During surgical interventions, the mismatch between the stiffness of surgical tools and treated tissue can lead to unintended damage[60,61]. Moreover, nerve bundles can suffer permanent damage from excessive pressure, where ~1300 Pa are considered as limit for safe handling[62]. Addressing these limitations requires micro-scale surgical tools that are suitable to manipulate nerve bundles, have smaller stiffness than conventional tools (e.g. about 20 MPa)[63], and offer mechanisms that prohibit the application of excessive force. While conventional materials used for surgical tools, e.g. steel, are too hard to carefully

interface with soft and sensitive tissues, polymers are promising to develop such tools. For this purpose, however, flexible polymer structures need to be equipped with actuators for shape control, and ideally further electronic components to monitor their performance and offer additional insights. Since conventional electronic components rely on flat and rigid supports and require bulky and redundant packaging, they are not readily incorporated onto flexible or small-scale instruments. This challenge must be addressed through alternative formulations of electronics.

2.1.3 FLEXIBLE ELECTRONICS FOR SMART SURGICAL TOOLS

Conventional electronics are carried by flat and rigid substrates, such as semi-conductor wafers (Si, GaAs, etc.) or printed circuit boards (PCBs). In contrast, the field of FE emerged to develop electronic components and entire circuits that are carried by flexible substrates. A wide array of insulating substrates, such as paper[64–66] and various polymers[67–69], serve as platforms for electronic devices based on thin-film metals, semi-conductors and dielectrics[70], carbon nanotubes[71], and organic semi-conductors[15]. Applying standard fabrication techniques such as photolithography, printing, physical and chemical vapor deposition, and wet and dry etching, a diverse array of passive and active electronic components has been realized, including conductor traces[72], resistors[70], capacitors and inductances[21,73], diodes[74], and transistors[15,22,70]. These were combined into complex, integrated electronic systems, for instance a natively flexible 32-bit ARM microprocessor[75] (Figure **2.3**a), organic light emitting diode displays[76], artificial electronic skins for smart prosthetics[14], or winged micro-fliers[77] (Figure **2.3**b). FEs are robust, extremely light-weight, and have the unique ability to comply to irregular geometries. This makes them particularly attractive for bio-electronic interfaces, as they can adapt seamlessly to complex anatomies while causing little discomfort or irritation. Flexible polymer foils that are equipped with sensors can be used as on-skin patches[78], or even smart lenses[79] (Figure **2.3**c), which monitor physiological parameters (temperature, heart rate, breathing) or chemical markers. Electronic skins (e-skins) with e.g. magnetic sensors as displayed in Figure **2.3**d offer a super-human sense of magneto-perception[15,80], which is useful in augmented and virtual reality applications. And flexible ultrasound (US) transducer arrays (Figure **2.3**e) are investigated for cardiac monitoring[81,82].
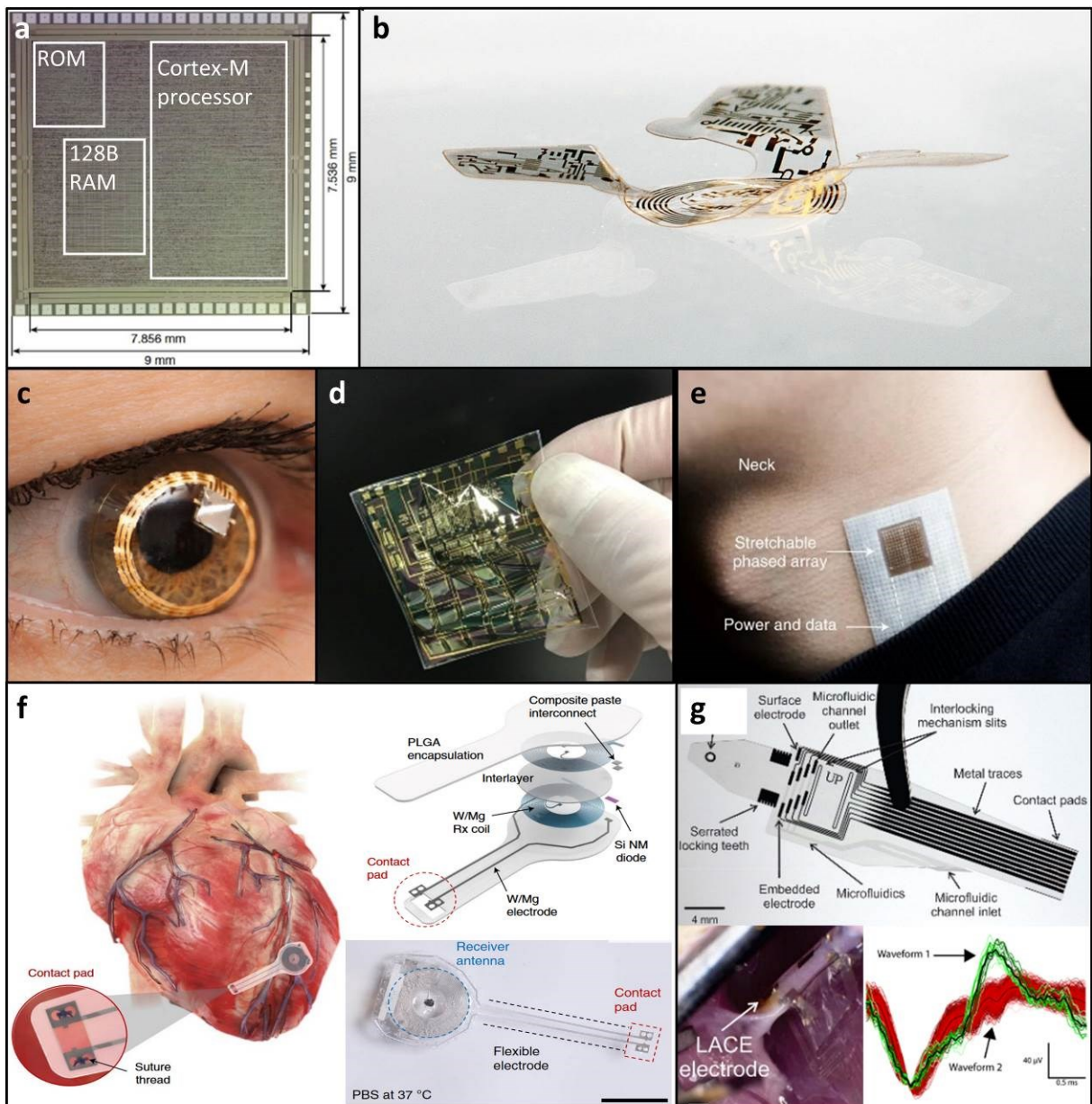
Figure 2.3: Review on flexible electronics: (a) First natively flexible ARM microprocessor[75]. Reproduced with permission from Springer Nature. **(b)** A 3D shaped winged flier with integrated sensors for environmental monitoring. Image courtesy of Northwestern University[83]. **(c)** The Triggerfish (Sensimed, Switzerland) smart contact lens to monitor intraocular pressure[84]. Reproduced with permission from Elsevier. **(d)** Imperceptible e-skin with magnetic sensors[15]. **(e)** Skin patch with a 12 by 12 matrix of US transducers[82]. Reproduced with permission from Springer Nature. **(f)** Bio-degradable and wireless pacemaker to support post-surgical recovery[22]. Scale bar indicates 10 mm. Reproduced with permission from Springer Nature. **(g)** Neural cuff implants can be attached to peripheral nerves bundles and record neuronal signals.[20] Reproduced with permission from IEEE.

Just as for on-skin patches, flexible electronic devices are well suited as internal implants due to their softness, compactness, and compliance. Surgeons can apply ultra-thin devices for sensing, stimulation, and even micro-fluidic drug delivery onto the surface of organs or wrap it around cylindrical structures. For instance, a fully bio-resorbable temporary pacemaker[22] has been proposed to support patients recovering from heart surgery

(Figure **2.3**f). The device is applied on the surface of the human hearth, where it determines the pulse using wireless control and power supply, and then decomposes into bio-compatible products, removing the need for a secondary surgery. Targeting the neural system, cuff implants[20,85] can be wrapped around peripheral nerve bundles for signal monitoring or stimulation (Figure **2.3**g). Recorded neuronal signals can then be used for diagnostics or to control prosthetics. Moreover, cuff-implants can apply stimuli to bypass damaged sections of a nerve and allow patients to again use their otherwise healthy body parts. To serve such purposes, an intimate contact between the neuronal tissue and the implanted electronics is critically important. Surgeons apply cuff implants to peripheral nerve bundles down to a size of about 1 mm. These procedures are technically challenging and come with the risk of damaging the soft and sensitive nerve tissue. Often, much of a cuff implant's area does not contribute to the main purpose of sensing or stimulation, but is required for handling and fixation. To improve these devices, flexible neural implants need first to be miniaturized to reduce the rejection reaction of the patients' bodies and to improve compliance with irregular small-scale anatomies. Small-scale (< 1 mm) implants, however, are not easily handled even by the most skillful surgeons. Therefore, this new generation of neural implant must come with a native capability to adjust its shape on demand and should carry additional sensors, which monitor the device shape and ensure an optimal bio-electrical-mechanical interface. The key prerequisite for such devices is a flexible platform that integrates soft micro-actuators and sensors. Related investigations were already initiated in the past[86] and continue in this thesis (Chapter 5).

Apart from implants or on-skin applications, FE is well positioned to provide electronic capabilities to otherwise passive mechanical structures. Integrated FE devices add only little weight, size, and stiffness to an object when applied onto its surface and are therefore attractive for applications that require compact tools. One such category are catheters that are routinely used in MIS. Clinical state-of-the-art catheters are highly engineered to provide optimal mechanical properties, such as the right balance of stiffness and flexibility[87], to navigate the tortuous vessel systems of the human anatomy. In the past decades, multiple lines of research have emerged to supplement these mechanical properties with electronic capabilities. For instance, the Rogers group has developed a variety of electronically integrated balloon catheters[23,88,89]. Their approach is to fabricate advanced flexible and stretchable electronics (Figure **2.4**a) using standard

micro-fabrication techniques, and apply them onto commercial catheters, mostly balloon catheters that have an inflatable section. The modification is carried out manually using adhesives to permanently attach the FE devices to the commercial catheters. This approach has led to the integration of temperature, pressure and blood flow sensors, electrodes for cardiac ablation, light emitting diodes, and on-board multiplexing (Figure **2.4**b-e).
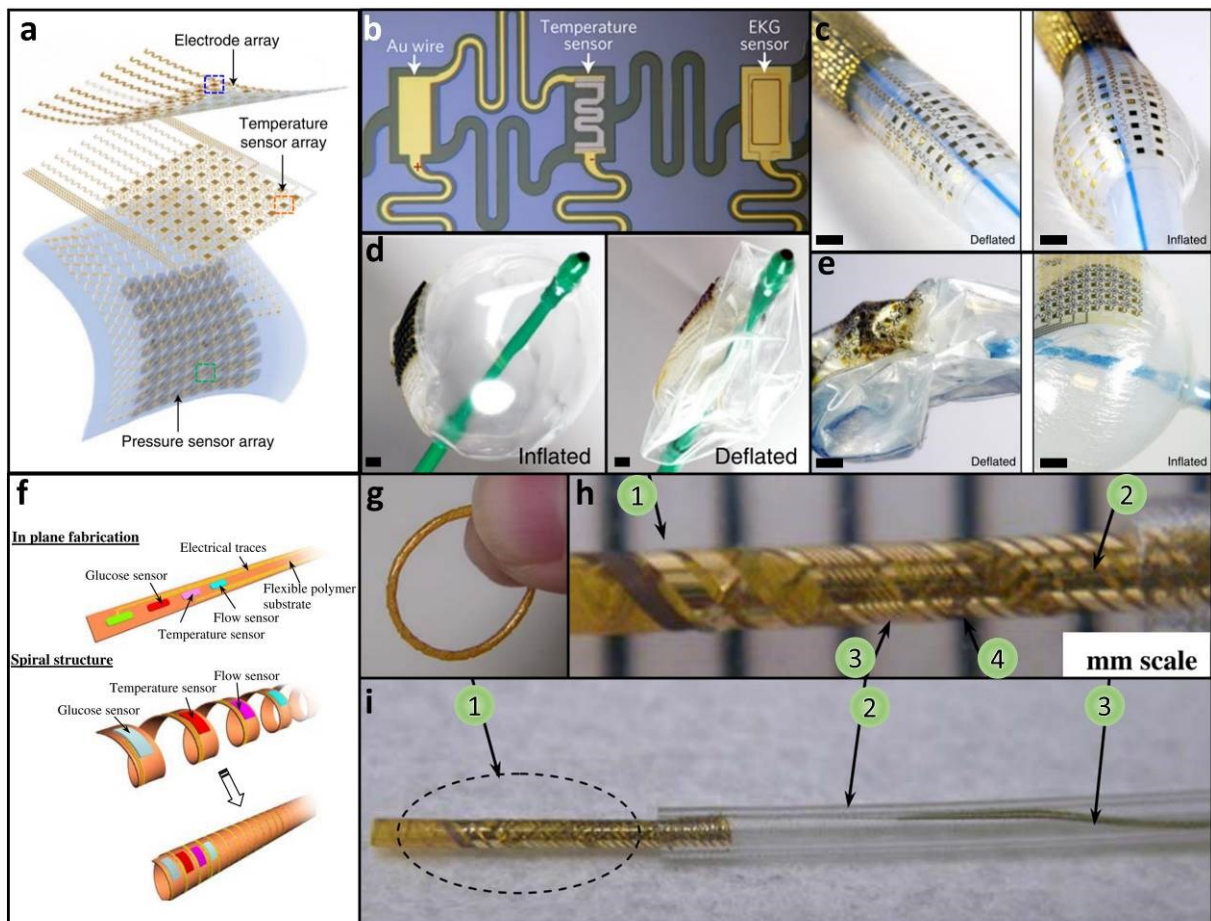
Figure 2.4: Review on electronically integrated catheters: (a) Standard flexible and stretchable electronics are fabricated separately and attached onto commercial balloon catheters[89]. **(b)** Exemplary flexible and stretchable electronic circuit with multiple components that was mounted on a balloon catheter[88]. Following panels display commercial balloon catheters quipped with[89] **(c)** a mounted stretchable ablation electrode array, **(d)** a pressure sensor array, **(e)** with a temperature sensor array, each in in its deflated and inflated state. Scale bars indicate 2 mm. **(f)** Strategy to fabricate integrated catheters based on spiraling assembly of Kapton tape[90]. **(g)** Spiral assembly-based catheter platform. **(h)** Spiral integrated catheter with integrated glucose sensor (1), electrical leads (2), and temperature (3) and flow (4) sensor. **(i)** Spiral integrated catheter (1) connected to silicone tube (2) and electrical cable (3). All images reproduced with permission from Springer Nature.

A similar approach aims at the integration of biosensors, e.g. for glucose and oxygen monitoring, and smaller catheter sizes. Here, sensors were fabricated on top of Kapton tape and spirally wound onto a tubular supporting structure[90,91] (Figure **2.4**f), instead of

using bulky commercial catheters. This manufacturing strategy led to integrated catheters with sizes down to 0.65 mm (Figure **2.4**g-i), integrating sensors to measure temperature, flow, oxygen saturation, and glucose concentration, to name a few.

Despite a number of intriguing demonstrations, these manufacturing strategies come with very clear limitations. The manual production scheme is prone to inaccuracies, not easily scalable to meet a rising demand for healthcare products, and time and cost intensive. Ideally, catheters should be single-use devices to eradicate the risk of pathogen transmission between patients. High prices for medical tools can be prohibitive in this regard and catheters, especially electronically integrated ones, should ideally be batch fabricated at a low cost. Moreover, the requirement for manual assembly imposes a limit on the degree to which these devices can be miniaturized. In fact, no electronically integrated catheter has been previously demonstrated to match the small size of clinical micro-catheters (~ 0.45 mm). Additionally, conventional electronic components need redundant support and packaging to withstand manual handling during assembly, which negatively impacts their flexibility and size, and partially offsets the core benefits of FE. With regard to catheter size, it should be noted that electronically integrated catheters could lead to novel applications, such as intermediate-duration and permanent sensing applications to monitor biomolecules, blood gas, physiological parameters, and even brain signals from within small vessels[92] in a minimally invasive way. Microscopic smart catheters with very small sizes (~ 0.1 mm) might occupy a key role in upcoming applications as they can be installed in microscopic blood vessel (e.g. 0.5 mm) without imposing a critical obstruction to blood flow[93].

In summary, considerable efforts have been made to develop electronically integrated catheters that provide additional functionalities for sensing and treatment. Reported manufacturing strategies rely on the manual assembly of separate FE onto mechanical support structures, which imposes limits on the size, cost, and integration density of realized devices. Regarding the overall prospects of FE in modern healthcare, these devices already facilitate a variety of fascinating applications. Their shape-adaptability, however, cannot be fully utilized as long as the geometric transformations need to be carried out manually. Instead, next generation bio-medical tools based on FE should have the integrated ability to adapt their shape. These shape transformations either need to take place one time to achieve a desired, pre-defined form, or repeatedly and on-demand to serve as flexible robotic micro-tools.

2.2 PLATFORMS FOR SHAPEABLE ELECTRONICS

As discussed in Section 2.1, FE have great potential in applications as small-scale bio-interfaces and surgical tools. These technologies, however, are to date impeded by the requirement for the manual adjustment of their shapes when aiming at smaller scales, both during the fabrication of instruments and the placement of FE devices *in situ*. Already available soft materials that offer intrinsic shape adaptability represent an attractive strategy to achieve shape control in flexible devices. They are introduced in Section 2.2.1. These shape-transforming compounds have been used in the development of self-assembling electronics and soft actuators, which are introduced in Section 2.2.2 and Section 2.2.3, respectively.

2.2.1 SHAPEABLE POLYMER COMPOSITES

Fields such as 3D electronics, micro-robotics, or 3D bio-scaffolds have fueled the requirement for shape-transforming organic and inorganic materials systems and gave rise to the diverse field of shapeable materials technologies. Various mechanisms were investigated that can lead to shape-transformations in flexible material systems, including surface tension[71,94], mechanically guided buckling[95,96], thermal effects[97], intrinsic strain[98–100], shape memory[63,72], or solvent induced swelling[101,102]. Among these, hydrogel polymers that swell in aqueous solvents are attractive since they offer high volumetric strain (50-500 %)[103] and excellent compatibility with standard micro-fabrication techniques. The swelling of polymers in water or other solvents can be sensitive to specific stimuli, such as pH[86,104], temperature[25,105,106], or electric cues[107,108]. Hydrogel swelling generally leads to an isotropic volumetric strain, as seen with gum bears that contain gelatin (Figure **2.5**a), a naturally occurring hydrogel. In contrast, functional platforms require a directed, anisotropic shape transformation such as folding, curving, or rolling. Anisotropic strain can be achieved for instance through heterogeneous integration of materials that develop different strains upon exposure to a stimulus[109,110]. In practice, this means that a swelling material, i.e. the hydrogel, is combined with an inert material that acts as reinforcing layer, as displayed in Figure **2.5**b, resulting in a bending composite. Pinecones naturally take advantage of this mechanism (Figure **2.5**c) to open under dry ambient conditions[111,112]. Layered material systems with two components comprising a swelling hydrogel and an organic or inorganic reinforcing component can be fabricated as planar structure which determine their 3D appearance after transformation, resulting in polyhedral shapes[113,114], 'Swiss-roll'

tubular structures[27,108], and even complex micro-origami[25,115] (Figure **2.5**d), to name a few.
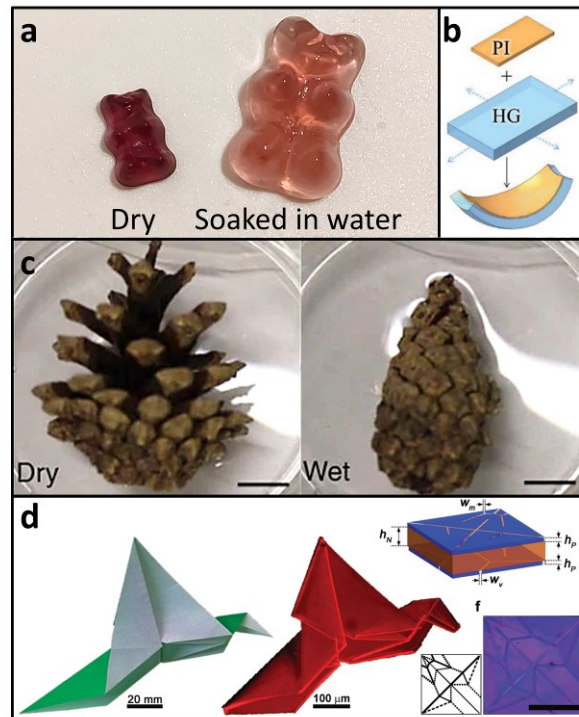

Figure 2.5: Swelling hydrogels in nature and technology: (a) Gum bears contain gelatin that swells in water. **(b)** Volumetric strain is converted to a bending shape change in a composite comprising a swelling hydrogel (HG) and non-swelling polyimide (PI) layer.[116] **(c)** Pinecones open and close, depending on ambient moisture[111]. Reproduced with permission from Springer Nature. **(d)** Strategically distributed hinges enable self-folding of complex shapes from planar layer stacks, forming e.g. a micro-scale origami crane[25]. Reproduced with permission from John Wiley and Sons.

Curving composites with swelling and non-swelling layers take on deterministic shapes when strain is induced. The curvature radius of the final geometry depends on the properties of the involved layers, specifically their thicknesses, Young's moduli, and the induced strain. The curvature of a bending multi-layer material stack can be estimated through geometric and mechanical considerations. As detailed in available literature, e.g. discussed by Christophersen et al.[117], it should be firstly noted that any bent multi-layer will experience, purely as a geometric effect, a bending strain as indicated in Figure **2.6**

$$\varepsilon_b(z) = \varepsilon_0 + \frac{z}{R} = \varepsilon_0 + z \cdot \kappa \qquad \text{Eq. 2.1}$$

where $\varepsilon_b(z)$ is defined as the strain at distance z from the bottom plane at $z = 0$, ε_0 is the strain at this reference surface, and $R = \kappa^{-1}$ are the curvature radius and curvature, respectively.
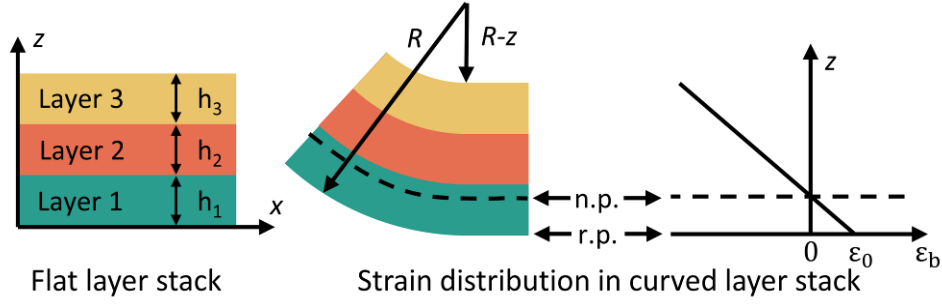
Figure 2.6: Modelling of bending multi-layer systems: The strain in a bending multi-layer equals zero in the neutral plane (n.p.) and changes linearly with distance, being compressive on one and tensile on the other side. The reference plane (r.p.) is defined at $z = 0$.

When one or multiple of the layers expand or shrink, additional strain occurs and Equation 2.1 needs to be expanded by the expansion strain α, which is different for each of the $1 \leq i \leq N$ layers

$$\varepsilon_b(z) = \varepsilon_0 + \frac{z}{R} = \varepsilon_0 + z \cdot \kappa - \alpha(z) \qquad \text{Eq. 2.2}$$

In the case of a freely bending multi-layer, i.e. without external constrains, all forces F and moments M must be zero, thus

$$F = \int_0^h \sigma(z)\,dz = \int_0^h E(z)\left[(\varepsilon_0 + z \cdot \kappa) - \alpha(z)\right]\,dz = 0 \qquad \text{Eq. 2.3}$$

$$M = \int_0^h z \cdot \sigma(z)\,dz = \int_0^h z \cdot E(z)\left[(\varepsilon_0 + z \cdot \kappa) - \alpha(z)\right]dz = 0 \qquad \text{Eq. 2.4}$$

where $E(z)$ and $\alpha(z)$ are constant in sections to reflect the properties of individual layers, h is the thickness of the entire stack, and the second equality in both equations uses the definition of Young's modulus $\sigma = E \cdot \varepsilon$. ε_0 and κ can be both derived simultaneously by solving the system of Equations 2.3 and 2.4. The configuration that is most relevant throughout this thesis comprises a stack of three layers, where only one outside facing layer has a non-zero volumetric strain α. As discussed by Du et al.[118], the curvature then is

$$\kappa = c_\kappa \cdot \alpha \qquad \text{Eq. 2.5}$$

with the strain to curvature constant c_κ defined as

$$c_\kappa = \frac{-6m_3 n_3[1 + 2m_2 + m_3 + m_2 n_2(m_2 + m_3)]}{h_1(1 + Y_2 + Y_3 + Y_{23})} \qquad \text{Eq. 2.6}$$

with $m_i = h_j/h_1$ and $n_j = E_j/E_1$ where $j \in (1,2,3)$, assuming that layer 3 is the swelling or shrinking compound and layers 1 and 2 are mechanically passive, and

$$Y_2 = 4m_2 n_2 + 6m_2^2 n_2 + 4m_2^3 n_2 + m_2^4 n_2^2 \qquad \text{Eq. 2.7a}$$

$$Y_3 = 4m_3n_3 + 6m_3^2n_3 + 4m_3^3n_3 + m_3^4n_3^2 \qquad \text{Eq. 2.7b}$$

$$Y_{23} = m_2m_3n_3[(4m_2^2 + 6m_2m_3 + 4m_3^2)n_2 + 12(1 + m_2 + m_3)] \qquad \text{Eq. 2.7c}$$

Predictions about the mechanical behavior of a shapeable material system based on this model can provide valuable insights even prior to sample fabrication and can help to estimate optimal layer thicknesses and device geometries, for instance to achieve maximum curvature, or minimal strain on certain components by placing them close to the neutral plane.

Another key aspect of shapeable material systems are the involved release technologies. Shape-transforming compounds are often fabricated as planar layer stacks on handling substrates and require partial or full delamination prior to any geometry change. The release can be achieved either through low-adhesion interfaces between the substrate surface and the bottom-most compound[108], or the selective removal of a sacrificial layer. A sacrificial layer is applied prior to the active and passive components of the shapeable material system onto the substrate and should therefore be sufficiently stable under the harsh fabrication conditions, including relevant temperatures, corrosive solutions, organic solvents, process gases, vacuum, and plasma. The removal of the sacrificial layer should be sufficiently selective, i.e., not damage the overlaying structures, not take extensive amounts of time, and be reliable to facilitate high-yield manufacturing. Previously investigated sacrificial layer technologies include inorganic[100,119,120], organic[99,114], and organo-metallic composites[28,86] as will be discussed in Section 3.1.

2.2.2 SHAPEABLE ELECTRONICS

Shapeable electronics[103] has emerged recently as a new field, rooted in the combination of shape-transforming material systems and micro-patterned electronic devices. After initial studies of strained membranes and their self-assembly into rolled-up tubes[98,121], self-rolling composites were used to demonstrate 3D micro-scale electronic devices[119,122]. Taking advantage of organic[102] and inorganic[100,123] material systems, micro-structures were batch-fabricated on Si or glass wafers and equipped with electronic components, before they self-assemble into various shapes.

One particularly versatile technology was pioneered by D. Karnaushenko and D. D. Karnaushenko at the Institute for Integrative Nanosciences (Leibniz IFW Dresden). Here, a three-layer thin-film stack comprises a metal-organic sacrificial layer (SL), a swelling hydrogel (HG) layer, and a reinforcing polyimide (PI) layer. The topmost PI layer

can carry further layers, such as metal structures[27,28,86]. After selective removal of the SL, the HG/PI compound rolls up to form a tubular structure in the so-called 'Swiss-roll' architecture (Figure **2.7**a). Key achievements of this material system are the robustness of the SL, the excellent adhesion between the HG and PI, its bio-compatibility that was demonstrated with cell toxicity investigations[86,124], a high yield during patterning and self-assembly[125], and the compatibility with standard, high-throughput and high-resolution manufacturing techniques, including photopatterning of the polymer layers. The deterministic roll-up process results in tubes with diameters ranging from 50 μm to 1 mm (Figure **2.7**b). The final tube diameter is determined by the layer thicknesses and the pH of the rolling solution[86,116]. This platform enables parallel fabrication on a wafer-scale (Figure **2.7**c) and has led to the developments of a diverse array of electronic devices (Figure **2.7**d-h), which profit from the geometry transformation in different ways. Rolled-up structures with many windings have a drastically reduced footprint compared to their planar equivalents, which improves the energy storage density of batteries and capacitors[124,126]. Magnetic encoders[125] (Figure **2.7**d), helical micro-antennas[28] (Figure **2.7**e), and transformers[127] were realized through the reshaping and re-orienting capability of the shapeable polymer stack. Electronically functional fluidic channels have been developed based on self-rolling tubes, and were integrated into micro-fluidic systems, e.g. impedimetric sensors for high-throughput immune cell analysis[116] (Figure **2.7**f) and nuclear magnetic resonance chips[128]. In addition to permanent shape-transformations, the platform allows *in situ* geometry adaptations to a limited extent. This was demonstrated with cuff implants (Figure **2.7**g) that were equipped with active electronic circuits based on thin film transistors (TFTs) and could wrap around fibers when exposed to moisture[86]. Moreover, micro-electronic swimming robots (Figure **2.7**h) were developed to comprise two rolled-up reaction vessels for bubble production, enabling propulsion[129]. An integrated antenna allowed to harvest energy from an external electro-magnetic field to control the rate of bubble formation, allowing the steer the motile robot.

In this thesis, a novel type of micro-catheter is developed based on the self-rolling polymer stack. These electronically integrated self-assembled micro-catheters are presented in Chapter 4.
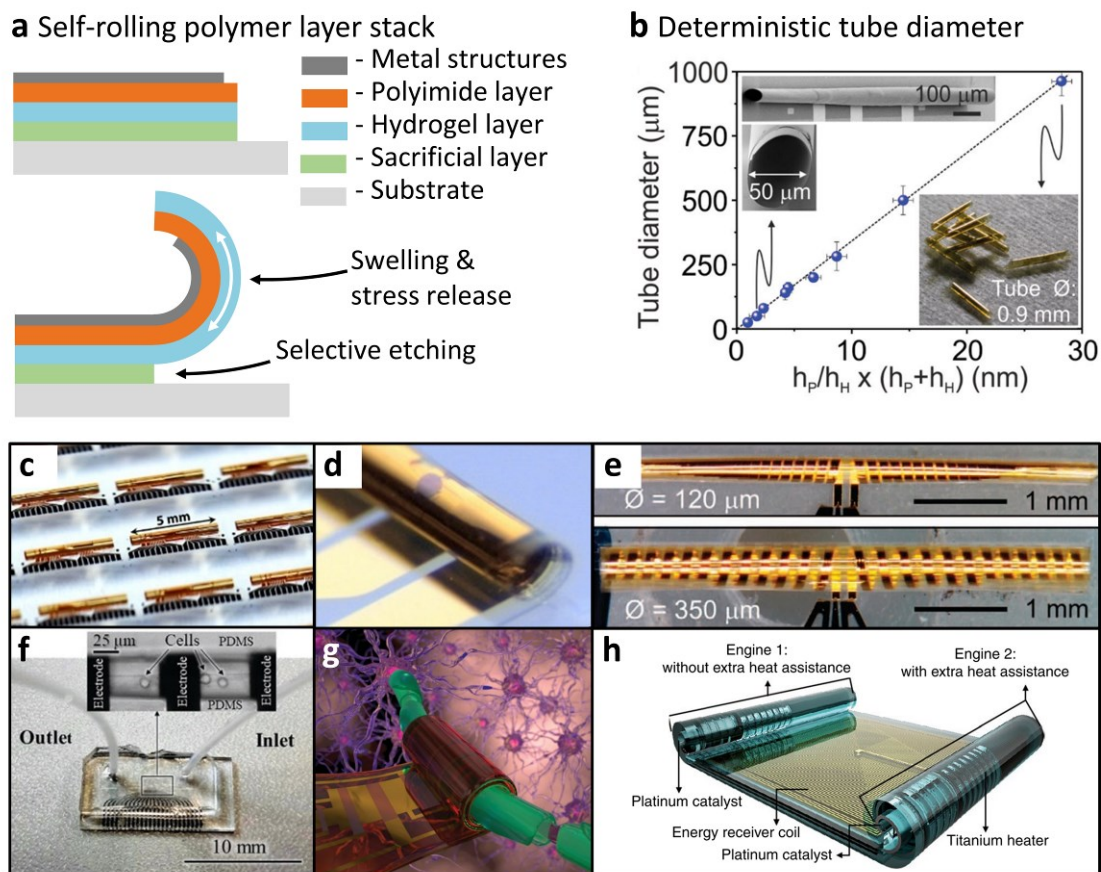
Figure 2.7: Self-rolled electronics based on the shapeable polymer stack: (a) The PI/HG bi-layer self-rolls when the SL is removed. **(b)** Rolled-up polymer tubes have a deterministic diameter defined by the layer thicknesses[86]. **(c)** An array of giant magnetoresistance angular encoders[125]. **(d)** A rolled-up polymer tube with electrodes and a spin valve magnetic sensor[125]. **(e)** Helical antennas with different diameters[28]. **(f)** Impedimetric micro-fluidic sensor[116]. **(g)** Concept image of nerve cuff with integrated active electronics[86]. **(h)** Artistic sketch of a micro-swimmer with tubular reaction vessels for bubble propulsion and an energy receiver coil[129]. Reproduced with permission from Springer Nature.

2.2.3 SOFT ACTUATORS AND MANIPULATORS

Established robot-assisted surgical systems rely on grippers (forceps) that are actuated using wires and external motors[130]. As discussed in Section 2.1.2, surgical micro-tools based on FE could be a valuable addition to the toolset of MIS due to their lower stiffness and embedded functionalities. Small scale thin-film devices, however, are not compatible with conventional means of actuation, such as motors and wired force transmission, and thus require alternative approaches towards shape control. Several lines of research investigate mechanisms that would enable soft and small-scale actuators, including those actuated by electric[131] (Figure **2.8**a) and magnetic[132,133] fields, pneumatic[134–136] (Figure **2.8**b) or hydraulic pressure[137], and polymers that respond to various stimuli, such as light[66,138] (Figure **2.8**c), temperature[106], moisture[110], or pH[124]. Among these, stimuli responsive polymers are appealing for the development of micro-scale

actuators[139]. Regarding upcoming applications in MIS, prospective actuators should offer short reaction times within seconds, a general bio-compatibility of the working conditions (temperature, pH, applied voltages), and the reliance on exclusively physiologically plausible triggers. The latter implies that stimuli responsive polymers that react to light, heat, pH, or moisture are not ideal candidates for operations inside a patient's body. In addition, the actuation should be gradual, i.e. not just between two extreme positions, and reversable, at least for some hundreds of times.

Regarding these requirements, electrical signals are a favorable trigger mechanism for shape transformations as they can be applied in a site-selective and rapid fashion. Among electro-sensitive materials and composites, electro-active polymers (EAPs) offer themselves as promising candidates. EAPs include a diverse collection of compounds that change their shape, e.g. through volumetric expansion or bending, according to an electrical bias. A prominent actuator technology among EAPs are ionic polymer-metal composites (IPMCs)[107,140–142], which has been considered for bio-medical applications. IPMCs are ion conducting membranes that are sandwiched between inert electrodes such as platinum. The membrane contains ions and water that are displaced when an external bias voltage is applied, leading to a pressure gradient and subsequent curving of the IPMC. These actuators can be fabricated as relatively thin layers with thicknesses of tens of micrometers, or as multi-layers to excerpt stronger forces (Figure **2.8**d). Despite such favorable properties, these compounds have a number of drawbacks. First, the required bias of 3-5 V might be hazardous in physiological environments since these voltages are outside the electrochemical window of water and could lead to gas bubble formation due to water splitting. Moreover, IPMCs are notoriously difficult to process in monolithic micro-patterning schemes.

In contrast, actuator composites based on conductive polymers (CPs) such as polypyrrole (PPy) require only small bias voltages (< 1 V) to induce bending actuation and are regarded as suitable and safe for biomedical and *in vivo* applications[108,115,143,144]. The material properties and actuation mechanism of PPy are detailed in Section 3.1.4. The fabrication of these actuators is compatible with standard micro-fabrication workflows (Section 3.2.5) and they operate naturally in electrolyte solutions[144,145]. The development of PPy actuator-based micro-scale devices was pioneered during the 1990s after the controlled volume change of CP compounds has been reported previously[146]. PPy compounds, also sometimes referred to as 'artificial muscles', have been widely

explored as actuation technology for devices on the centimeter down to the micro-scale, leading to the development of micro-vials[147] (Figure **2.8**e), actuator arrays capable to grasp fibers[148], steerable catheter guidewires[149] (Figure **2.8**f), and micro-manipulators[115] which comprised multiple independent digits and were able to lift and move glass spheres (Figure **2.8**g), just to name a few.

All these demonstrations depended on a direct line of sight between the operator and the devices to reliably control the operation. Furthermore, the actuation performance of PPy and other EAP actuators depends drastically on numerous factors, including operational and fabrication conditions, and degradation[150–153]. To ensure reliable and reproducible shape changes, EAP actuators, just as other actuation technologies in robotics, require feedback control. Feedback control requires an assessment of the momentary shape of the actuator, which is then used in an algorithmic procedure to adjust the physical parameter that regulates actuation, i.e. the bias voltage in the case of PPy actuators. Feedback control of EAP actuators was first explored using optical sensors to monitor the actuation amplitude[154]. Although it was possible to improve the positioning accuracy and reliability in a laboratory environment, feedback strategies that rely on an optical line of sight are not feasible for real-life applications[155], for instance in MIS. The approach to measure electrical properties (impedance, charge) of EAP actuators to determine their shape was proposed as part of the concept of *self-sensing actuators*[156], which to date massively struggles with noise and the decoupling of driving and sensing signals. Model-based strategies such as feed-forward control were shown to predict the shape of freely moving actuators accurately[155], but cannot account for interactions with an unpredictable environment, for instance when actuation is impeded by an obstacle. A superior strategy relies on the mechanical coupling of different components for actuation and sensing. There, either a part of the actuating material was electrically separated and used for strain sensing, or a strain sensor was attached to the device[157–160]. These actuator-sensor systems had sizes on the centimeter scale and enabled feedback control. Although being conceptually favorable to optical and model-driven approaches, these sensor-integrated devices are not easily miniaturized due to the involved fabrication schemes, since previously reported systems rely on the manual assembly of separate components or use ineffective materials for curvature sensing.

The next generation of bio-medical instruments requires a technological approach to seamlessly integrate actuators into complex flexible micro-robotic systems. In this thesis,

PPy micro-actuators are integrated alongside curvature or magnetic sensors into re-shapeable micro-electronic devices as presented in Chapter 5. Sensor technologies that are useful for this and other purposes are introduced in the following section.
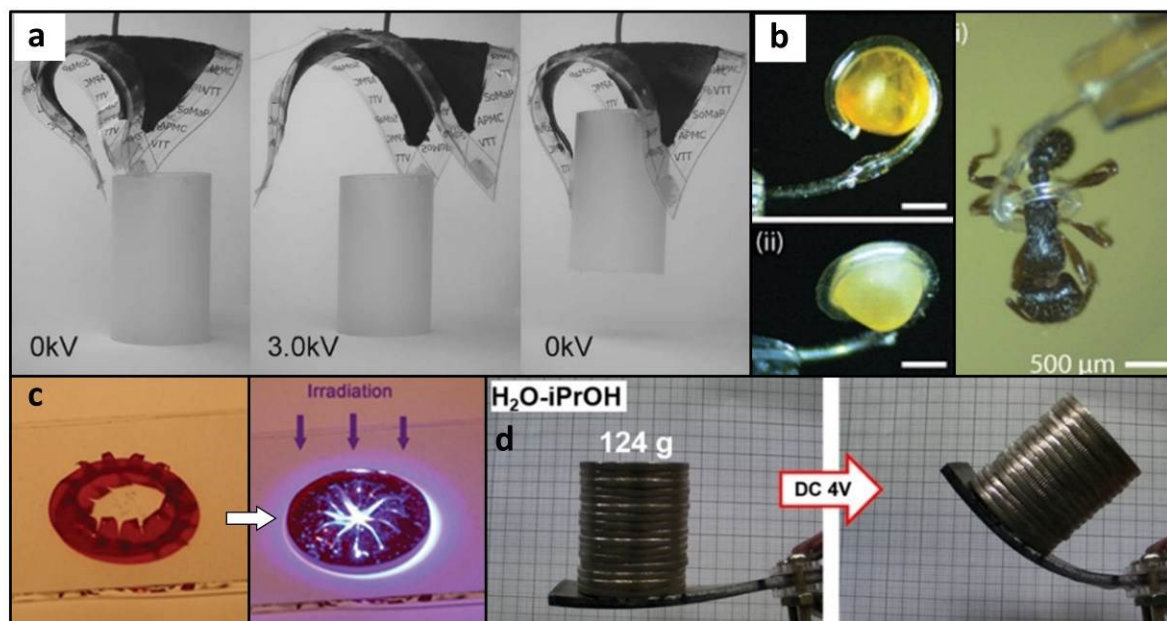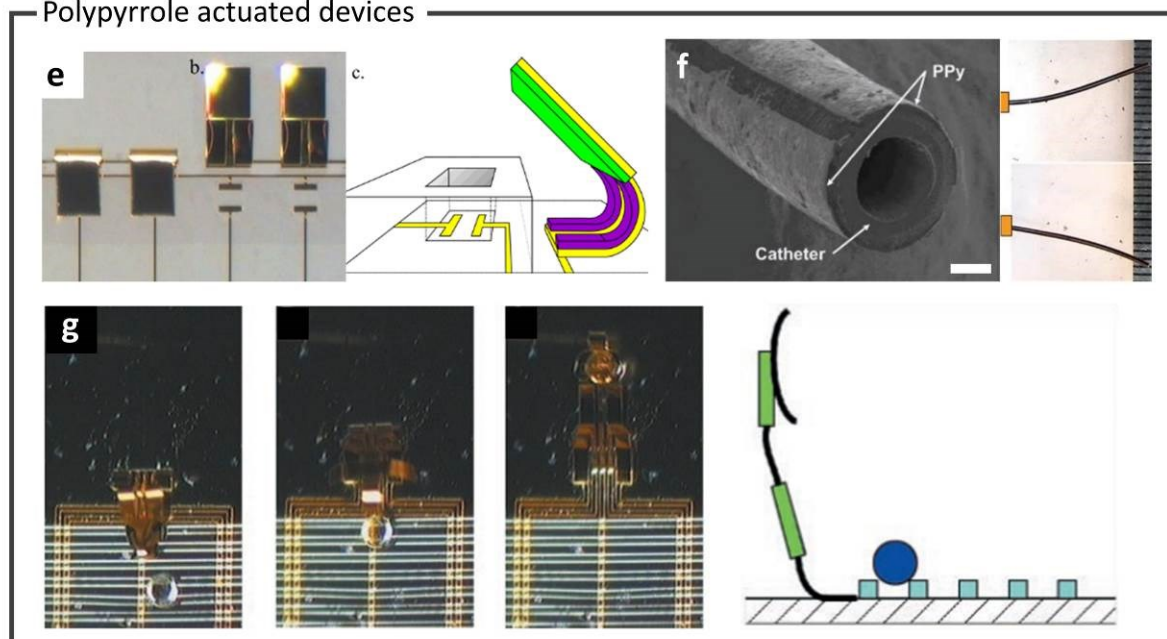
Figure 2.8: Soft actuators: (a) A dielectric actuator bends when high voltage is applied[131]. Reproduced with permission from AIP Publishing. **(b)** A pneumatic tube manipulates tiny and sensitive objects[135]. **(c)** An artificial iris closes upon exposure to light.[138]. Reproduced with permission from John Wiley and Sons. **(d)** Ionic polymer metal composites bend when an electrical bias voltage is applied[141]. Reproduced with permission from American Chemical Society. **(e)** A micro-vial with a PPy-actuated lid (150 µm width)[147]. Reproduced with permission from Springer Nature. **(f)** A bending catheter guide wire[161]. Scale bar indicates 150 µm. **(g)** A micro-hand with independent digits manipulating a 100 µm glass bead[115]. Reproduced with permission from ASSS.

2.3 SENSORS FOR POSITION AND SHAPE FEEDBACK

In classical open surgery, medical practitioners have direct access to the relevant tissues and organs, and obtain all require information through their senses of sight and haptics. In contrast, MIS is carried out using remote tools, such as robotic manipulators or catheters, which create a perceptional gap between the surgeon and the operation site in one or multiple ways, for instance by obstructing the line of sight or taking away haptic feedback[57]. Intelligent surgical tools should integrate electronic sensing capabilities that can provide the medical practitioner with the desired information. Relevant forms of feedback include, among others, the position and orientation of the surgical tools (replacing the sense of sight) and insights about mechanical interactions between the tools and surrounding tissues (replacing haptic perception).

This section provides an introduction into two types of sensor technologies, namely magnetic sensors that are suitable for position measurements in Section 2.3.1, and strain sensors that can monitor the curvature of flexible structures in Section 2.3.2.

2.3.1 MAGNETIC SENSORS FOR POSITION AND ORIENTATION MEASUREMENTS

Magnetic sensors are ideally suited for position measurements in physiological environments. In contrast to optical, acoustic, and electrostatic fields that suffer from absorption, reflection, and screening in biological tissues, static and low frequency magnetic fields generally do not interact with such matter. Hence, they offer themselves as bio-compatible and safe reference frames for navigation in deep-tissues. A variety of magnetic sensors has been developed and now constitute a key technology, contributing to applications such as automation and manufacturing, robotics[162,163], consumer electronics, and healthcare[164,165]. Magnetic sensors based on various physical effects offer different properties operational regarding field range, sensitivity or sensing directions.

The *anisotropic magnetoresistance* (AMR) effect describes the interaction between the resistance of ferromagnetic (FM) metals and an external magnetic field, which is commonly taken advantage of in magnetic field sensors[166,167]. AMR emerges already in very simple soft magnetic structures, such as thin layers of NiFe alloys (Permalloy), if a steady state magnetization is induced either through a shape anisotropy[168], an external magnetic field[169], or an additional pinning layer that provides an exchange bias[170]. It is

commonplace, although not imperative, to pattern AMR structures as stripes and magnetize them along their long axis as indicated in Figure **2.9**a-1. The AMR is well-studied and in-depth discussions can be found in available literature[171].
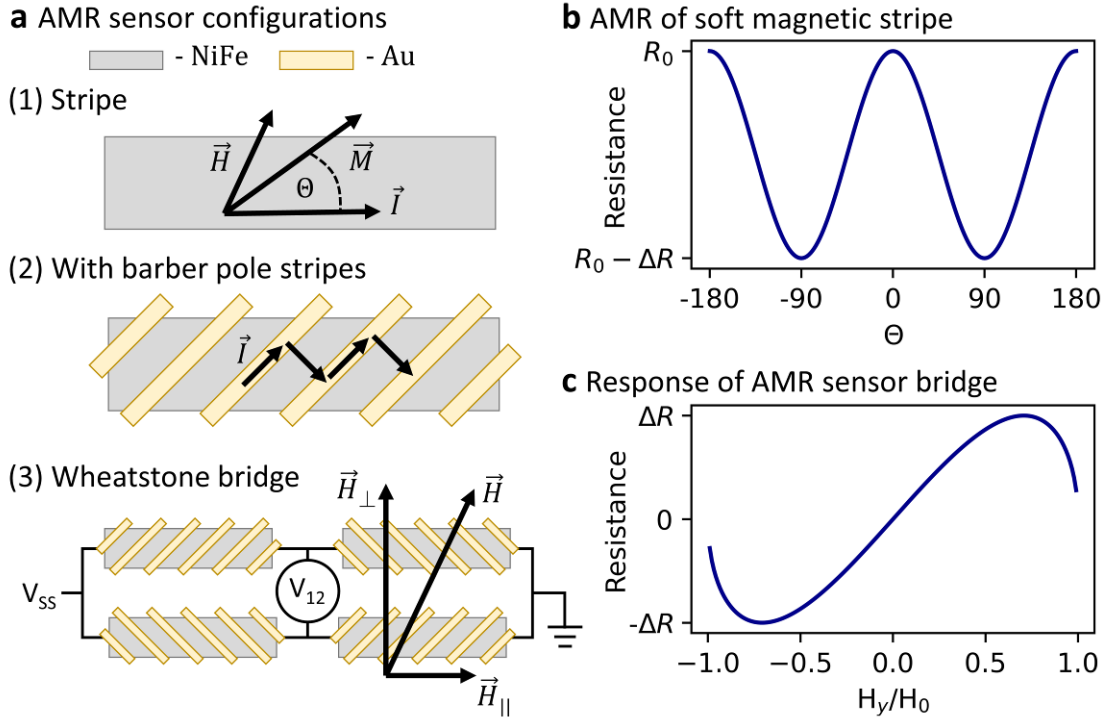

Figure 2.9: Anisotropic magnetoresistance sensors: (a) Illustration of (1) a simple AMR structure, (2) with barber pole stripes to redirect the current flow, and (3) in a Wheatstone bridge configuration **(b)** Angle dependent resistance of simple AMR structure. **(c)** Expected response of an AMR sensor in a Wheatstone bridge configuration during an orthogonal field sweep.

The resistance of such a structure can be described with the Voigt-Thomson law, which reads

$$R(\Theta) = R_0 - \Delta R \cdot \sin^2\Theta \qquad \text{Eq. 2.8}$$

where R_0 is the resistance in absence of a magnetic field, ΔR is the highest observed resistance change that is specific to the material, and Θ is the angle between the electric current $\vec{I}$ that is conducted through the AMR stripe, and the total magnetization $\vec{M}$, which is rotated by the external magnetic field as indicated in Figure **2.9**a-1. Evaluating Equation 2.8 (Figure **2.9**b) reveals that the AMR is highest when the magnetization and the current align (parallel or anti-parallel, 0° or 180°), and lowest when those vectors are perpendicular (± 90°). In an established and widely used method to compensate the small sensitivity and non-linearity for small fields, metal stripes ('barber pole' stripes, BPs) are patterned diagonally at 45° on top of the magnetic stripe[172,173], as shown in Figure **2.9**a-2. Using metals that are significantly more conductive than NiFe, e.g. Al or Au, the current bypasses the magnetic material through the BPs and traverses the NiFe

diagonally, choosing the path of least resistance. This redirects the current flow effectively by 45° relative to its original path. Regarding Equation 2.8, this offsets the angle between the current flow and effective magnetization, i.e. $\Theta_{BP} = \Theta - 45°$. This adjustment linearizes the sensor response for small magnetic fields and maximized its sensitivity. Using $\sin^2(\Theta + 45°) = 0.5 - \sin\Theta\cos\Theta$ derived from the trigonometric addition theorem, and $\cos\Theta = \sqrt{1 - \sin^2\Theta}$, Equation 2.8 transforms to

$$R(\Theta) = R_{0,1} + \Delta R \cdot \sin\Theta\cos\Theta = R_{0,1} + \Delta R \cdot \sin\Theta\sqrt{1 - \sin^2\Theta} \quad \text{Eq. 2.9}$$

where $R_{0,1}$ accounts for a constant offset. Finding the state of minimal magnetic energy and assuming small angles, one further finds the relationship

$$\sin(\Theta) \approx \frac{H_\perp}{H_0 + H_\parallel} \approx \frac{H_\perp}{H_0} \quad\quad \text{Eq. 2.10}$$

with the anisotropy field H_0 and the components of the magnetic field $H_\perp$ and $H_\parallel$ that are orthogonal and parallel to the steady state magnetization, respectively. The small angle approximation, and especially the omission of the parallel component $H_\parallel$ leading to the second approximation in Equation 2.10, is appropriate for weak external fields $|\vec{H}| < H_0$. Combining Equation 2.9 and Equation 2.10 yields

$$R(\vec{H}) = R_{0,1} + \Delta R \cdot \frac{H_\perp}{H_0 + H_\parallel} \sqrt{1 - \left(\frac{H_\perp}{H_0 + H_\parallel}\right)^2} \quad\quad \text{Eq. 2.11}$$

AMR sensors are commonly operated in a Wheatstone bridge configuration as depicted in Figure **2.9**a-3. This increases the sensor sensitivity by a factor of two and renders the total bridge resistance independent of the external magnetic field, further improving the sensor linearity. There are two alternative ways to achieve this configuration. Either AMR structures are positioned in parallel and adjusted with BPs in such a way that adjacent stripes have orthogonal current directions. Alternatively, AMR structures can be positioned in a rectangular pattern. In this case, BPs are omitted and linearization is instead achieved with a steady state magnetization (pinning) at a 45° angle to the stripes. Figure **2.9**c displays the response of an AMR sensor bridge when an orthogonal field is applied. It is linear for small fields, then peaks and reverses when the magnetic field strength approaches the anisotropy field H_0. The high sensitivity of AMR sensors makes them extremely useful for the measurement of small magnetic fields, e.g. the earth magnetic field (tens of µT) as electronic compass[167,168].

While AMR sensors are attractive to detect and measure extremely small magnetic fields, other sensor technologies can satisfy different needs. *Spin valve magnetic sensors* (SVMS) exploit the *giant magnetoresistance* (GMR) effect to offer themselves as precise angular encoders[125]. Among different possible configurations, top-pinned in-plane spin valves are realized with a multi-layer stack comprising FM and antiferromagnetic (aFM) layers. As depicted in Figure **2.10**a, an aFM layer fixates the magnetization of a FM 'pinned layer' stack from above. The magnetization of these layers is permanently defined during the fabrication process.
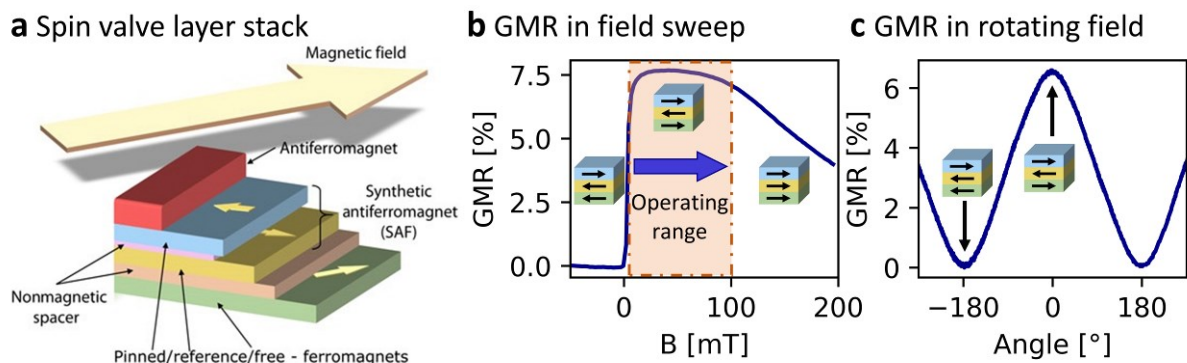

Figure 2.10: Spin valve magnetic sensors: (a) Schematic view on the layer stack forming a top-pinned in-plane spin valve magnetic sensor[125]. **(b)** GMR during a field sweep along the pinning direction. **(c)** Angular dependence of GMR in a rotating magnetic field in the saturation regime. (b) and (c) adapted with permission from AAAS[125].

Separated by a non-magnetic spacer, the FM 'free layer' is positioned at the bottom of the multi-layer stack. Ideally, the free layer is always aligned with the external magnetic field. This can be facilitated with the introduction of an additional FM layer, the 'reference layer', in a synthetic aFM configuration with the pinned layer, which effectively cancels the stray fields of the pinned and reference layers. Figure **2.10**b shows the typical resistance characteristic when an external field is applied along the reference direction, featuring a flat region for negative bias fields when the free layer is anti-parallel to the reference layer, a steep increase and plateau for positive fields that align the reference and free layers, and finally a decrease for fields that are high enough to flip the magnetization of the reference layer. The sensor stack is considered 'saturated' when exposed to field strengths within the plateau region (between 5 mT to 60 mT Figure **2.10**b) and can be used for angular encoding there. If such a sufficiently strong field is rotated in the sensor plane, the free layer magnetization aligns accordingly. The layer stack resistance then depends on the angle Θ between the reference and free layer magnetizations. The relationship is accurately described by

$$R(\Theta) = R_0 - \Delta R \cdot \cos \Theta \qquad \qquad \text{Eq. 2.12}$$

where R_0 is the highest observed resistance and ΔR its greatest reduction. The relationship described with Equation 2.12 is shown in Figure **2.10**d, where the resistance of a SVMS is measured inside a rotating magnetic field of about 10 mT. The resistance is lowest when the free and reference layers are aligned, and highest when they are anti-parallel.

2.3.2 STRAIN GAUGE SENSORS

Strain gauge (SG) sensors are used to measure the surface strain of objects that are bent or stretched[174]. These devices consist of traces of conductive material that undergo a resistance variation when experiencing mechanical strain. The ratio between mechanical strain and resistance variation, the gauge factor (GF), has two main contributions: geometric effects due to the stretching and thinning (or compression and thickening) of the conductive traces, and the piezoresistive effect. The GF of thin-film metals is relatively low (2-5), but can be considerably higher (up to 200) in materials which exhibit a strong piezoresistive effect[175], e.g. Si. Since the resistance change is proportional to the total resistance of the SG, the absolute measurable signal can be improved if the length of the strained conductive traces is increased, and their width is decreased, e.g. in a meander pattern as shown in Figure **2.11**a. The resistance of such a meander increases when the underlying object stretches or bends downwards (Figure **2.11**b) and decreases when compressed or bent upwards (Figure **2.11**c).
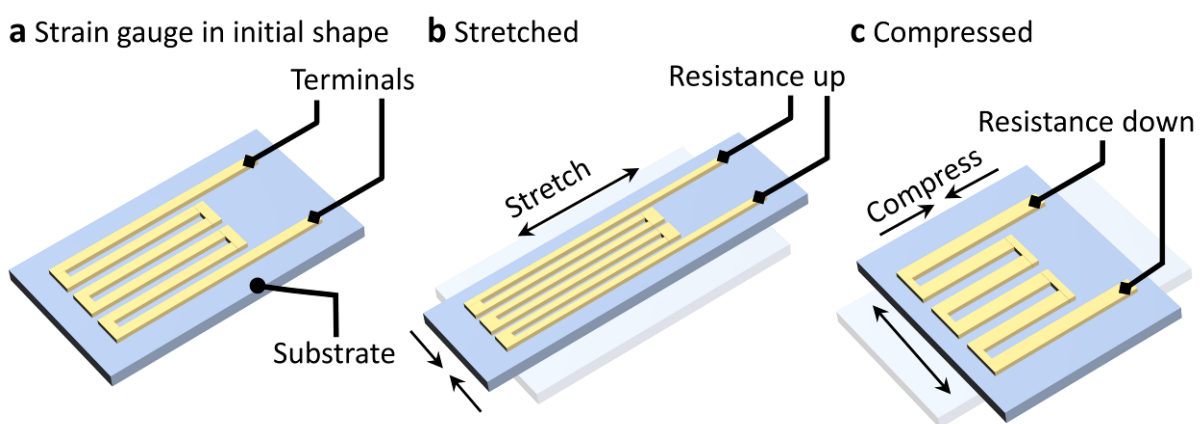

Figure 2.11: Strain gauge sensors: (a) A meander-shaped metal trace attached to a flexible substrate. **(b)** The resistance increases during stretching and downwards bending and **(c)** decreases when compressed or bent upwards.

To detect even subtle resistance changes, common setups include the Wheatstone bridge configuration and four-point resistance measurements. In the four-point configuration, a constant current is applied through the SG using two electric leads, and the voltage drop

across the SG is measured using two separate leads, thereby avoiding a dilution of the signal by the resistance of not sensitive parts of the device. Temperature variations can strongly affect the resistance of a SG in multiple ways, including changes of ohmic resistance, and thermal expansion and contraction of the SG and underlying material. A reference SG, i.e. an identical SG that is attached onto an identical surface that does not experience strain, should be used to correct for these effects.

3 MATERIALS AND METHODS

This chapter introduces the technologies that are involved in the fabrication and operation of integrated micro-tools. Recently developed materials, specifically for shapeable and reshapeable polymer systems, are discussed in Section 3.1. Section 3.2 introduces the diverse set of subtractive and additive processing techniques that were applied throughout this thesis. Section 3.3 briefly introduces key techniques for the characterization and evaluation of developed devices. The operation of integrated electronic devices in this work, especially those using feedback control, relies on the interpretation of sensor signals. Section 3.4 introduces the mathematical tools used for signal processing and evaluation.

3.1 MATERIALS FOR SHAPEABLE ELECTRONICS

This thesis is focused on the integration of polymer thin-films and electronic components to develop novel functional systems and devices. This development heavily relies on several material systems that have been previously established within their respective niches. The following sections introduce two distinct polymer technologies. First, the *shapeable polymer stack*[28,86], comprising a metal-organic SL, a reinforcing PI layer, and a swelling HG layer, which was developed by D. Karnaushenko and D. D. Karnaushenko at the Institute for Integrative Nanosciences (Leibniz IFW Dresden), is introduced in the Sections 3.1.1 to 3.1.3. Secondly, the micro-actuator technology based on PPy that was developed by multiple groups, most prominently by E. Smela, E. H. Jager, and O. Inganäs[108,148], is introduced in Section 3.1.4.

3.1.1 METAL-ORGANIC SACRIFICIAL LAYER

The SL used throughout this thesis is a metal-organic complex based on a polyacrylic acid (PAA) network that is crosslinked by lanthanum ions La^{3+} as illustrated in Figure **3.1**a. During sample fabrication, the precursor solution containing complexes of La^{3+} and acrylic acid (AA) and a photoinitiator are dissolved in AA, deposited via spin coating and patterned using photolithography (Section 3.2.1). Irradiation with UV light initiates a radical polymer chain formation, thereby forming a matrix of PAA chains that are cross-linked by coordinated La^{3+}. While unexposed parts are easily removed with DI water during the development step, polymerized and cross-linked structures are stable in water and mild aqueous bases, many organic solvents (e.g. 2-propanol, acetone,

dimethyl acetamide, N-ethyl pyrrolidone), and can withstand brief treatments in oxygen plasma and high temperatures of up to 600 °C. Taking advantage of these properties, various materials including polymers and thin-film metals can be deposited and patterned on top of it. There are two approaches to selectively remove the SL, which both target the coordinating bonds between La^{3+} and the deprotonated acid groups of the PAA chains. The SL can be etched with an acidic solution that protonates the carbolic acid groups of PAA. This reaction weakens their bonds to La^{3+} and thus the cross-links between PAA chains, which then dissolve into the solution. Alternatively, a strong chelating agent (e.g. diethylene triamine pentaacetic acid), which coordinates around La^{3+} more strongly than PAA, can strip it out of the SL, thus removing the cross-links, and likewise lead to its dissolution. The latter process also takes place in basic solutions (e.g. pH 9), but is generally slower than the acid-based approach. The optimal etching solution needs to be selected to be compatible with overlaying materials.
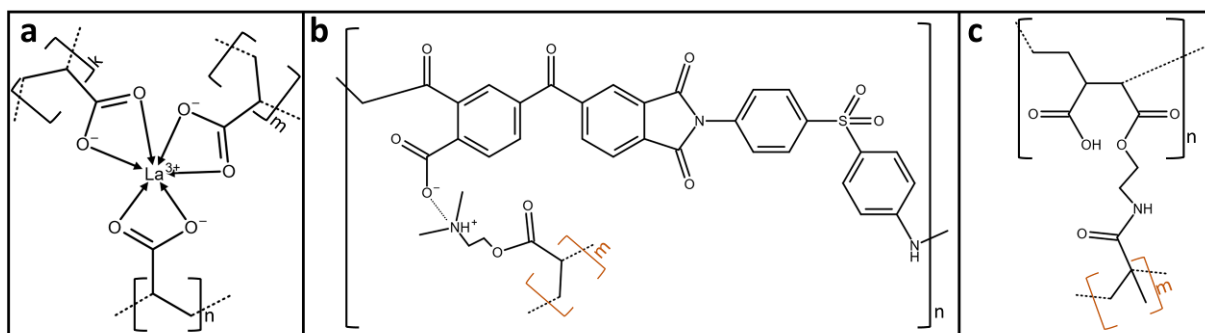

Figure 3.1: Materials for the shapeable polymer stack: (a) Metal-organic matrix for the SL **(b)** PI as reinforcing layer. **(c)** HG for the swelling layer.

3.1.2 POLYIMIDE AS REINFORCING MATERIAL

PI is a chemically and thermally resilient polymer that is widely used in the industry, e.g. for electronics. Following the procedure reported by Karnaushenko et al.[27], a polyamic acid pre-polymer mixture is synthesized, patterned via photolithography, and finalized with an imidization step during a hard bake to yield cross-linked PI layers (Figure **3.1**b). The mechanical properties of PI, e.g. its stiffness and tear resistance, depend on factors such as the length of polymer chains and the duration of the hard bake. Using thin-film fabrication schemes, layer thicknesses of hundreds of nanometers up to several micrometers can be achieved. This PI can be patterned to result in high resolution structures down to 10 μm and with positive slope side walls, which are important for the continuous support of thin metal films, e.g. deposited by evaporation (Section 3.2.2) or sputtering (Section 3.2.3). PI layers can withstand temperature of at least 300 °C, are

stable in organic solvents, acid solutions, but degrade slowly in basic environments via hydrolysis, and can be dry etched with oxygen plasma.

3.1.3 SWELLING HYDROGEL FOR SELF-ASSEMBLY

A HG graft polymer with a polyethylene-alt-maleic anhydride backbone was photosensitized (Figure **3.1**c) in a dimethyl acetamide solution and processed via spin coating and photolithography (Section 3.2.1). Thin HG layers of usually 100 nm to 1 μm were patterned on top of SLs before they were coated with PI. During and after the selective removal of the underlying SL, HG absorbs water that is attracted by its polar carbolic acid groups. HG swelling is pH sensitive, since its water uptake capacity increases in more basic solutions where its acid groups have higher polarity due to deprotonation. Consequently, the curvature of HG/PI bilayers can be controlled through pH variations, with higher pH leading to greater HG swelling, stronger curvature, and thinner tubes in Swiss-roll architecture devices.

3.1.4 POLYPYRROLE FOR FLEXIBLE MICRO-ACTUATORS

PPy belongs to the class of organic semi-conductors, specifically CPs. The defining feature of these materials is a chain of sp^2 hybridized carbon bonds, i.e. alternating single and double bonds, which allows the remaining p_z orbitals to form π-conjugated extended molecular orbitals with high electron mobility (Figure **3.2**a). It should be noted that extended molecular orbitals of pure PPy experience a periodic segregation due to its one-dimensionality, known as Peierls distortion[176]. For practical applications, PPy can be considered insulating in its neutral, and conductive in its oxidized state[177]. To achieve PPy that is permanently oxidized and thus conductive, immobile bulky ions, so-called dopants, are incorporated into the polymer network during electro-polymerization as will be discussed in Section 3.2.5. Doped CPs are useful surface coatings for sensors[178] and supercapacitors[124] since they drastically increase the specific surface area and charge capacitance of the underlying metal electrodes. When operated in an electrolyte solution, the electro-chemically driven exchange of solvated ions between PPy and the electrolyte leads to volumetric strain[179], i.e. swelling and shrinking (Figure **3.2**b). Bilayers comprising PPy and a flexible electrode, most commonly Au, Pt, or $InSnO_2$ and an optional supporting layer, thus can be used as bending actuators[108]. When a negative electrical bias below the reduction level of PPy is applied, it is charged due to the inflow of electrons from the underlying metal electrode. The influx of negative charges into the porous

material triggers the influx of hydrated positive counterions, such as Na$^+$, from the surrounding electrolyte and swells the polymer. When the negative bias voltage is removed and goes back above the oxidation potential, the polymer network discharges electronically, thereby expelling the counterions, and returns to its non-swollen state. The exact reduction and oxidation potentials depend on the various factors, including the polymerization conditions, dopants, solvents, counterions, and the counter electrode, but generally do not exceed -1 V (vs. Ag/AgCl). In the case of PPy doped with dodecylbenzene sulfonate (DBS$^-$) in a Na$^+$ rich aqueous electrolytes, a typical reduction potential of -0.8 V and oxidation potential of -0.5 V vs. Ag/AgCl can be observed (Section 3.3.3). This specific material system is especially interesting for bio-medical applications due to the natural abundance of Na$^+$ in physiological liquids and the small redox potentials below ± 1 V.

a Molecular structure of polypyrrole

Molecular orbital

b Mechanism of polypyrrole actuation

Flat   Expanded   Oxidation   Curved   Contracted
                            Reduction

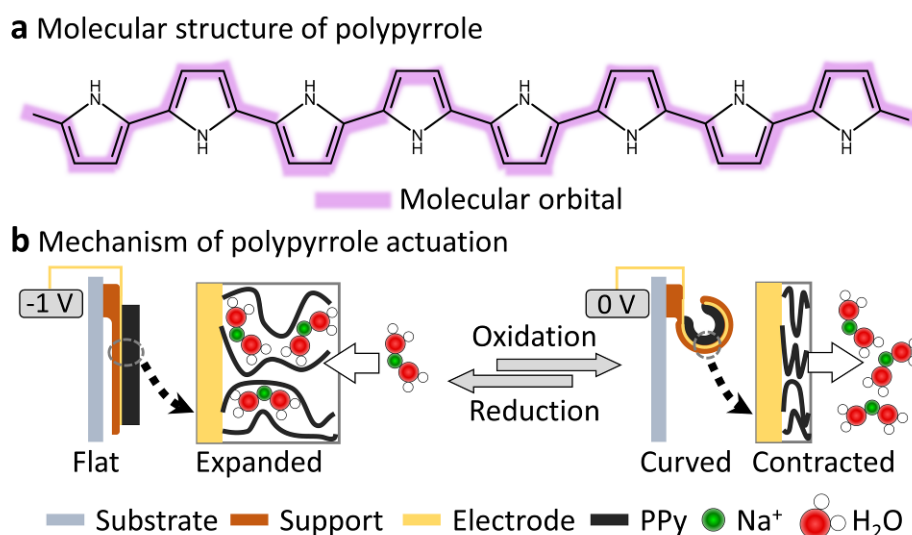Substrate   Support   Electrode   PPy   Na$^+$ H$_2$O

Figure 3.2: Polypyrrole for bending actuators: (a) Alternating single and double bonds lead to a distributed molecular orbital with high electron mobility. **(b)** A negative bias voltage reduces the CP and introduces negative charges. This attracts hydrated Na$^+$ counterions and swells the polymer matrix. Removing the bias has the opposite effect. Swelling and shrinking translates to flattening and curling in a bi-layer configuration. Biases voltages are applied against a counter electrode and denoted vs. Ag/AgCl.

A counterintuitive, yet important aspect of CP actuators is that an oversupply of electrical power beyond full reduction or oxidation does not translate into a higher output of force. Instead, high electrical potentials can lead to undesired chemical reactions, such as overoxidation of the PPy chains, which permanently degrades their charge transport capabilities[177]. Actuation performance as well as electro-chemical properties, however, do depend on the composition of different structural variants, which is initially defined during the electro-polymerization[180,181] (details in Section 3.3.3) and can change during operation and potential cycling[177]. To optimize the actuation performance, i.e., the capability of PPy to curve itself and its substrate, the deposition procedure and operation

conditions need to be carefully optimized. Moreover, the actuator geometry should be designed to achieve desired curvatures and the CP layer thickness needs to be optimized to ensure an efficient translation of strain into curvature as introduced in Section 2.2.1 and elaborated onto in Section 5.1.1.

3.2 Device fabrication techniques

Subtractive and additive manufacturing techniques were applied throughout this thesis to fabricate self-assembling and reshapeable micro-electronic systems. This section provides a brief introduction to these processes, including those to pattern thin polymer films via photolithography, deposit layers of metal and metal-oxides, and electro-chemically deposit CPs. The fabrication of devices was carried out in the facilities of the Institute for Integrative Nanosciences (Leibniz IFW Dresden).

3.2.1 Photolithography

Photolithography is a patterning process that takes advantage of photo-chemical interactions between light and specific photosensitive materials. Through the selective exposure to light with appropriate wavelengths and intensities, the solubility of a photosensitive polymer or photoresist (PR) is changed. This photochemical process allows to selectively dissolve the PR and results in functional structures or masking layers. Photolithography is widely used throughout the scientific and industrial fields for the manufacturing of micro-electronic circuits. A typical fabrication workflow comprises the following steps as illustrated in Figure **3.3**a:

First, the sample or substrate is cleaned. The cleaning procedure needs to be adjusted with regard to the substrate material, but typically includes a rinsing step with organic solvents and an oxygen plasma treatment. A thin layer (~ 1 μm) of PR is deposited with one of a variety of available solution-based techniques, including spray coating, dip coating, doctor blading, slot dye coating, or spin coating. Among these, spin coating offers excellent control over layer properties and reproducibility and is commonly chosen in industrial facilities (integrated circuit manufacturing) and laboratories. A thin organic or inorganic layer can be applied prior to the deposition of PR to improve the substrate wettability or promote adhesion. After PR coating, the newly formed film is dried or soft-baked using a contact hot plate or convection oven to remove excess solvent. This process can be promoted with a steady flow of dry air or an inert gas. Then, the desired pattern is projected onto the PR, typically with UV light. One common method to achieve the

projection is a mask aligner system. Here, a high-pressure mercury lamp generates the required UV light, which passes through a series of optical filters to select the portions of the light which are appropriate for the PR. The light is collimated into a parallel beam and passes a chromium mask with the desired image. Mask aligner systems such as the SÜSS MicroTec MA6 expose an entire sample at once and therefore allow rapid and high throughput manufacturing. Mask-less aligners, for instance the Heidelberg Instruments MLA 100, are alternative exposure systems that do not rely on physical masks to block out UV light. Instead, a micro-mirror matrix is used to project a digital image file piecewise and in series onto the sample.
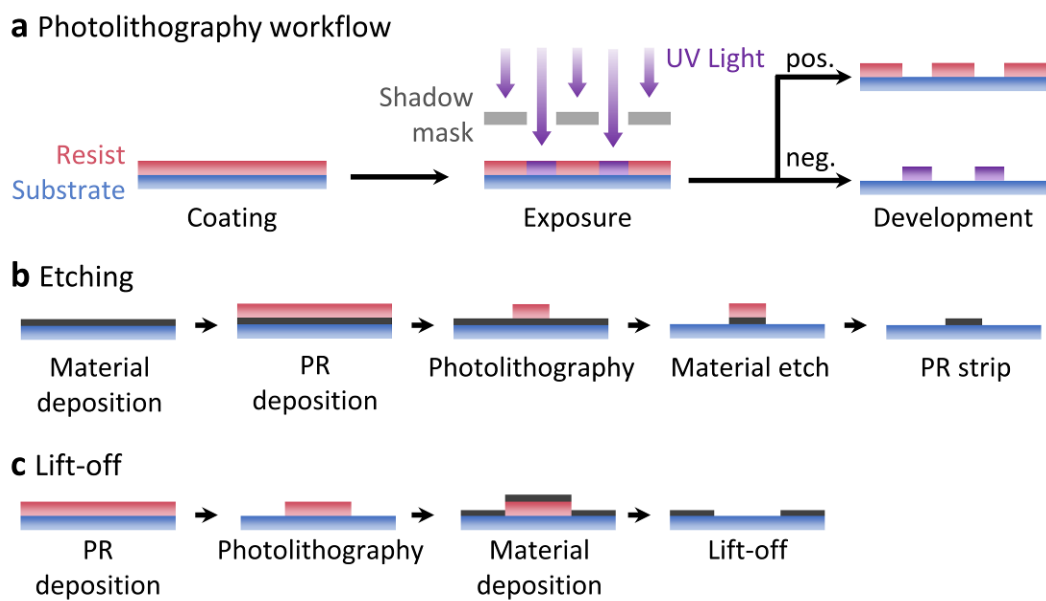

Figure 3.3: Photolithography processing of micro-structures: (a) A light sensitive polymer is selectively exposed to UV light, which increases (positive resist) or decreases (negative resists) its solubility in a developer. **(b)** To pattern a layer through etching, a masking layer is processed on top of the material and removed after the etching process. **(c)** To pattern thin films, an inverse PR pattern is processed on the substrate and the material is deposited on top. The desired pattern emerges after the excess material is removed together with the PR.

The pattern of exposed and shaded sample regions needs to be designed specifically for the applied PR. PRs are available in two tones, *positive* or *negative*. Positive PRs are not soluble in their respective developer when not exposed, and become soluble after exposure. This is achieved, for instance, with materials that generate strong acidic groups during exposure and then easily dissolve in aqueous alkaline solutions of organic (tetramethyl ammoniumhydroxide) or inorganic (NaOH, KOH) bases. In contrast, the solubility of negative PRs decreases upon exposure, for instance through polymerization of monomers or cross-linking of linear polymer chains. Non-exposed monomers are removed in a development step with organic solvents (e.g. propylene glycol monomethyl acetate, dimethyl sulfoxide). Developed PR is dried with a stream of pressured air or an

inert gas. These PR structures can be applied on top of to-be-patterned layers and used as masks for etching (Figure **3.3**b), or prior to the deposition of a thin film that is then patterned via lift-off (Figure **3.3**c). Functional polymer layers as introduced in Section 3.1 require an additional hard bake step (> 200 °C), e.g. to control the degree of polymerization and cross-linking and thereby tune the mechanical properties and remove volatile compounds to prevent degassing during consecutive fabrication steps.

In this work, photolithography was applied to pattern the SL, HG, and PI layers of the shapeable polymer platform, and to form PR masks for lift-off and wet and dry chemical etching using the high-resolution commercial PR AZ 5214e (MicroChemicals, Germany). Relevant processing parameters are provided in the Appendix A1.

3.2.2 ELECTRON BEAM DEPOSITION

Electron beam (e-beam) deposition[182] is a form a physical vapor deposition that is used to deposit thin layers of a variety of materials, including metals, metal oxides, and semi-conductors, with low to high melting point temperatures. To generate the required

vapor, the corresponding target material is bombarded with a beam of high-energy electrons as depicted in Figure **3.4**a. Upon impact, the kinetic energy of the electrons is converted into thermal energy, which increases the temperature of the target material and leads to its evaporation or sublimation. The resulting vapor thermally propagates upwards where it precipitates on the chamber walls and the sample, which is positioned heads-down above the ingot containing the evaporation material. E-beam evaporation results in high-purity films that are deposited with high rates of $0.1 \, \mathrm{nm \, s^{-1}}$ up to several $\mathrm{\mu m \, s^{-1}}$. Free electrons are generated thermally with a tungsten filament cathode, accelerated with a high electric field ($\sim 10 \, \mathrm{keV}$), and collimated into a beam. To avoid contamination of the e-beam source, it is place underneath the ingot containing the evaporation material and deflected in a magnetic field by 270°. The deposition is carried out in a vacuum chamber with pressures below $10^{-7} \, \mathrm{mBar}$. This setup aides to preserve film purity and minimize the number of collisions between evaporated material and residual gas to maintain a narrow deposition area. E-beam deposition setups commonly contain further components, such as a water-cooling system for the ingots, shutters, and a quartz micro-balance to monitor deposition rates *in situ*. E-beam evaporation is a comparably anisotropic process which results in a poor step coverage if no counteracting

measures, such as deposition under an angle, are taken. As such, it is well suitable for the processing of lift-off patterned structures.

In this thesis, e-beam evaporation was used to deposit thin Au layers, which were patterned to serve as parts of sensors, working electrodes for electro-polymerization of CPs, and electronic leads. To compensate for the poor adhesion of Au on Si and glass substrates, thin layers ($\sim$ 4 nm) of Ti or Cr were deposited underneath Au during the same vacuum process.
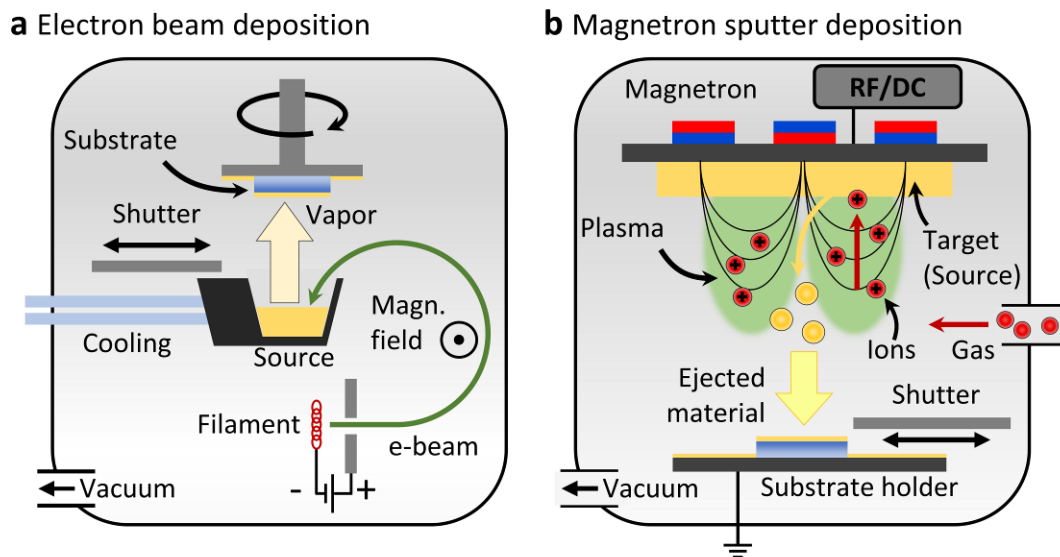

Figure 3.4: Physical vapor techniques for thin-film deposition: (a) Set-up for e-beam evaporation. **(b)** Setup for plasma sputtering.

3.2.3 SPUTTER DEPOSITION

Sputter deposition[182] is a versatile technique where atoms are released from target material through plasma bombardment and directed onto a sample, where they form thin layers. The process is carried out in a vacuum chamber (Figure **3.4**b) with base pressures of 10^{-6} mBar, which is then filled with an inert (e.g. Ar) or reactive process gas up to a pressure of about 10^{-3} mBar. Strong direct current (DC) or RF electric fields are applied between the target and the sample holder to ionize the process gas and form a plasma. DC fields can be favorable for conductive target materials, while RF fields are required for insulating ones. After plasma ignition, ionized process gas (e.g. Ar^+) is accelerated towards the target material where atoms are ejected upon impact. Sputtered atoms then propagate through the chamber towards the sample, where they form a thin layer at precisely controllable rates. This property of sputter deposition makes it particularly attractive for thin-film magnetic multi-layers. A shutter covering the sample is used to regulate deposition time and multiple targets can be installed within one sputter chamber to

deposit multi-layers in one continuous vacuum process. The plasma is confined to the surface region of the target material by magnetic fields using permanents magnets that are positioned behind the target holder. Sputter deposition is a relatively isotropic process and therefor well suited for step coverage. Although it is possible to pattern sputtered films via lift-off, care should be taken that the PR lift-off structures feature a pronounced undercut to avoid undesired step coverage.

In this work, sputter deposition was used to fabricate magnetic multi-layer stacks for AMR sensors (Section 4.3) and GMR sensors (Section 5.3).

3.2.4 ATOMIC LAYER DEPOSITION

Atomic layer deposition (ALD) is a chemical vapor deposition technique[182] that allows the repeatable isotropic formation of high-quality monolayers on samples using gaseous reactants. ALD is carried out in vacuum chambers where the sample is placed on a heated carrier. The deposition of metal-oxides, such as SiO_2, Al_2O_3, or HfO_2, for uses as insulating layers or dielectric gate oxides, commonly relies on the repetition of a two-step cycle. Figure **3.5** depicts exemplary the deposition steps required to form a Al_2O_3 layer.
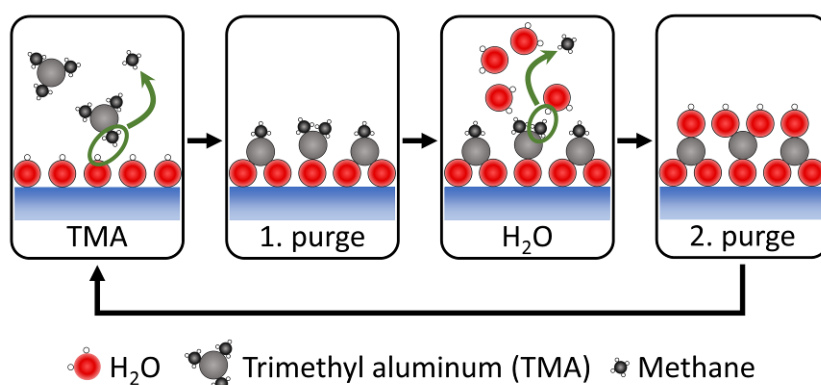

Figure 3.5: Atomic layer deposition of Al_2O_3: Schematic of single deposition cycle (1) First precursor reacts with surface groups (2) First purge (3) Second precursor reacts with first precursor, forming the desired compound (4) Second purge. Process resumes from (1) to deposit multiple layers.

The metal-organic precursor vapor (trimethyl aluminum) is injected into the reaction chamber where it reacts with available hydroxyl groups on the sample or from previous deposition steps. It was suggested that an initial layer can form on samples that do not contain the required chemical site, such as polymers that might lack hydroxyl groups, relying on precursor molecules that adsorb onto the sample surface. The precursor chemically bonds onto the entire surface of the reaction chamber and the sample in a self-limiting process, forming a continuous monolayer and under production of volatile

byproducts. Then, the chamber is purged with an inert gas, e.g. N_2, and the second reactant is introduced (H_2O or O_2 for Al_2O_3). During the second reaction step, the second precursor reacts with the monolayer that was formed during the previous half-step to form the desired compound, while undesired side-groups react to volatile species and are purged out of the chamber before the following cycle. The quality of the layer, i.e. the presence of uncovered patches or pin holes as well as its stoichiometry, needs to be finely controlled via the concentration of precursor gas and process temperatures.

In this thesis, ALD was applied to form dense and ultra-thin layers of Al_2O_3 that insulated magnetic sensors, strain sensors, and metal traces electrically and chemically from the environment. These protective layers proved useful in preventing undesired signal cross-talk between sensors and other electronic components in aqueous environments, and prevented the corrosion of sensitive metals when samples were treated with aggressive chemicals and during operation. In this sense, effective protective layers are of key importance for the herein presented system integration efforts.

3.2.5 ELECTRO-POLYMERIZATION OF POLYPYRROLE

Electro-polymerization is an electro-chemical deposition technique, similar to electro-plating, which is used to deposit films of CP onto conductive electrodes. The following discussion revolves around PPy[108,183,184], although it equally applies to similar compounds, including polythiophene or polyaniline.

To deposit PPy, a current is conducted between a counter electrode and a working electrode through a solution that contains pyrrole and a salt. In contrast to classical electro-plating of metals, the precursor monomer is not in an ionic state in its dissolved form, but a neutral molecule. Here, the working electrode is biased such that monomers are oxidized at its surface to form highly reactive, positively charged ionic radicals. Since the electron transfer happens on much shorter time scales than the diffusion of monomer radicals, the vicinity of the working electrode is enriched with this specimen. In this radical-rich region, these molecules can form an aromatic dimer through covalent bonding and the release of two protons (H^+ ions). The exact form of the monomer radical as well as the coupling reaction mechanisms are still subject to ongoing investigations. The key reaction steps are, as displayed in Figure **3.6**a: (i) Electro-oxidation of a monomer; (ii) formation of a dimer; and (iii) its relaxation into a neutral aromatic dimer. The latter then enters the cycle again in (i) to form a polymer chain of increasing length.

Since the oxidation potential of the dislocated electrons decrease with increasing chain length, longer chains are more likely to be oxidized and go through an additional growth cycle. Polymer chains of increasing length then precipitate and form a film on the working electrode. The growth process does not result in a perfectly neutral polymer, but about one in three to four units carries a positive charge. This is compensated by anions from the solution, which are incorporated during the deposition. These impurities play an important role as dopants, regulating the oxidation state and thus the electrical properties of the CP, and should be selected and administered with care. The salt that is selected for the precursor solution should offer a big anion that is not easily rinsed out of the polymer matrix. In this work, sodium dodecylbenzene sulfonate (NaDBS) was used due to its favorable size and low toxicity[185].
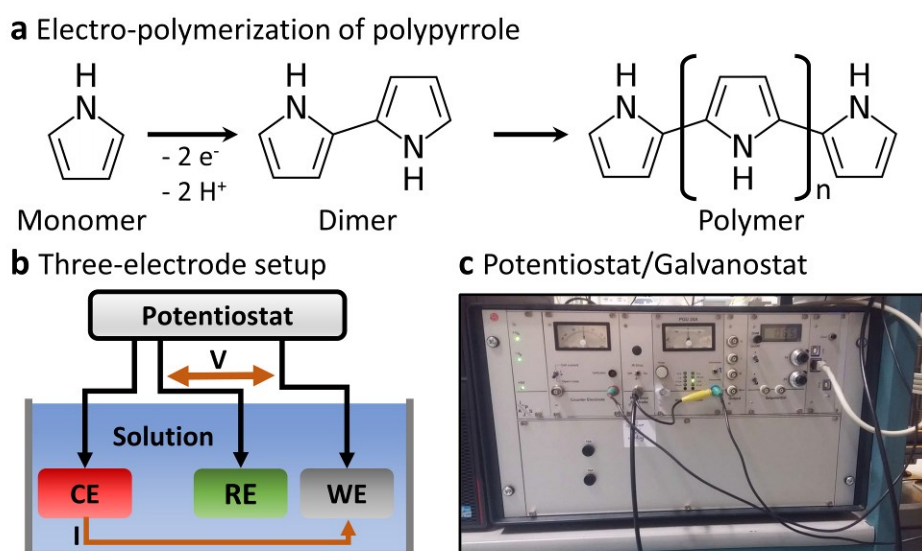

Figure 3.6: Electro-chemical deposition of PPy: (a) Steps of polymerization: Monomer radicalization, dimerization, progressive chain growth. **(b)** Schematic of three-electrode electro-chemical cell with a working (WE), reference (RE), and counter electrode (CE). **(c)** The potentiostat/galvanostat used in this thesis.

Although electro-polymerization can, and sometimes is, carried out in a two-electrode electro-chemical setup, it is advantageous to resort to a three-electrode system as depicted in Figure **3.6**b. In three-electrode systems[186], a reference electrode is included in addition to the working and counter electrodes. In this configuration, the bias voltage is applied (or measured) between the working and reference electrodes, while the current is measured (or applied) between working and counter electrode. The reference electrode conducts no current and the electrode material is selected to have a known and stable electro-chemical potential against the electrolyte. In this work, a Ag wire was plated with AgCl and used as a pseudo reference non-blocking electrode. A three-electrode electrochemical cell is connected to a potentiostat/galvanostat (Figure **3.6**c), which can

apply a desired potential between the working and reference electrodes by regulating the current (potentiostatic mode) or apply a desired current (galvanostatic mode).

In this thesis, electro-polymerization was applied to deposit PPy onto Au electrodes. The deposition protocol was adapted based on previously reported works[108]. First, the monomer solution was prepared by mixing 1.39 g of NaDBS into 40 mL of DI water (0.1 M), adding 0.278 mL of pyrrole monomer (0.1 M) and shaking for 20 min with a vortex mixer. Solution of NaDBS was usually prepared in bulk and stored for several weeks. Pyrrole monomer was distilled after delivery and stored at -20 ℃. The monomer solution could be used for several days. Directly before PPy deposition, samples with exposed Au electrodes were first rinsed with acetone and 2-propanole. A treatment with O_2 plasma (2 min, 100 W, 5 sccm O_2 flow, Diener Femto, Germany) was carried out in order to thoroughly remove organic contaminations and adsorbed solvent molecules. The plasma cleaning step proved critically important for the reproducible deposition of PPy actuator layers. After cleaning, samples were connected in a three-electrode setup as detailed above and immersed in the freshly prepared monomer solution.

Although pyrrole is polymerized onto the working electrodes at any bias voltage above 0.47 V, the rate of deposition has a strong effect on the actuation performance. Constant bias voltages of 0.50 to 0.53 V vs Ag/AgCl were applied to generate a deposition current density of around 10 mA cm^{-2} and the deposition time was adjusted to define the layer thicknesses. During deposition, the current was usually very low for the first 5-10 s (< 1 mA cm^{-1}), then rapidly increased and stabilized at a constant value that was determined by the bias voltage. The fine adjustment of the deposition bias voltage was required to compensate voltage drops of the device-specific embedded metal traces. Such electronic leads can introduce additional resistances of several kΩ and thereby lead to voltage drops of e.g. $\Delta U = R \cdot I = 2000\,\Omega \cdot 5\,\mu A = 10\,mV$. After deposition, PPy coated samples were rinsed with DI water and stored in NaDBS aqueous solution or phosphate buffered saline (PBS) solution until further use.

Electro-polymerization of PPy played a key role throughout this thesis. It was applied for the fabrication of micro-actuators in the micro-manipulators of integrated self-assembled micro-catheters (Chapter 4) and re-shapeable micro-electronic devices (Chapter 5).

3.3 DEVICE CHARACTERIZATION TECHNIQUES

This section introduces several techniques that were applied to characterize the magnetic, electrical, and electro-chemical properties material systems and devices. The evaluation of final devices was carried out in a variety of artificial and natural model environments, whose preparations are described in this section as well.

3.3.1 KERR MAGNETOMETRY

The magnetization and domain structure of reflective magnetic surfaces can be investigated with setups that use the magneto-optic Kerr effect (MOKE). MOKE describes the interaction of in-plane polarized light and magnetic materials as illustrated in Figure **3.7**. The polarization direction of in-plane polarized light rotates when it reflects from a magnetic surface. The rotation depends on the magnetization direction and can be observed with an analyzer (optical polarization filter) in the path of the reflected light. MOKE microscopy is routinely used to observe magnetic phenomena, e.g. domain structures. In combination with a magnetic field generated by electro-magnetic coils, MOKE magnetometry can be performed to investigate the interaction of magnetic domains and external magnetic fields[187,188].
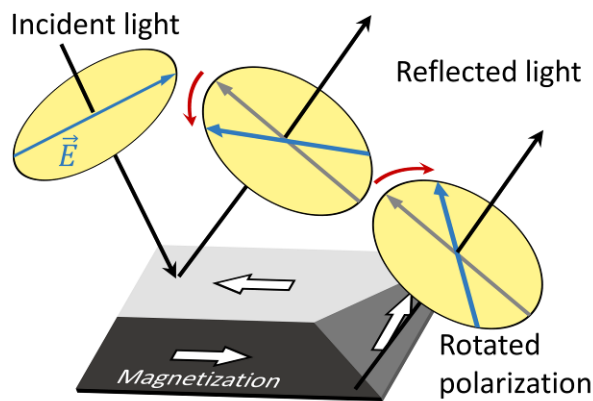

Figure 3.7: Magneto-optic Kerr effect: Schematic explanation of the Kerr effect. The polarization direction of linearly polarized light rotates upon reflection from a magnetic surface.

In this thesis, MOKE magnetometry was applied to measure the hysteresis loops of Py/IrMn/Py magnetic multi-layer stacks. The loops were recorded by applying an external magnetic field, and adjusting the magneto-optical sensitivity, along the pinning direction. Consequently, the brightness of the magnetic structures would shift when its magnetization was flipped by the external field. The brightness of the magnetic structures (image intensity) was recorded and averaged over several frames. Hysteresis loops were obtained by plotting image intensity as a function of applied magnetic field. An exchange

bias would lead to a corresponding shift of the hysteresis loop towards positive values of the applied field.

3.3.2 ELECTRO-MAGNETIC CHARACTERIZATION OF SENSORS

The performance of magnetic sensors was assessed using a Helmholtz coil setup, which generates a homogenous magnetic field. The setup comprises two parallel coils with a co-axial field orientation, a power supply, and a reference magnetic Hall sensor. The power supply is controlled with an external voltage bias that can be generated by a source-measure-unit (SMU), a signal generator, or an integrated source-measure PCB, as it was done in this work. The magnetic sensor is operated with an external SMU or SMU PCB as well, and the sensor data as well as the output of the reference magnetic sensor are recorded simultaneously. Sensor response curves are then commonly depicted as a function of externally applied field (bias field). The bias field is calculated using the reference sensor signal and a calibration curve, which ideally is a linear relationship, and needs to be established using a calibrated Gaussmeter.

3.3.3 ELECTRO-CHEMICAL ANALYSIS OF POLYPYRROLE

Cyclic voltammetry (CV) was carried out to investigate the electro-chemical properties of PPy layers using a three-electrode setup as described in Section 3.2.5 and depicted in Figure **3.6**b. CV is a useful technique in which a triangular bias voltage (Figure **3.8**a) with a defined slope, the so-called scan rate (voltage per unit time), is applied to the working electrode and the current is recorded (Figure **3.8**b). The voltage dependent current (Figure **3.8**c) can then be examined for material specific features. Regarding CPs such as PPy, CV reveals redox reactions as peaks of positive or negative current, implicitly indicating the exchange of hydrated ions with the electrolyte environment[108]. PPy chain networks can form in different variations, which are referred to PPy(I), PPy(II), and PPy(III), or blends of different variations[177,180]. These variations have different electro-chemical properties, resulting in different redox potentials. Among these, only the reduction and oxidation of PPy(I) and PPy(II) are desirable as these contribute the most to actuation, whereas PPy(III) has worse electrical and mechanical properties and stiffens the polymer network. The characterization of PPy actuators should therefor firstly confirm the presence of the desired redox reactions around -0.8 V and -0.5 V. The lack of these features strongly indicates non-optimal deposition parameters, such as the deposition voltage or current[181]. Plateau-shaped redox peaks are usually a superposition

of two redox peaks, corresponding to two distinct variants. A slight shift of redox peaks towards less negative biases indicates a transformation of PPy(II) into PPy(I), which however does not have a negative effect on actuation performance. Diminishing peak heights can indicate various processes, including the loss of a desired PPy variant due to transformation (PPy I → III), the loss of π-conjugated extended orbitals due to overoxidation, or a mechanical degradation of the interface between the CP and the electrode[152]. When electro-chemical analysis reveals undesired processes, measures such as protective electronic circuits or electrode surface treatments should be taken to preserve actuator performance.
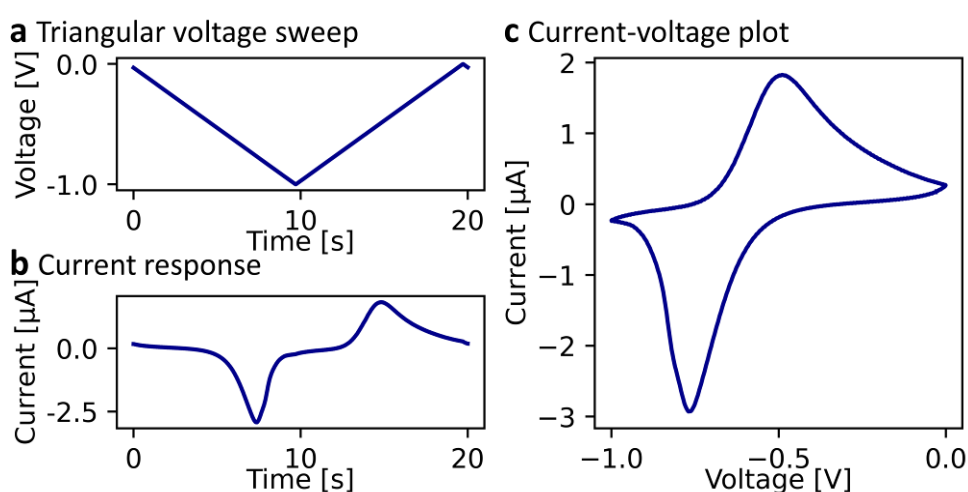
Figure 3.8: Cyclic voltammetry of PPy: (a) Triangular potential sweep that is applied to an electro-chemical cell. **(b)** The resulting current flow. **(c)** The combined current-voltage plot reveals potential-dependent redox reactions. In this case of PPy, they are indicated by a reduction (-0.8 V) and an oxidation (-0.5 V) peak.

3.3.4 PREPARATION OF MODEL ENVIRONMENTS AND MATERIALS

Model solutions with different viscosities[189] were used to investigate flow through rolled-up micro-catheters. To prepare a viscous solution, certain masses of methylcellulose (MC) were added to DI water. The mixture was stored at 8°C and mixed regularly by shaking until MC fully dissolved.

Agar phantoms[190] with hollow channels were prepared for insertion studies under US imaging. First, a mold was prepared from a plastic container and a thin tube that was spanned through its center. Using a hotplate and a beaker, DI water was brought to a mild boil before agar powder (1.5 %$_{mass}$) was added under constant stirring. The mixture was heated further until boiling and removed from the hotplate. After cooling to about 60 °C, the agar mixture was purred into the mold. An ultrasonic bath was used to remove air

bubbles. After complete cooling, the agar block easily slipped out of the mold and the tubing could be pulled out easily, leaving behind a smooth channel.

Various organs were retrieved from mouse models. The dissections were carried out by Franziska Hebenstreit and Dr. Mariana Medina Sánchez (both Leibniz IFW Dresden) at the Transgenic Core Facilities of the Max Planck Institute of Molecular Cell Biology and Genetics, Dresden. To retrieve the *esophagus* and the *stomach* used for targeted fluidic delivery studies, a cut was placed from the center bottom of the mouse to the top. To expose the digestive tract, an additional cut was placed at the bottom of the abdominal wall, at which point the organs can be retrieved carefully and stored in PBS solution. Directly before insertion experiments, the intestine was removed and the stomach with attached esophagus was flushed to remove residual contents. The cleaned organs were then placed on a rubber plate inside a PBS filled petri dish and fixed with thin copper wires.

Similarly, *sciatic nerves* were retrieved from already dead mice. A cut was placed at the dorsal thigh parallel to the femur. The skin tissue was placed away and the muscle was dissected into two to expose the sciatic nerve. The nerve was cut, taken out, and stored in PBS until usage.

3.4 SENSOR SIGNAL EVALUATION AND PROCESSING

Electronic systems can be equipped with sensors to monitor a multitude of aspects of their environment. Real world sensor signals, for instance in the form of voltage outputs, often do not directly reveal the required information and need to be processed before conclusions can be drawn. This section briefly introduces some useful signal processing techniques, including *kernel* and *band-pass filters* in Section 3.4.1 and *cross-correlation* in Section 3.4.2. Moreover, sensor-equipped systems that are designed to interact with their environment, e.g. through an actuator, require a formalism to convert incoming sensor signals into instructions for actions. This can be achieved through closed loop algorithms, such as *Proportional-Integral-Derivative* (PID) control, which is described in Section 3.4.3.

3.4.1 SIGNAL PROCESSING

Real world sensor signals are a superposition of the actual quantity that is to be measured, and both noise and systematic distortions. A variety of techniques have been developed to separate these components. One widely used and computationally simple operation to

reduce noise and flatten a signal is the moving average. A filtered signal is achieved by averaging all discrete measured values $S(t_i)$ within a defined time interval $[t_{i\text{-}n}, t_{i+n}]$

$$S_{\text{filtered}}(t_i) = \frac{1}{\sum_{j=-n}^{n} c_j} \sum_{j=-n}^{n} c_j \cdot S(t_{i+j}) \qquad \text{Eq. 3.1}$$

where c_j are weights that are assigned to each summand. All weights can be set to equal one or defined to follow e.g. a gaussian distribution, thereby reducing the significance of measurements that are more distant in time. In formal terms, Equation 3.1 is a *kernel filter.* Filters with box or gaussian kernels act as low-pass filters. In this sense, the kernel width, i.e., the length of the averaging time interval, should be chosen sufficiently long to effectively remove higher frequency distortions, but shorter than real features of the signal. Figure **3.9**a depicts a noisy signal before and after treatment with a low-pass filter.
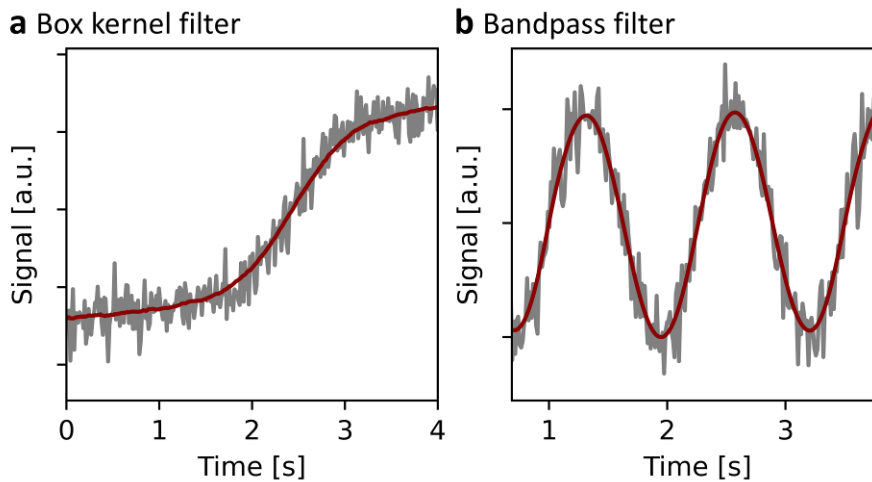
Figure 3.9: Signal processing: (a) High frequency distortions is removed with a running average. **(b)** A Butterworth bandpass filter isolates a frequency band from a distorted signal.

In more demanding procedures, however, the possibilities offered by simple kernel filters might be insufficient. *Bandpass filters* are useful if a signal with a constant and known frequency needs to be isolated from lower and higher frequency distortions. Figure **3.9**b displays a noisy sine signal that was passed through a second order Butterworth bandpass filter with critical frequencies of 50 Hz and 250 Hz. The pass band transmits frequencies around 100 Hz. Increasing the filter order improves the rejection of undesired frequencies but is computationally more expensive. A bandpass with suitable critical frequencies is useful to simultaneously remove probabilistic high-frequency distortions (noise), systematic distortions (parasitic fixed frequency signals), and low-frequency distortions (e.g. drift).

3.4.2 CROSS-CORRELATION FOR PHASE ANALYSIS

The *cross-correlation* is a mathematical operation to determine the time resolved 'similarity' of two signals. For two continuous functions f and g, it is defined as

$$(f \star g)(\tau) = \int_{-\infty}^{\infty} \overline{f(t)}\, g(t + \tau)\, \mathrm{d}t \qquad \text{Eq. 3.2}$$

where τ can be regarded as a shift of the function variables, e.g. time. When applied to two signals that are identical except for a time delay, the cross-correlate will display a maximum at the corresponding time lag τ as depicted in Figure **3.10**a.
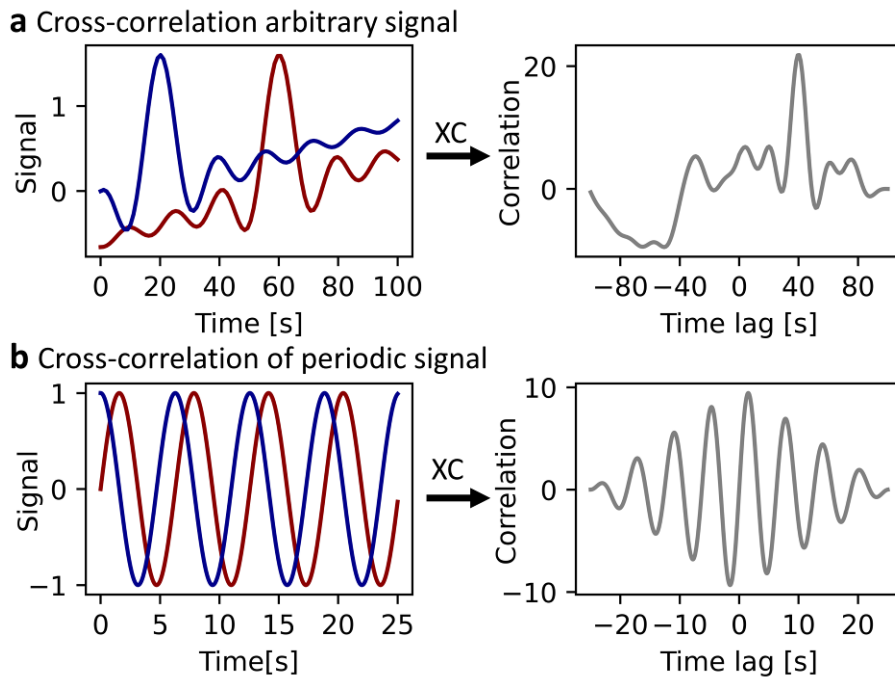
Figure 3.10: Phase analysis via cross correlation: (a) The cross-correlation of two signals with a time shift shows a peak at the corresponding time lag. **(b)** Two identical but phase-shifted signals yield an oscillating cross-correlate. Zero-pegging for times outside the measurement interval leads to the declining amplitude towards higher time lags.

The same operation applied to two periodic functions of equal frequency and a phase delay results in periodic maxima and minima as displayed in Figure **3.10**b. In this case, the phase shift ϕ of the signals can be computed from the smallest time delay τ_{min} that yields a maximum of the cross-correlation using

$$\phi = \tau_{min} \cdot 2\pi f \qquad \text{Eq. 3.3}$$

where f is the signal frequency. This operation to determine time delays is particularly useful for real world signals that are distorted by noise. Here, the inclusion of multiple periods effectively cancels out probabilistic distortions by summing up positive and

negative contributions. The accuracy of the time lag computation improves when more periods are considered.

3.4.3 PID FEEDBACK CONTROL

The regulation of a system in real time based on sensory measurements of its state can be achieved through *feedback control*. It is widely applied in industrial and consumer applications, for instance in kitchen ovens where the heat supply is regulated using a thermometer. In robotic systems, feedback control can be applied to adjust actuation depending on electrical signals from sensors, including those measuring force, strain, inertia, or magnetic fields. The conversion of measured sensor signals into instructions requires a mathematical formalism. Among a variety of control schemes that have been developed, PID control is useful to operate systems without detailed knowledge of their internal mechanisms[191]. PID control, as illustrated in Figure **3.11**, is a closed loop control scheme, that uses three variables: the setpoint (SP) that defines the desired state of the system, the feedback (FB) that is the current state of the system as measured using a sensor, and the output (OP) which is a correction to the driving parameter of the system. An update u to the OP is determined by computing the error e of the system, i.e. the mismatch between desired and real state,

$$e(t) = SP(t) - FB(t) \qquad\qquad \text{Eq.} \quad 3.4$$

and passing it to the control function

$$u(t) = K_P \cdot e(t) + K_I \int_0^t e(\tau)\,\mathrm{d}t + K_D \frac{\mathrm{d}e}{\mathrm{d}t}(t) \qquad\qquad \text{Eq.} \quad 3.5$$

where K_P, K_I, and K_D are the proportional, integral, and derivative gain constants, respectively. These are the parameters that define the dynamics of the system and can be determined heuristically, or through several tuning methods. PID control offers itself as easily implemented and universal control scheme that can yield acceptable results in many application scenarios. Some drawbacks are the inherent symmetry of the operation, which is disadvantageous for asymmetric systems, the permanently defined control parameters that cannot adapt to an evolving system, the inability to account for system non-linearities, and the sensitivity to noise[191].
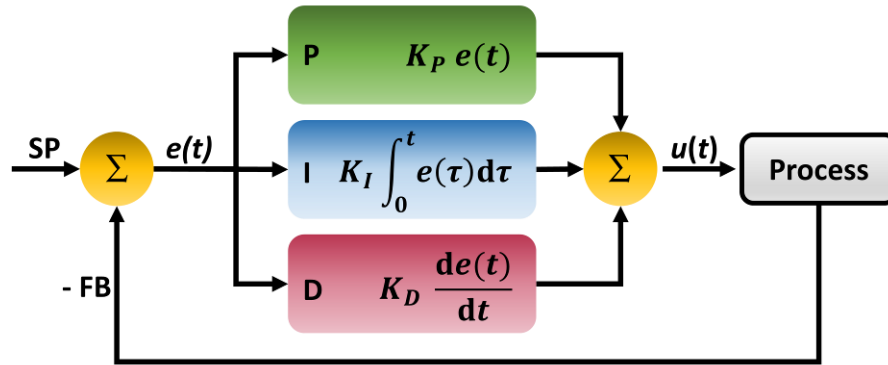
Figure 3.11: Proportional-Integral-Derivative closed-loop control: Schematic to illustrate the workflow for system regulation. The deviation of the system state from the desired set point (error) is assessed. The error is computationally processed with the three terms to determine an update. Finally, the update is applied to the system driver (output) and the control loop resumes from the beginning.

4 ELECTRONICALLY INTEGRATED SELF-ASSEMBLED MICRO-CATHETERS

MIS could massively benefit from catheters with built-in electronic functionalities, especially for navigation, manipulation, and sensing. This chapter is dedicated to the development and evaluation of electronically **i**ntegrated **s**elf-**a**ssembled micro-**c**atheters (ISACs) that are based on the self-rolling polymer stack introduced in Section 2.2.2. As depicted in the artistic illustration in Figure **4.1**a, this novel instrument features integrated micro-electronic devices that are embedded inside the catheter walls, while having a microscopic diameter of only about 0.1 mm (Figure **4.1**b), making it the thinnest integrated catheter that has been reported to date. The integrated electronics and fluidics, in conjunction with the tiny size, lead to a number of intriguing application scenarios as depicted in Figure **4.1**c: (1) ISACs are readily integrated into micro-fluidic systems to enable targeted drug delivery, e.g. to fill a small-scale aneurysm with a liquid embolic agent[34]. (2) The integrated micro-manipulator is envisioned to grasp and remove a clot out of a blood vessel. This gripping tool is located at the tip of ISACS and comprises four opposing digits that are actuated using the CP PPy. (3) ISACs are equipped with magnetic sensors, namely sensitivity-optimized AMR sensors, for position feedback and navigation. These sensors act as electronic compasses, allowing to track the location of the catheter in a gentle, non-invasive manner. ISACs are envisioned to act as the final element in a modular catheter system as depicted in Figure **4.1**a (bottom), where it is deployed from a regular micro-catheter that accommodates the fluidic and electronic connections. While the conventional catheter is used to navigate close to the site of interest, the ISAC is inserted into the smallest vessels close to the destination, where its embedded functionalities and small size enable the procedure. The small size of ISACs might not only enhance existing interventions, such as the treatment of increasingly smaller anatomies, but potentially clear the path for new bio-medical applications. These potential applications could include the medium-term deployment into small vessels for drug delivery[33] or sensing[92,192], without critical obstructions to blood flow.

This chapter first describes the fabrication of ISACs as well as their design in Section 4.1. Section 4.2 investigates their capabilities to deliver fluids, adapt their shapes, and manipulate microscopic objects. Finally, Section 4.3 reports the integration of magnetic sensors and introduces a purpose-developed strategy to track the location of ISACs. Parts

of the results presented in this Chapter have been published in the journal Science Advances (B. Rivkin, C. Becker, B. Singh, A. Aziz, F. Akbar, A. Egunov, D. D. Karnaushenko, R. Naumann, R. Schäfer, M. Medina Sánchez, D. Karnaushenko, O. G. Schmidt, 'Electronically integrated micro-catheters based on self-assembling polymer films', *Sci. Adv.* 7, 51, eabl5408, 2021) and reproduced under the terms of the creative commons license (CC-BY 4.0).

c Functionalities of Self-Assembled Integrated Micro-Catheters
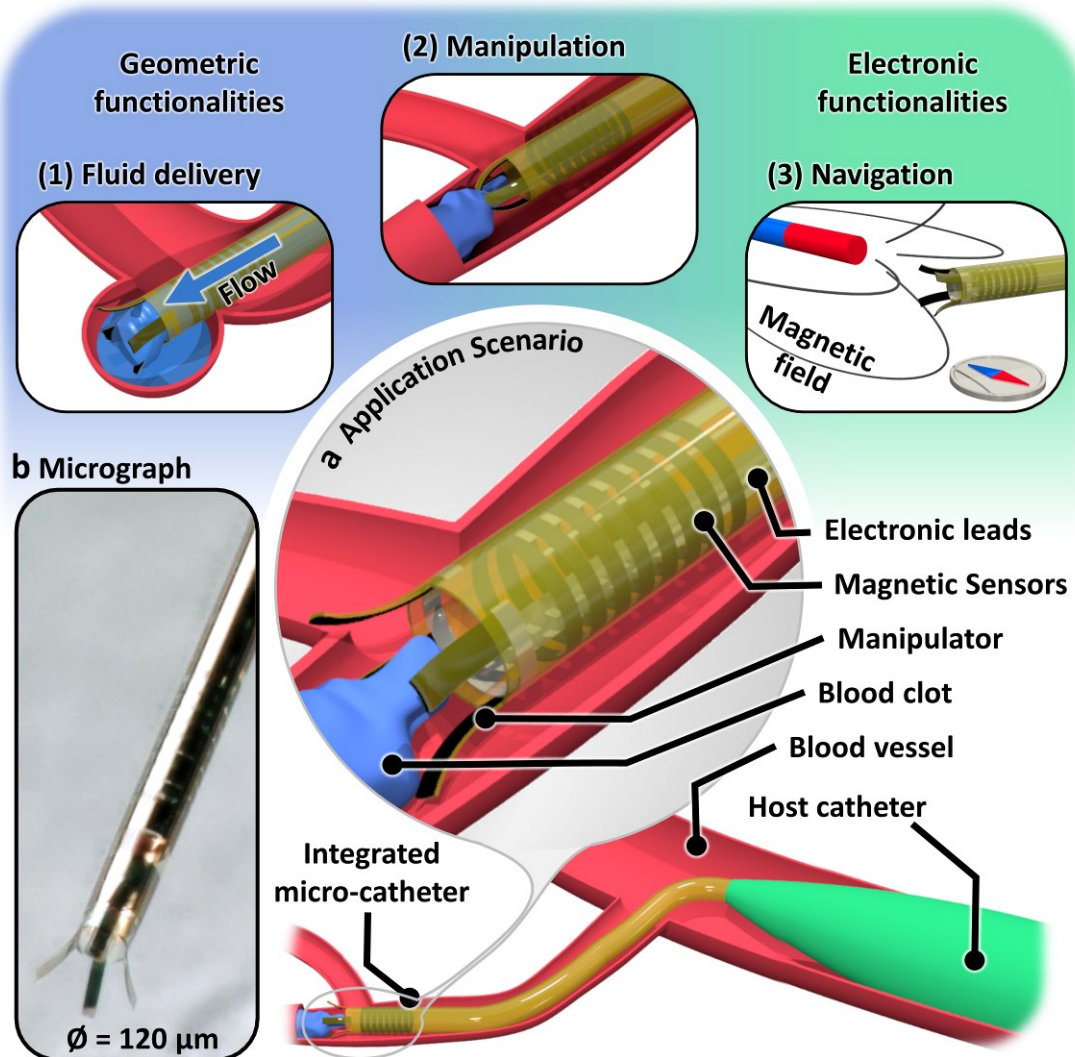
Figure 4.1: Concept of an integrated self-assemble micro-catheter: (a) ISACs integrate actuated opposing digits and a magnetic sensor. Both are operated with embedded electronic leads. During medical interventions, ISACs are deployed from a regular 'host' catheter that accommodates electronic and fluidic connections. **(b)** Micrograph showing tip of ⌀ 120 μm ISAC. **(c)** Three hypothetical application scenarios using integrated functionalities: (1) Liquid embolization of an aneurysm via targeted fluid delivery; (2) Micro-manipulator used to retrieve a blood clot; (3) Integrated magnetic sensor used as electronic compass for navigation. Figure adapted from [193].

4.1 DESIGN AND FABRICATION

ISACs are fabricated as planar stacks, comprising a diverse set of materials, before they self-assemble into completely free-standing, microscopically thin devices with various electronic components and functionalities.

4.1.1 FABRICATION AND SELF-ASSEMBLY

The fabrication of ISACs starts with the in-planar processing of shapeable polymer stacks (Sections 2.2.2) via photolithography (Section 3.2.1) onto cleaned glass substrates (50 x 50 mm^2). The SL (250 nm), HG layer (600 nm) and the first PI layer (600 nm) are patterned as depicted in Figure **4.2**a-1 to 3. These materials were introduced in Sections 3.1.1 to 3.1.3 and processing parameters can be found in the Appendix A1. Magnetic multi-layer stacks that are later used as part of the AMR sensors (Section 2.3.1) are processed with a combination of a lift-off process and plasma sputter deposition. The specific composition will be discussed in Section 4.3.1. The magnetic structures are followed by a single $Ti^{4\,nm}/Au^{30\,nm}$ bi-layer that is processed via lift-off and e-beam deposition, finalizing the AMR sensor, and at the same time forming electrodes for the micro-manipulator and electronic interconnects (Figure **4.2**a-4). The samples are coated with continuous ultra-thin yet pin-hole free layers of Al_2O_3 (20 nm) using ALD (Section 3.2.4) before and after the metal structures are processed. This sandwich configuration proved indispensable to protect the magnetic stacks from corrosion during later fabrication steps, to establish reliable electrical and chemical insulation, and extend their lifetime. Then, a second PI layer (600 nm) is processed on top of the isolated metallic components (Figure **4.2**a-5), which serves a dual purpose: First, it additionally isolates and protects the sensitive metal components. Secondly, the neutral plane of the entire stack is shifted close to the interface of the two PI layers, where the metallic components are located. By reducing the strain on this plane, the effect on the electronics is minimized while the self-assembly is rendered more efficient. The processing of protective layers is followed by selectively etching the Al_2O_3 insulating layer with a diluted organic base (tetramethyl ammoniumhydroxide, 2.7 %) for 20 min, where the second PI layer serves as masking layer. Then, the glass substrate is diced and samples are electrically connected by hot pressure bonding with anisotropic conductive film (ACF) and custom-designed flex cables. To deposit PPy onto the digits of the micro-manipulator (Figure **4.2**a-6), the still flat samples are connected as working electrodes in a three-electrode electro-chemical

cell and electro-polymerization is carried out following the adapted procedure introduced in Section 3.2.5. In the case of ISAC digits, the deposition voltage was adjusted to 520 mV, yielding layers of 2.4 μm after 27 s where a total charge of $8.2 \cdot 10^{-8}$ mA s was transported.
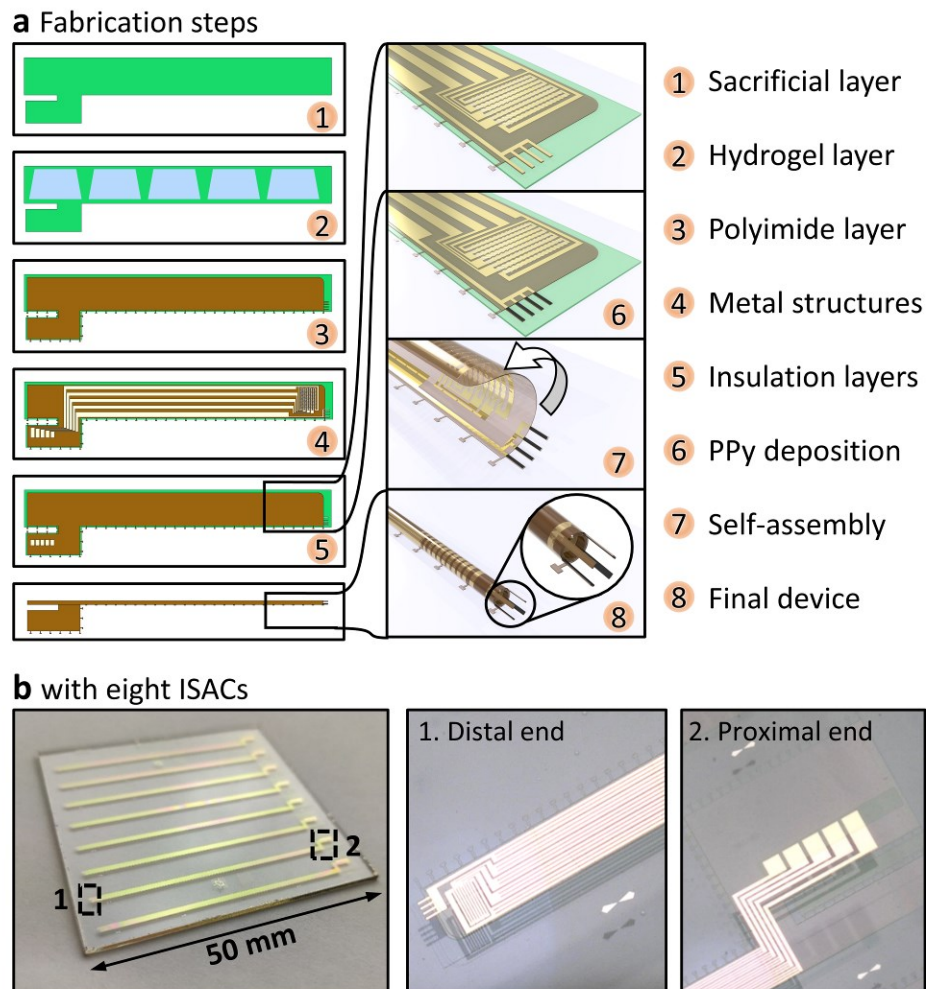

Figure 4.2: In-planar fabrication and self-assembly of ISACs: (a) Fabrication routine including in-planar thin-film processing and self-assembly. **(b)** Image of 50 x 50 mm^2 glass wafer with eight ISACs in their planar state. Figure adapted from [193].

After the planar fabrication is finalized with the deposition of PPy, the transformation of flat samples into 3D micro-catheters was realized with a series of treatments. First, the SL is selectively removed in diluted hydrochloric acid (HCl, 2 %$_{vol.}$), Then, the samples are rinsed with DI water and transferred into a basic solution to adjust the diameter of ISACs, taking advantage of the pH sensitivity of the swelling HG to fine-tune the geometry of the rolled-up tubes (Figure **4.2**a-7). Once the desired shape is achieved (Figure **4.2**a-8), rolled-up samples are taken out of the solution and immediately fixated with a spray-coated layer of camphor. It is applied using a regular spray head and a super-saturated solution of camphor in acetone and water (13:9:4 mass ratio). Upon spray coating, the camphor forms a continuous film on the rolled-up catheter and the

handling substrate instantly. It locks the shape of ISACs during the evaporation of water, preventing undesired shape changes such as unrolling that can occur due to strong capillary forces. After the complete evaporation of water, camphor sublimates within the next 6 hours to reveal tightly rolled tubes. After complete drying, rolled-up catheters are stable and do not unroll neither in air nor in aqueous solutions.

This fabrication scheme relies on standard manufacturing processes as they are commonly encountered throughout the electronic and semi-conductor industries, allowing to fabricate ISACs in parallel on a wafer scale (Figure **4.2**b).

4.1.2 FEATURES AND DESIGN CONSIDERATIONS

An image of a planar device prior to self-assembly is displayed in Figure **4.3**a. The self-rolling part has a length of just under 50 mm and a width of about 1 mm (Figure **4.3**a-1), although ISACs with lengths of 70 mm were fabricated as well. Four Au stripes (200 x 30 μm^2) that are supported with PI from the bottom and plated with PPy from top are located at the distal end (Figure **4.3**a-2). The patterned Al_2O_3 and PI protective layers are designed to leave only the deposition areas uncovered, thereby acting as masking layers during electro-polymerization. The stripes are distributed with a pitch of 90 μm to form opposing digits after roll-up into tubes with diameters of 100 μm to 120 μm. The second electronic components, namely the magnetic sensor, is located close to the distal end as well. It comprises eight AMR magnetic stripes (600 x 25 μm^2) which pairwise form the four arms of a Wheatstone bridge. Metal traces (Figure **4.3**a-3) connect the electronic components at the distal end to a total of five bonding pads that are located close to the proximal end, allowing to establish electronic connections. The metal traces are distributed over the entire width of the polymer stack to avoid local imbalances during self-rolling and each is split into three thinner stripes to reduce mechanical resistance to rolling and generate redundancy. Thin PI stripes reach over the SL to connect the polymer stack to the handling substrate. These so-called 'anchors' control the self-rolling direction (from left to right in Figure **4.3**a) and prevent the premature release of the devices from the handling substrate. They are easily cut after the fabrication of ISACs is finalized and connections are established. The swelling HG layer, that is located underneath the PI, is patterned with trapezoidal gaps (Figure **4.3**a-3). This micro-structure distributes the HG such that outer windings of the Swiss-roll architecture experience a higher rolling strain compared to the innermost windings and improves the stability and integrity of rolled-up tubes. The proximal end of ISACs is dedicated for

electronic and fluidic connections. The electronic contact area is an appendix to the self-rolling part of the ISAC (Figure **4.3**a-4) and remains flat during self-assembly. It carries five contact pads, relating to four terminals of the magnetic sensor and one actuator electrode.
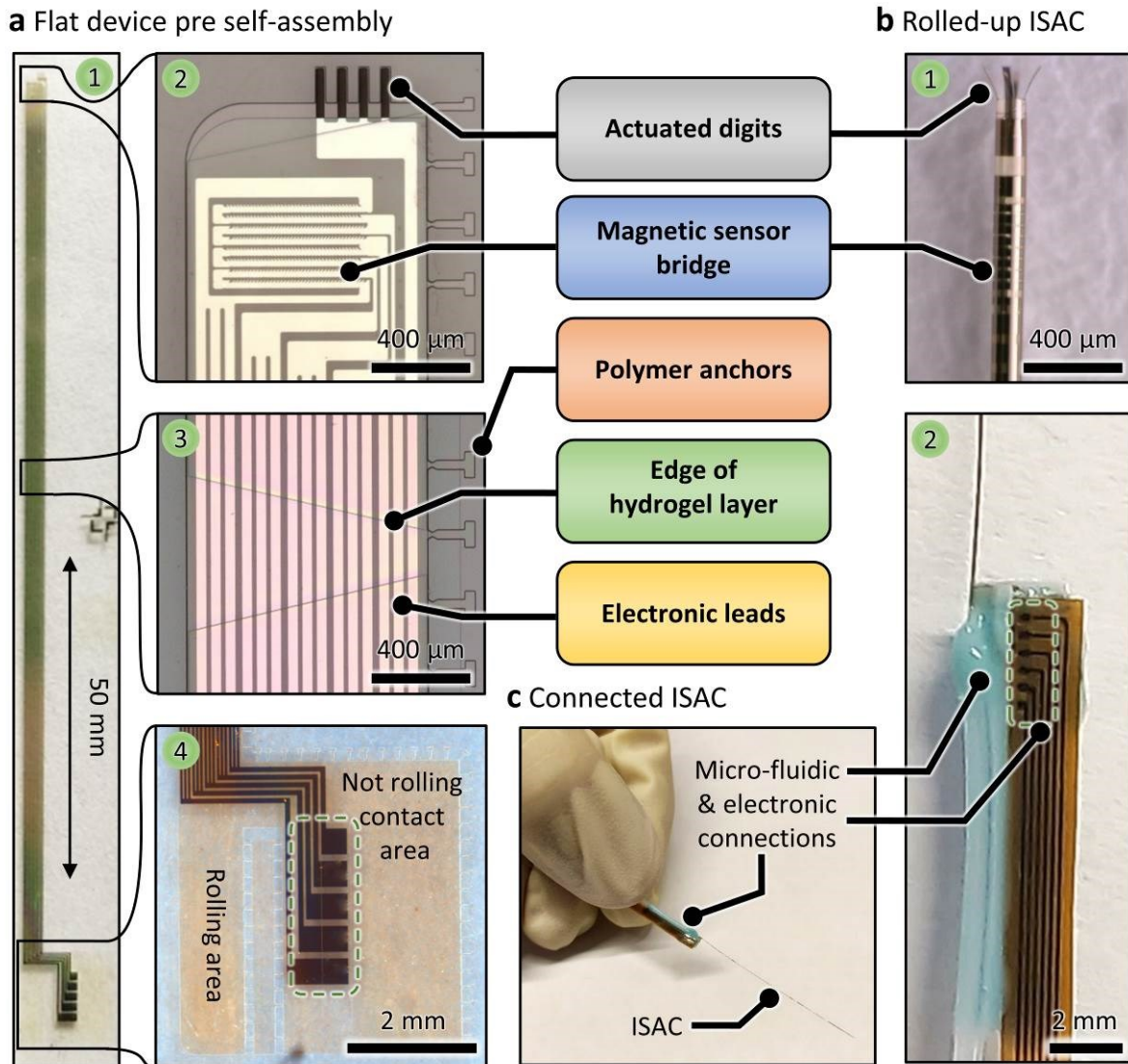

Figure 4.3: Integrated features of ISACs: (a) Planar device before self-assembly. **(b)** Rolled-up ISAC. **(c)** Finalized and released device with electronic and fluidic connections. Figure adapted from [193].

The self-assembly of these polymer stacks results in ISACs with diameters between 100 µm and 120 µm as displayed in Figure **4.3**b-1. The original width of 1 mm translates to 3 windings, which proved to be a decent compromise between stability and flexibility. It should be noted that, due to the several windings, such a Swiss-roll tube has a multiple of the usable surface area compared to regular tubes, allowing the accommodation of more electronic components. For ISACs, the shape-transformation is important in several ways: (i) The channel for fluidic transport forms naturally. (ii) The actuated stripes are

reoriented to oppose each other and form a micro-manipulator. Opposing digits can drastically improve grasping capabilities as it is commonly observed in technical and natural settings, e.g. in the opposable thumb of human hands. (iii) The initially planar stripes of the AMR sensor are re-shaped to a ring, or more precisely, a spiral shape, which is critical for correct perception of magnetic fields distributed in 3D. (iv) Through roll-up into tubes, the ultra-thin and flexible polymer stacks gain the structural integrity that is indispensable to handle these free-standing devices in water and air.

4.1.3 ELECTRONIC AND FLUIDIC CONNECTIONS

In order to establish electronic connections for sensor and actuator operation, custom designed flex cables (thickness: 100 μm, length 10 cm) are hot press bonded with ACF to the connection area at the proximal end of ISACs prior to self-assembly. The fluidic connection is established by putting a commercial micro-fluidics tube (outer diameter: 0.7 mm) over the free-standing proximal tip of the ISAC. Medical-grade two-component adhesive is applied to seal the connecting site and partially glue the tubing to the flex cable (Figure **4.3**b-2). ISACs are then finalized by releasing the connected catheters from the handling substrate by carefully peeling it off or scratching the anchors. ISACs are sufficiently stable to be handled manually and remain straight if not loaded externally (Figure **4.3**c).

4.2 INTEGRATED FEATURES AND FUNCTIONALITIES

4.2.1 FLUIDIC TRANSPORT

ISACs with attached fluidic tubing are readily connected to pumps or syringes and used for the targeted delivery of liquid payloads. The flow transport through ISACs was characterized with a precise pressure pump (Biophysical tools, Germany). Model liquids with different viscosities (Table **4.1**) were prepared as described in Section 3.3.4. Pressures ranging from 40 mbar to 160 mbar were applied to a reservoir from where the liquid would flow through the connecting tubing and the ISAC. The weight of the reservoir was measured to monitor the mass of the transported liquid after 10 min, which was converted into a volume flow per time as summarized in Figure **4.4**. As expected from the Hagen-Poiseuille law, the flow increases linearly with increasing pressure and decreases with higher viscosity. The resulting pressure-dependent flow rates were fitted with a linear model to obtain pressure-normalized flow rates as summarized in Table **4.1**, yielding for instance a value of 14.6 nL s^{-1} mPa^{-1} for pure water.
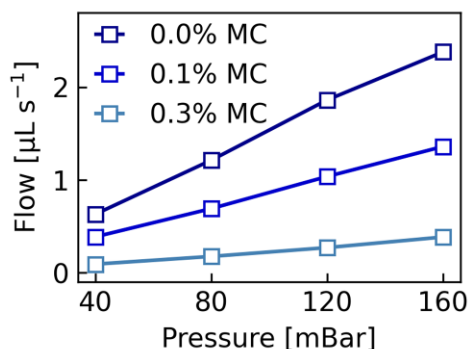
Figure 4.4: Flow rate through ISAC: Model fluids with difference viscosities were pumped through ISACs with controlled pressure. Figure adapted from [193].

The obtained values imply the possibility to transport fluids with at least micro-liter precision, leading to interesting applications regarding micro-dosing, for instance the delivery of chemotherapeutic agents into microscopic feeding vessels of tumors[33]. The investigation with liquids with various viscosities hints at the wide range of fluids that can be transported, both for the delivery of drugs and the harvesting of body fluids (blood, gastrointestinal fluids, salvia, urine, oviduct fluid). For instance, the typical viscosity of blood is about ~ 4 mPa s at relevant shear rates[194] .

Table 4.1: Rate of fluid transport through ISACs

Solution No	MC content [%$_{mass}$]	Viscosity [mPa s]	Flow per pressure (measured) [nL s^{-1} mPa^{-1}]
1	0.0	~ 1	14.6
2	0.1	~ 2	8.1
3	0.3	~ 5	2.4

The delivery of fluids into target sites is desired for a variety of medical treatments. Localized administration of small drug doses is advantageous to avoid dilution, or because the delivered agent undergoes immediate changes when once it is in contact with the environment. The latter applies, e.g., for liquid embolic agents that solidify as soon as they are delivered into a blood vessel. The targeted delivery of liquid payloads using catheters generally comprises several steps as schematically depicted in Figure **4.5**a: Starting from a remote location (1), the catheter is moved towards and inserted into the target cavity (2). The payload is transported (3) and the catheter is retracted from the site (4), while the payload remains in place. This process was demonstrated with an ISAC inside a narrow artificial model channel (0.2 mm) that was milled into a block of polymethacrylate acid (PMMA). As displayed in Figure **4.5**b-1, the channel was modified with a round defect, the 'aneurysm', with a diameter of 1 mm and a narrow opening of only 0.6 mm.

This specific defect dimensions are of interest because aneurysms with such small sizes can be especially difficult to treat with conventional clinical catheters[40,195]. Figure **4.5**b-1 to 4 display the targeted delivery of a dyed fluid into the aneurysm model. An ISAC is manually inserted through the channel and into the target site. The liquid payload, which represents e.g. a liquid embolic material, is pumped into the defect for 5 s to fill it completely and the ISAC is retracted out of the defect and the channel. A small amount of dyed fluid spilled out of the target site and into the channel due to the imprecise manual application of pumping pressure. This was corrected by applying negative pressure and sucking the excess liquid back into the ISAC, effectively demonstrating liquid biopsy in the process.
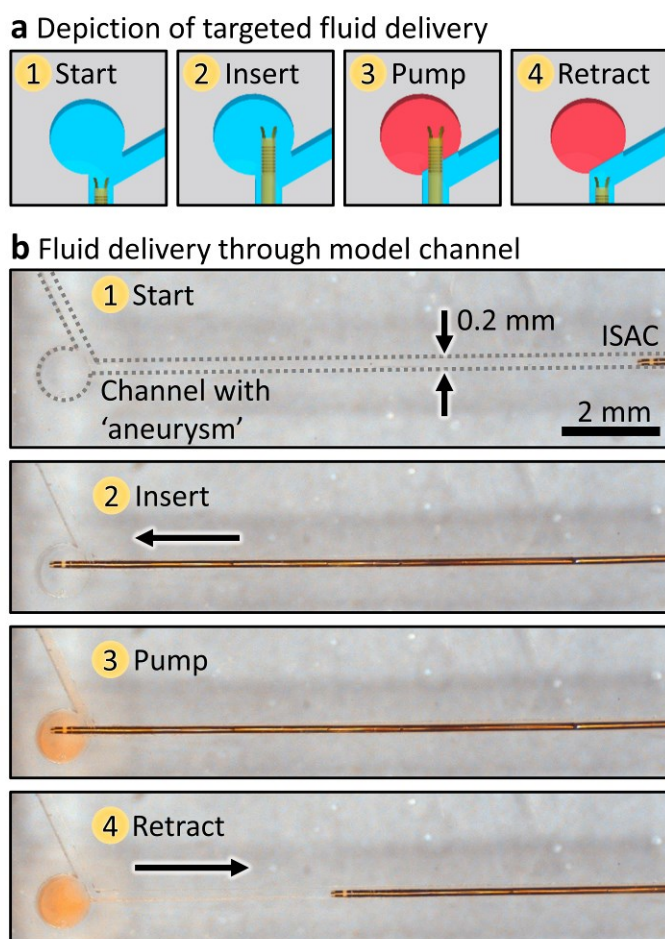
Figure 4.5: Targeted fluid delivery in model channel: (a) Steps involved in targeted fluid delivery with catheters. **(b)** Delivery of dyed fluid with an ISAC through a model channel into a target cavity. Figure adapted from [193].

While the ISAC remained straight throughout the demonstration of targeted fluid delivery, real environments require catheters to bend in order to maneuver tortuous vessels. The capability of ISACs to bend and adapt their shape was demonstrated in a second model environment. Micro-fluidic tubing (ø 0.9 mm) was adjusted around a

cylinder (ø 10 mm), creating a channel with a curvature radius of about 6 mm (Figure **4.6**). An ISAC was manually introduced into this curved channel. As the images in Figure **4.6** show, the device seamlessly adjusts to the curved channel geometry upon insertion. When retracted, it returns to its initial straight shape. The insertion was carried out repeatedly with no observable alteration of device properties. Moreover, it confirms that ISACs can transfer sufficient force along their length to be inserted into narrow channels where they can even curve to 180°, which is a key prerequisite for maneuvering biological anatomies. The flow rate was tested as discussed above using such a curved ISAC. Compared to the rate in its straight shape, no significant difference (219.0 ± 2.0 μL straight vs 218.7 ± 0.6 μL curved) could be found after three runs for each shape.
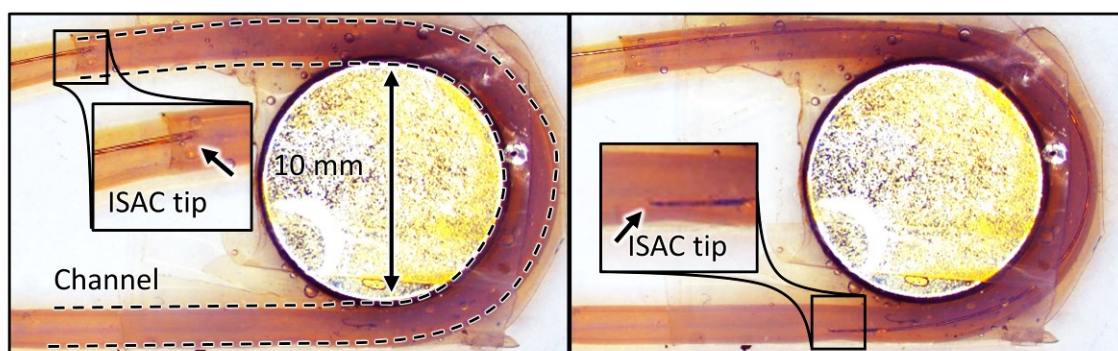
Figure 4.6: Insertion into curved model channel: An ISAC is repeatedly inserted into a curve microchannel to inject a liquid payload. Figure adapted from [193].

Regarding future applications, ISACs are expected to reliably perform in diverse physiological environments. The gastrointestinal tract is a possible target for minimally invasive catheter interventions. The fluid delivery capabilities of ISACs were further investigated in a more realistic environment, namely the esophagus and stomach that was retrieved from a mouse model. The organs were extracted as described in Section 3.3.4 and mounted on a rubber substrate using thin copper wires (Figure **4.7**a). An ISAC was introduced manually into the esophagus, which had an inner diameter of less than 0.7 mm, and maneuvered into the stomach. Once inside the target location, a fluorescent dye was injected through the ISAC. It distributed in the first section of the two-part rodent stomach and the esophagus. Figure **4.7**b shows the final scene under blue light.
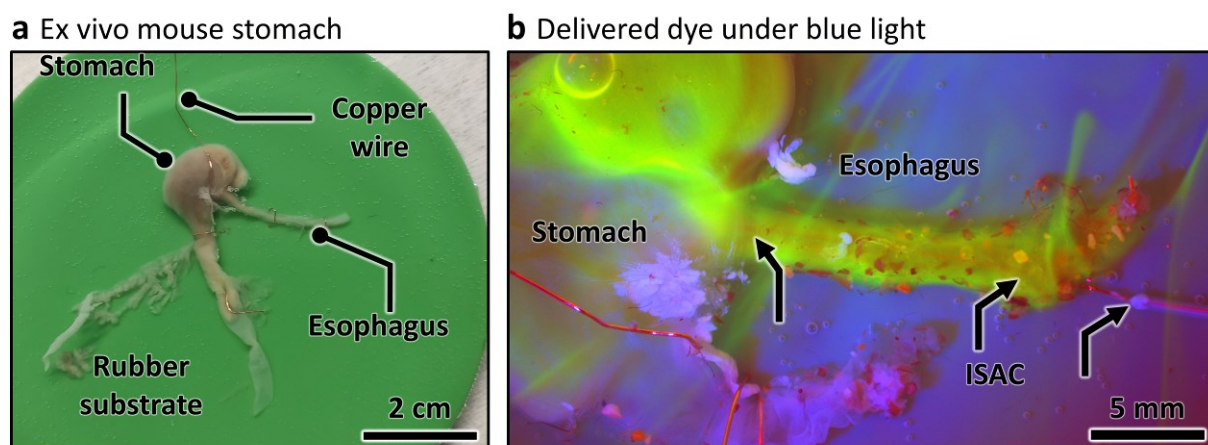
Figure 4.7: Targeted fluid delivery in ex vivo mouse stomach: (a) Mounted *ex vivo* mouse model stomach with esophagus. **(b)** Fluorescent dye that was delivered into the *ex vivo* stomach is visible under blue light. The ISAC used for delivery is still inside the esophagus. Figure adapted from [193].

4.2.2 BENDING STABILITY

In future minimally invasive interventions, ISACs will be deployed in tortuous vessel systems where they must comply with the intricate channels present in human anatomy. Specifically, ISACs have to deform to different bending angles, ideally without structural fatigue, damage to electronic components, or other critical failures, including unrolling. Attention should be given to the effect of kinking, which can occur as a result of mishandling and should not render the instrument unusable immediately.

The mechanical robustness of ISACs was assessed with an automated setup, where the device first was fixated using a static holder and then bent with a small dynamic strap that was actuated with a linear motor. The mechanical stability of the polymer platform was subject to the first investigation. First, the ISAC was bent by 30° such that all bending focused in one kink to maximize the strain on the material and a dyed fluid was pumped through it. Optical assessment with a microscope showed a stream of ejected colored water, but no leakage at other sites (Figure **4.8**a), thereby confirming that the Swiss-roll architecture neither unrolls nor breaks upon kinking. Next, the dynamic strap was adjusted to repeatedly bend the ISAC to 30°, 60°, and 80° (Figure **4.8**b). The integrity of the polymer tube wall was tested regularly again by pumping a dyed fluid through the ISAC. Optical assessments showed no indication of structural fatigue that would lead to leakage, even after 2000 actuation cycles.
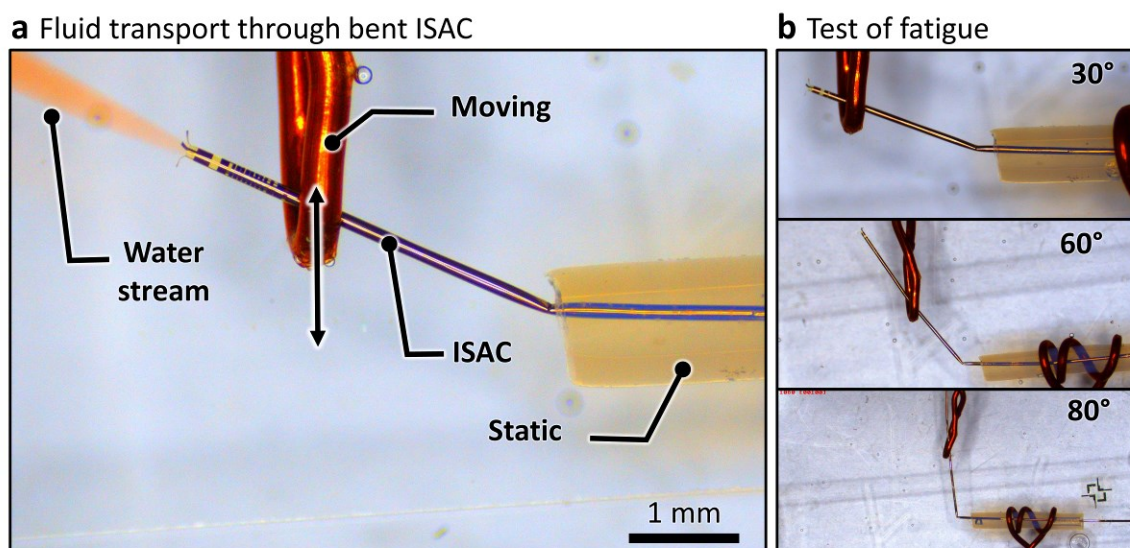
a Fluid transport through bent ISAC

Moving

Water stream

ISAC

Static

1 mm

b Test of fatigue

30°

60°

80°

Figure 4.8: Structural stability under bending: (a) A dyed liquid is pumped through a bent ISAC. **(b)** An ISAC is bent to various angles for 2000 times without catastrophic failure. Figure adapted from [193].

Moreover, ISACs rely on metal traces that serve as electronic leads and connect actuators and sensors to external electronics. Alongside the polymer platform, these metal structures will be subject to repeated bending. Their stability was investigated with the same setup as discussed above. Here, an ISAC was deformed to reach gradual bending (Figure **4.9**a) with specific curvature radii (Figure **4.9**b), namely 13 mm, 6.5 mm, 4.5 mm, and 0 mm, where the latter corresponds again to a sharp kink at a single spot. The resistance of the same metal trace that ran from the base of the ISAC to its tip, and back, was measured after each of 2000 actuation cycles. Figure **4.9**c displays the relative increase of the electrode resistance for selected actuation cycles. When the ISAC is bent gradually, the resistance remains almost unchanged, increasing just minorly by less than 1 ‰. Only when it is kinked at a single site, a notable trend arises, and the resistance increases by still a small ratio of less than 4 ‰. This miniscule degradation is achieved through the design of ISACs. For one, the ultra-thin polymer layers develop only small strains on their surfaces upon bending. Moreover, the metal traces are located in the center of the PI double layer, where they are close to the neutral plain and are not subjected to strain. The minor degradation trend is likely caused by imprecisely defined layer thicknesses and might arise from the formation of microscopic cracks inside the metal trace[68]. If necessary, the durability of metallic components could be improved through the application of dedicated shapes and patterns, as they are employed in flexible and stretchable electronics[14]. Based on this study and regarding the harsh testing

conditions, however, the stability of integrated metal traces does not appear to be a limiting factor.
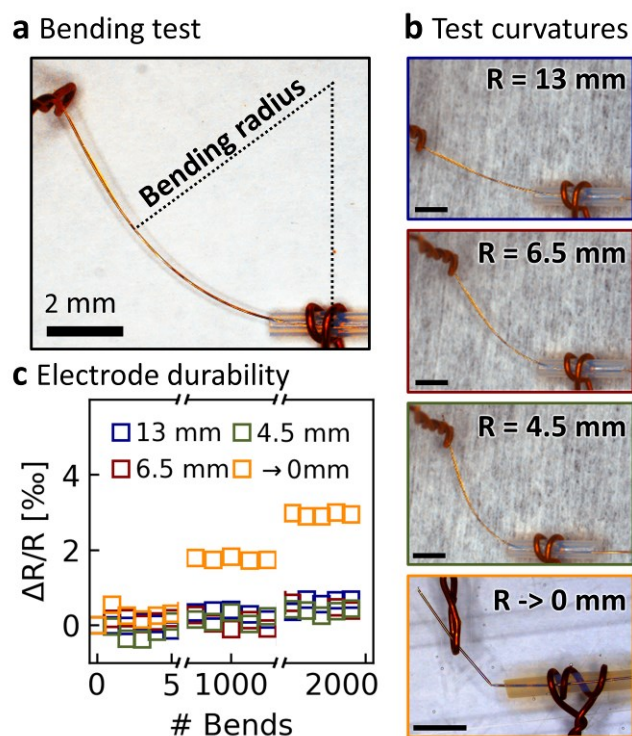

Figure 4.9: Stability of metal traces under bending: (a) Definition of the curvature or bending radius. **(b)** An ISAC is bent to different curvatures. Scalebars indicate 2 mm. **(c)** Relative increase of metal trace resistance during repeated bending to various curvatures. Figure adapted from [193].

4.2.3 ACTUATED MICRO-MANIPULATOR

Manipulation tasks are commonly part of clinical catheter interventions and can include the installation of implants, biopsies, or retrieval of tissues and objects, e.g. blood clots. In clinical applications, this is achieved by maneuvering a catheter close to the site of interest before it is used to introduce a separate tool, e.g. a wire. In contrast, ISACs carry an integrated tool for micro-manipulation that is located at their distal tip. It comprises four digits that are processed during the in-planar fabrication (Figure **4.10**a) and selectively coated with PPy. During the self-rolling process, they are re-arranged to oppose each other pair-wise. The manipulator can then be opened and closed in a controlled way (Figure **4.10**b) by applying small bias voltages to PPy, where the CP swells when reduced at -1 V (opening) and shrinks when oxidized at 0 V (closing). Here, all biases are denoted vs a Ag/AgCl reference. The opening and closing behavior was quantitatively investigated by measuring the digit distance during one actuation cycle as depicted in Figure **4.10**c, where 100% open corresponds to the digit distance in Figure **4.10**b 'open', and 0% open corresponds to the touching finger tips in Figure **4.10**b 'closed'. The transition from a fully

closed to fully open state requires less than 5 s, while the closing is accomplished in about 6 s. It should be noted that the speed of actuation is mostly determined by the rate of bias voltage change, which is adjusted conservatively to 100 mV s^{-1} in this experiment and can be increased if necessary.
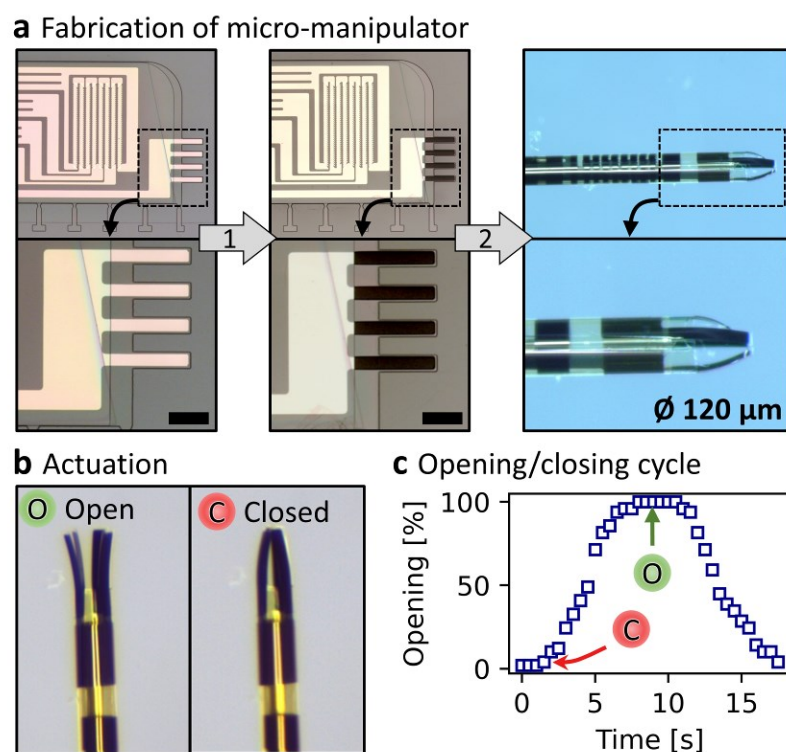

Figure 4.10: Actuated micro-manipulator: (a) Fabrication steps: (1) Deposition of PPy and (2) self-assembly. Scale bars indicate 100 μm. **(b)** Micro-manipulator at the tip of ISACs in opened (O) and close (C) state. ISAC diameter is 110 μm. **(c)** Opening and closing cycle of an integrated micro-manipulator. Figure adapted from [193].

PPy actuators are not only fast, precise, and biocompatible, but also soft. These properties make such a manipulator ideal to grasp and move delicate tissues. For instance, retrieving single cells or tissue sampled from narrow channels might be of interest for analysis or treatment. Such a capability of ISACs to retrieve microscopic objects out of narrow channels was demonstrated using a polystyrene micro-particle (∅ 100 μm) and an artificial channel (0.4 mm) milled in PMMA. Figure **4.11** depicts a series of micrographs showing the process: An ISAC is manually introduced into the channel (1) and maneuvered towards the target (2). The negative bias voltage was applied to open the manipulator (3), which is then aligned with the particle (4). The bias is removed to close the digits (5) and firmly secure particle, before the ISAC is retracted out of the channel with the cargo (6 and 7).
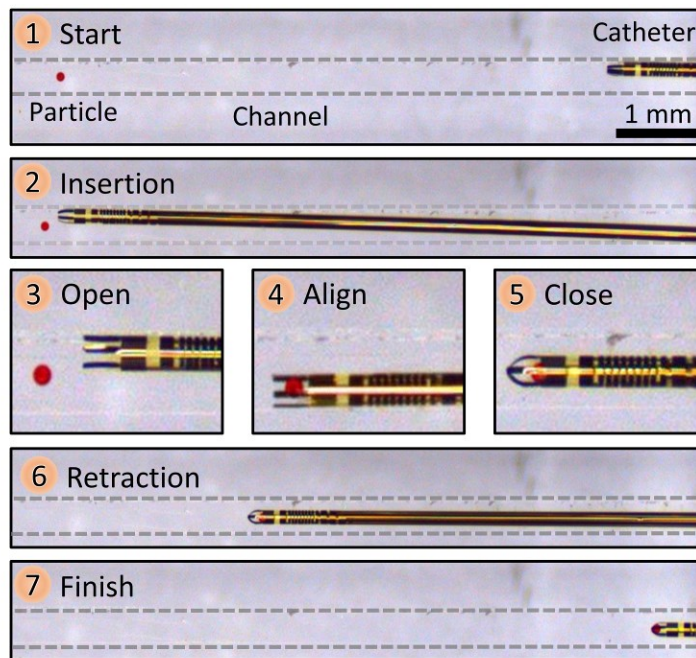
Figure 4.11: Retrieval of particle from channel using integrated micro-manipulator: Series of micrographs display how the target object is approached, grasped, and retrieved out of the channel. Figure adapted from [193].

4.3 MAGNETIC POSITION TRACKING

The demonstrations of fluidic delivery and manipulation in Section 4.2 required constant observations to locate ISACs through a microscope. Similarly, state-of-the-art minimally invasive interventions often rely on X-ray-based techniques, such as fluoroscopy, to monitor the propagation of surgical tools within the patient. The repeated exposure to ionizing radiation, however, imposes a health hazard onto patients as well as the medical practitioners[196,197]. A safer alternative is offered by EMT[35,51], as discussed in Section 2.1.1. To enable harmless navigation, the location of medical tools can be determined with electro-magnetic sensors and digitally embedded into high-resolution 3D anatomic maps that are obtained by medical imaging techniques, e.g. magnetic resonance imaging or computed tomography. In this thesis, ISACs with the capability for magnetic tracking are developed. First, a magnetic sensor that is suitable regarding sensitivity, measurement range, geometric restrictions, and integrability is developed (Section 4.3.1) and demonstrated in a simple positioning task (Section 4.3.2). ISACs constitute a fundamentally novel tool and might lead to new medical applications. To take full advantage of its unique properties, a specialized tracking strategy is developed which aims to complement existing EMT approaches. The theoretical groundwork is developed in Section 4.3.3, which is experimentally realized and evaluated in Section 4.3.4 and Section 4.3.5. A discussion on the limitations of this approach and the current

implementation, as well as perspectives regarding future developments are provided in Section 4.3.6.

4.3.1 INTEGRATED MAGNETIC SENSOR

A variety of magnetic and inductive sensors based on the self-rolling shapeable polymer stack have been previously demonstrated, including GMI sensors[27], GMR sensors[125], and antennas[28]. The selection of an optimal sensor type for the magnetic tracking of ISACs should consider several aspects: (i) The sensor should operate at low frequencies and field strengths to enable ISAC navigation that is secure and bio-compatible. (ii) The geometry of the sensor should be dictated by the requirements of the ISAC platform, not vice versa. Therefore, inductive sensors that impose limitations on size and geometry should be avoided. (iii) Due to the rotational symmetry of ISACs, the sensor should enable tracking with 5 DOF. These are parallel displacements in the three spatial directions and rotations orthogonal to the long axis of ISACs.

Taking these requirements into account, AMR sensors (Section 2.3.1) were chosen, as they can be optimized to achieve high sensitivity for low-frequency magnetic fields[168] while imposing little constrains on size and geometry. AMR sensors were integrated close to the distal tip of ISACs as illustrated in Figure **4.12**a. NiFe was chosen as soft magnetic material, as it is well-studied and has proven itself throughout academia[168,170,198] and industry[166,167]. AMR sensors require an induced anisotropy. Commercial integrated circuits with AMR sensors commonly rely on inductive coils (set/reset coils) that generate magnetic stabilization fields or set/reset pulses for this purpose[169,173]. Regarding the desired integration into a thin-film micro-system, such additional components are not feasible. Instead, the AMR sensors in this work rely on an additional aFM pinning layer $IrMn^{10\,nm}$, similar to previous reports[170,198]. The full magnetic stack then reads $Ta^{5\,nm}/NiFe^{2\,nm}/IrMn^{10\,nm}/NiFe^{X\,nm}$ (Figure **4.12**b), where X indicates the layer thickness of NiFe that remains to be optimized. The sensor comprises a total of eight magnetic stripes ($600 \times 25\ \mu m^2$) that are processed via sputter deposition ($2.4 \cdot 10^{-6}$ mbar base pressure, $1.4 \cdot 10^{-3}$ mbar Ar atmosphere) and patterned through a standard lift-off process. The deposition is carried out in a homogeneous magnetic field (25 mT) to define the pinning direction permanently along the long axis of the stripes and orthogonal to the long axis of the ISAC. The sensors were finalized with BP stripes (5 μm width, 5 μm gaps) and interconnects, both processed via e-beam deposition of Ti^{4nm}/Au^{30nm} and lift-off

patterning. The AMR sensors developed in this thesis were conceptualized, fabricated, and optimized in collaboration with Christian Becker (Leibniz IFW Dresden).
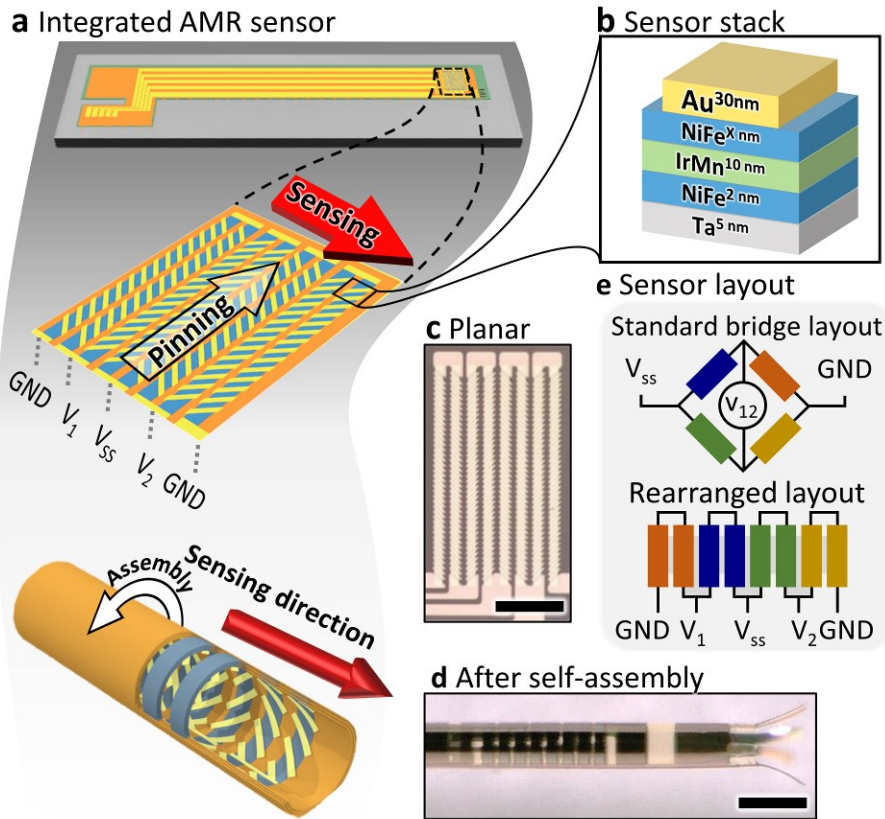

Figure 4.12: Integrated anisotropic magnetoresistance sensor: (a) Magnetic stacks are processed at the distal end, connected in a Wheatstone bridge arrangement, and self-rolled to sense magnetic fields parallel to the ISAC. **(b)** AMR sensor layer stack. **(c)** Planar AMR sensor. Scale bar indicates 200 µm. **(d)** Rolled-up AMR sensor at ISAC tip. Scale bar indicates 200 µm. **(e)** Rearranged layout of Wheatstone bridge configuration used for integrated AMR sensors. AMR sensors were developed in collaboration with Christian Becker (Leibniz IFW Dresden). Figure adapted from [193].

A micrograph of an AMR sensor in its planar state is displayed in Figure **4.12**c. During self-assembly, the AMR sensors are reshaped to form Swiss-roll rings, or spirals, as depicted in the schematic in Figure **4.12**a and the micrograph in Figure **4.12**d. After self-assembly, integrated AMR sensors have a tiny size of 375 µm in length and 120 µm in diameter. As discussed in Section 2.3.1, AMR sensors perceive only the component of an external magnetic field, that is orthogonal to its anisotropy direction. Consequently, the sensors developed in this work only perceive magnetic field components that are parallel to the long axis of ISACs due to the magnetic pinning along the magnetic stripes. This design is advantageous, since such integrated sensors are not affected by the rotation of ISACs around their long axis. Moreover, diameter variations due to manufacturing imperfections, which can be limiting for other sensor designs[125], are inconsequential in this arrangement. The eight stripes are connected in a Wheatstone bride configuration

such that neighboring stripes pairwise form the four arms of the Wheatstone bridge circuit (Figure **4.12**e).

Prior to their application in ISAC tracking, AMR sensors were optimized regarding their sensitivity and operational range by tuning the thickness of the soft magnetic NiFe layer. Sensor optimization was carried out using model devices that were processed in planar (Figure **4.13**a) before self-rolling to Swiss-roll tubes (Figure **4.13**b) like ISACs, but were much shorter to allow the parallel fabrication of 72 individual sensors on 25 x 25 mm^2 substrates. To gain an improved understanding of the material system, Kerr magnetometry (Section 3.3.1) was carried out to assess the exchange bias (pinning strength) induced by the pinning layer. Kerr-magnetometry was performed by Balram Singh (Leibniz IFW Dresden). Then, the AMR sensors were finalized with the roll-up step and underwent electro-magnetic characterization (Section 3.3.2). The response of AMR sensors was recorded during magnetic field sweeps inside a Helmholtz coil setup. Figure **4.13**c displays the response of the same sensor before and after self-assembly. Both curves display a linear regime around zero field, which peaks towards higher fields strengths as expected from AMR sensors in a Wheatstone bridge configuration (Section 2.3.1). The sensor sensitivity is defined as the slope of the linear regime and has the unit mV V^{-1} mT^{-1}, reading millivolt of signal per volt of bias voltage and per millitesla of external magnetic field. The sensor range is the strength of an external magnetic field below the signal peaks and inversions. The rolled-up AMR sensor has a lower, but still acceptable sensitivity compared to its planar state, possibly due to a magneto-mechanical interaction caused by the rolling strain[188]. Both curves show little noise and almost no hysteresis, suggesting a high quality of materials and their correct integration. The effect of NiFe layer thickness on sensor performance was systematically studied with a series of devices featuring NiFe layers ranging from 10 nm to 60 nm. Selected response curves are displayed in Figure **4.13**d, while the sensitivity of all devices is summarized in Figure **4.13**e. The sensitivity of AMR sensors increases with layer thickness and reaches an optimum at around 30 nm, peaking at 1.81 mV V^{-1} mT^{-1}. This behavior is related to the strength of the exchange bias, as revealed by Kerr magnetometry. As displayed in Figure **4.13**f and Figure **4.13**g, the exchange bias is highest for the thinnest NiFe layer, diminishes first very quickly for increasing layer thicknesses until 30 nm, after which it only changes slightly. In AMR sensors, weaker pinning leads to higher sensitivity since the magnetization of the soft FM layer is more easily rotated by external fields[172].
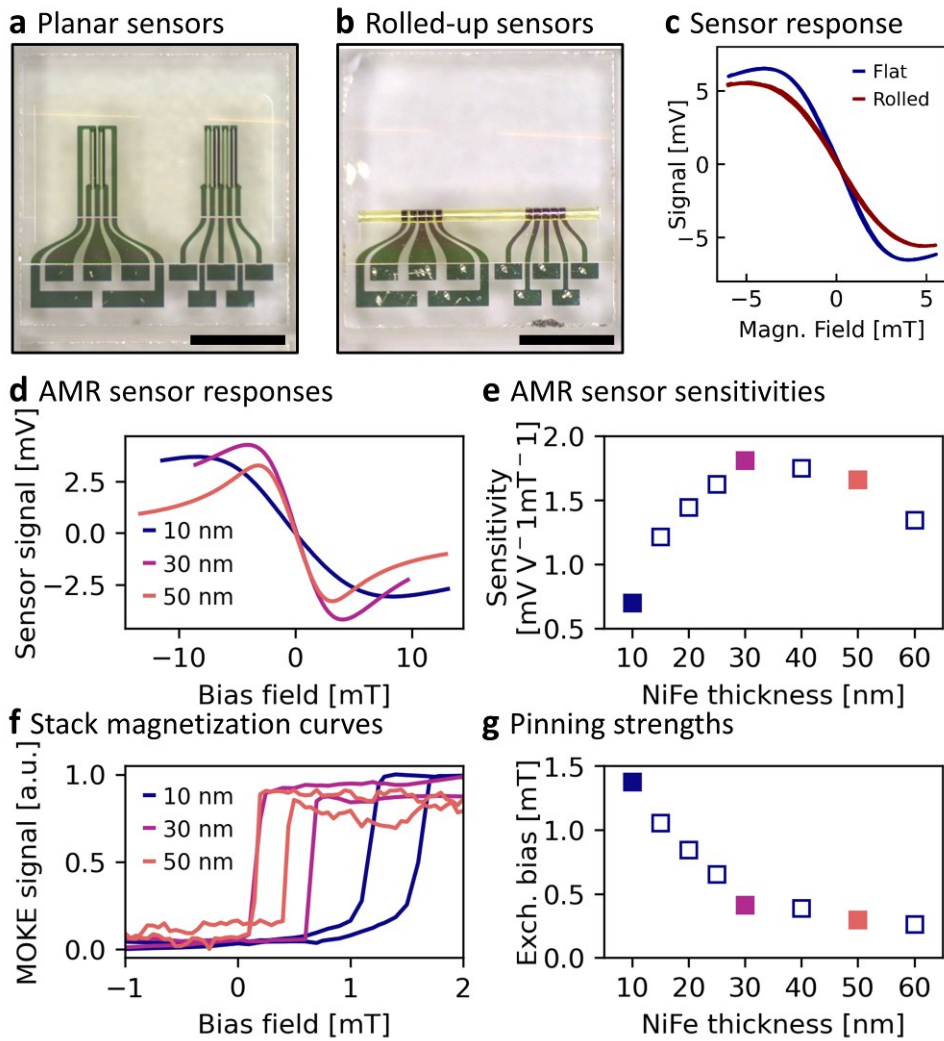
Figure 4.13: Optimization of integrated AMR sensors: (a) Model devices for sensor optimization in planar state. Scale bar indicates 1 mm. **(b)** Model device after roll-up. Scale bar indicates 1 mm. **(c)** Responses of the same AMR sensor in its planar and rolled-up shape. **(d)** Sensor responses of AMR sensors with different NiFe layer thicknesses. **(e)** Sensor sensitivities depending on NiFe layer thickness. **(f)** Magnetization curves of pinned NiFe layers with different thicknesses. **(g)** Exchange bias of pinned NiFe layer depending on layer thickness. AMR sensors were developed in collaboration with Christian Becker (Leibniz IFW Dresden). Kerr-magnetometry was performed by Balram Singh (Leibniz IFW Dresden). Figure adapted from [193].

The diminishing sensitivity for layer thicknesses above 30 nm that is suggested by Figure **4.13**e most likely originates from the current distribution inside the sensor stack: When the thickness of NiFe increases compared to the constant thickness of BP stripes, the current redirection through the Au is bypassed and an increasing portion of the current is conducted straight through the magnetic layer, instead on the desired zig-zag path. Since the straight current flow through NiFe is parallel in all stripes, it ceases to contribute to the differential signal of the Wheatstone bridge, thus reducing the sensitivity. Consequently, AMR sensors with NiFe layer thicknesses of 30 nm were found to be optimal for tracking applications in ISACs.

4.3.2 POSITION CONTROL WITH SENSOR FEEDBACK

Integrated AMR sensors immediately allow to carry out simple feedback driven positioning of ISACs. As shown in Figure **4.14**a, an ISAC was mounted on a holder that was attached to a software-controlled motorized linear stage. A constant DC bias of 2 V was applied to the sensor bridge and its output voltage was recorded, both using a PCB with integrated analog-to-digital (ADC) and digital-to-analog (DAC) converters. A permanent magnet was positioned about 1 cm beneath and 1 cm in front of the tip of the ISAC to provide a static reference magnetic field. The response of the AMR sensor was used as feedback in a PID control loop (Section 3.4.3) that controlled the linear motor position to maintain a constant distance between the magnet and the ISAC. As displayed in the series of images in Figure **4.14**b, a displacement of the reference magnet leads to a position adjustment of the ISAC through the software-controlled motor.
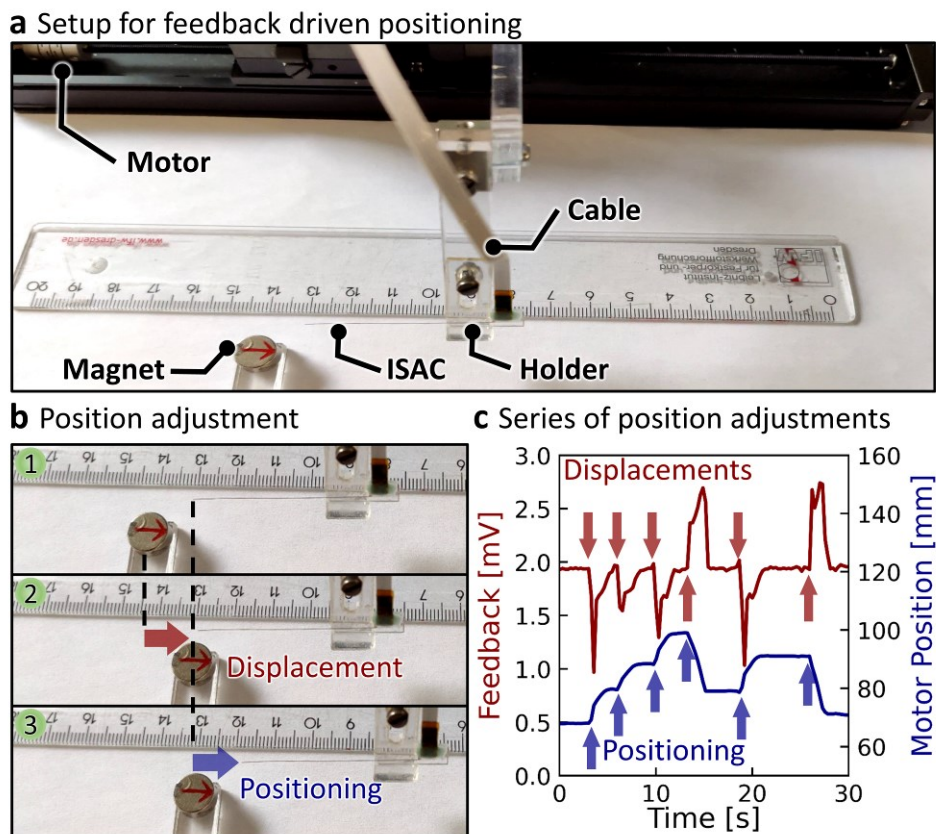
Figure 4.14: Positioning of ISAC with magnetic feedback: (a) Setup for magnetic feedback driven position control. **(b)** The field of a permanent magnet is detected by the integrated sensor and serves as reference. When the magnet is displaced, the motor automatically adjusts the position of the ISAC to maintain a constant distance to the magnet. **(c)** Feedback and output curves showing a series of displacements and position adjustments. Figure adapted from [193].

A series of displacements and readjustments was carried out and the corresponding feedback (sensor signal) and output (motor position) curves are displayed in

Figure **4.14**c. The control loop was implemented in Python to maintain the SP of the system at the initial sensor signal level, corresponding to 1.94 mV in the trial displayed in Figure **4.14**c. Whenever the magnet was displaced, the sensor feedback changed and an error in the order of 1 mV emerged as indicated by red arrows. The PID feedback loop then adjusted the output according to Equation 3.5. After a magnet displacement, the motor position was rapidly adjusted at first and slower when the desired distance was approached. A typical position adjustment of 10 mm took about 1.5 s and functioned correctly in both directions. The feedback loop operated with an update frequency of 4 Hz and the gain parameters (K_P = 4 mm mV^{-1}, K_I = K_D = 0) were adjusted heuristically.

4.3.3 INTRODUCTION OF MAGNETIC PHASE-ENCODED TRACKING

Static magnetic fields are sufficient for simple positioning tasks in one dimension, as demonstrated in the previous section. The navigation in 3D space with 5 DOF, however, requires a more complex reference frame that provides a higher information density. Alternating magnetic fields that change in time and space are suitable for this purpose. This section first identifies attractive application scenarios for ISACs and the requirements that these applications would impose on navigation. With these conditions in mind, a mathematical framework is developed that allows precise tracking of ISACs.

Intriguing applications of ISAC navigation should certainly target the cerebro-vascular system within the brain. Inside the human head, light or sound-based imaging techniques are mostly prohibited by the dense skull bone, available EMT probes might be too bulky to maneuver the intricate vessel network, and consequently, techniques that are based on X-rays remain the sole option for *in situ* imaging to date. To be successfully applied inside the human brain, the navigation of ISACs should offer a high tracking resolution ($\ll$ 1 mm), a relatively limited working volume about the size of a human head ($\sim$ 20 cm across), and relying solely on harmless magnetic fields.

The following paragraphs introduce the most fundamental form of position and orientation tracking: Tracking of parallel displacement along a line in 1d and rotation around a single axis. Perspectives on the generalization of these concepts to higher dimensions are provided in Section 4.3.6. and the mathematical framework for 5 DOF tracking is laid down in the Appendix A2.

First, the approach for *parallel displacement tracking* along one line is developed. The basic principle of this tracking approach, here named magnetic phase-encoded tracking,

is illustrated in Figure **4.15**. Two electro-magnetic coils, the so-called *sources*, are located on opposite sides of the working volume. The sources are supplied with two distinct driving currents to generate two alternating magnetic fields with equal strength and frequency, but with a 90° phase shift. The magnetic fields superimpose inside the working volume. The contribution of the individual sources to the superimposed field strongly depends on the exact position due to the distance dependent field decay of magnetic dipoles ($|\vec{B}| \sim r^{-3}$).
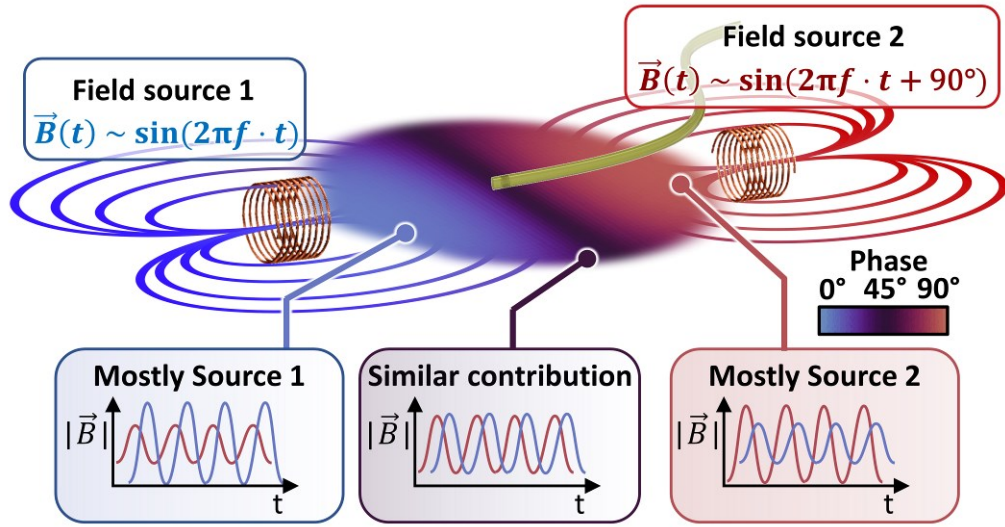
Figure 4.15: Working principle of magnetic phase-encoded tracking: Two opposing electro-magnetic coils generate alternating magnetic fields with a phase shift. The superimposed field between the coils has a position-dependent phase that is detected with a magnetic sensor. Figure adapted from [193].

The superimposed field is readily estimated by describing the sources as magnetic dipoles[199], generating the magnetic field

$$\vec{B}(\vec{R}) = \frac{\mu_0}{4\pi} \cdot \frac{3\vec{R}(\vec{M} \cdot \vec{R}) - \vec{M}r^2}{r^5} \qquad \text{Eq. 4.1}$$

where $\vec{B}$ is the magnetic field vector at position $\vec{R}$, μ_0 the vacuum permeability $1.26 \cdot 10^{-6}$ Hm^{-1}, r the absolute distance $r = \sqrt{\vec{R}^2}$, and $\vec{M}$ is the dipole magnetization. This first derivation considers only tracking along the axis through the center of a source with the ISAC oriented along this line, thus Equation 4.1 simplifies to

$$B(r) = \frac{\mu_0}{2\pi} \cdot \frac{M}{r^3} \qquad \text{Eq. 4.2}$$

with $B = |\vec{B}|$ and $M = |\vec{M}|$. Magnetic phase-encoded tracking requires two sources facing each other at opposite sides of the working volume at a distance 2·d. The

superimposed field is thus the sum two fields generated by dipoles at positions $\pm\, d$, reading

$$B_{total}(r) = B(d - r) + B(d + r) = \frac{\mu_0}{2\pi}\left(\frac{M_1}{(d-r)^3} + \frac{M_2}{(d+r)^3}\right) \qquad \text{Eq.} \quad 4.3$$

where it is assumed that $r = 0$ is the center of the working volume, and the magnetic moments of the two sources are M_1 and M_2. The sources are supplied with AC currents which generate alternating magnetizations $M_1 = M_{1,0} \cdot \sin(\omega \cdot t)$ and $M_2 = M_{2,0} \cdot \sin(\omega \cdot t + 90°)$, where $M_{1,0}$ and $M_{2,0}$ are the constant amplitudes of the magnetic moments, depending on the properties of the source coils and the driving currents. Inserted into Equation 4.3, it reads

$$B_{total}(r, t) = \frac{\mu_0}{2\pi}\left(\frac{M_{1,0}}{(d-r)^3} \cdot \sin(\omega \cdot t) + \frac{M_{2,0}}{(d+r)^3} \cdot \sin(\omega \cdot t + 90°)\right) \quad \text{Eq.} \quad 4.4$$

Equation 4.4 can be summarized using the harmonic addition theorem

$$a \cdot \sin(x + \alpha) + b \cdot \sin(x + \beta) = \sqrt{a^2 + b^2 + 2ab\cos(\alpha - \beta)} \cdot \sin(x + \delta) \quad \text{Eq.} \quad 4.5a$$

with

$$\delta = atan2(a \cdot \sin(\alpha) + b \cdot \sin(\beta), a \cdot \cos(\alpha) + b \cdot \cos(\beta)) \qquad \text{Eq.} \quad 4.5b$$

The function atan2(y, x) returns the arctan, but distinguishes the sign of the inputs to return the correct angles in all quadrants. Applying the harmonic theorem to Equation 4.4 yields

$$B_{total}(r, t) = \frac{\mu_0}{2\pi}\sqrt{\left(\frac{M_{1,0}}{(d-r)^3}\right)^2 + \left(\frac{M_{2,0}}{(d+r)^3}\right)^2} \cdot \sin(\omega t + \Delta\phi) \qquad \text{Eq.} \quad 4.6$$

with the phase shift

$$\Delta\phi(r) = atan2\left(\frac{M_{1,0}}{(d-r)^3}, \frac{M_{2,0}}{(d+r)^3}\right) = \arctan\left(\frac{M_{1,0}}{M_{2,0}} \cdot \left(\frac{(r+d)}{(r-d)}\right)^3\right) \qquad \text{Eq.} \quad 4.7$$

The final equality can be ensured through the orientation of the sources. As it is evident from Equation 4.6 and Equation 4.7, the superimposed field is a sine with a position-dependent phase shift $\Delta\phi$. Evaluating the phase shift (Figure **4.16**a) shows the unique relationship between the phase of the reference magnetic field and the position along the working axis. It features two plateaus when the superimposed field is dominated by either source in its own periphery, and a steep phase gradient in the center from 0° to 90°. Similar to the preceding discussion, an expression for the phase profile in

3D is derived in the Appendix A2. It should be noted that Equation 4.7 equals the 3D case in Equation A.9 when reduced to the special configuration in 1D. Equation A.9 is evaluated in a 2D plane and displayed in Figure **4.16**b, where two plateau regions with a steep gradient through the center emerges.
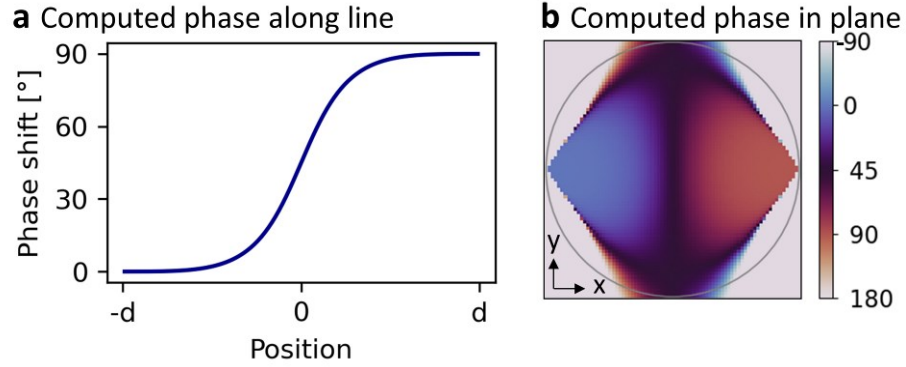

Figure 4.16: Computed position dependent phase shift for magnetic tracking: (a) Along the line connecting the source coils. **(b)** In a 2D plane.

Equation A.9 represents a system of five coupled equations that is suitable to track ISACs with 5 DOF, including parallel displacements and rotation. The detection of the *rotation* of ISACs, however, can be also realized in a simpler way, both experimentally and mathematically. Using the alternative approach, it is sufficient to generate a magnetic field that rotates in one plane. A rotating magnetic field is achieved with four source coils, where opposing coils receive the same input, and the two currents have a 90° phase offset as illustrated in Figure **4.17**a. The resulting field vector consequently reads

$$\vec{B} = \begin{pmatrix} B_X \sin(\omega t + 90°) \\ B_Y \sin(\omega t) \end{pmatrix} = \begin{pmatrix} B_X \cos(\omega t) \\ B_Y \sin(\omega t) \end{pmatrix} \qquad \text{Eq. 4.8}$$

The orientation of an ISAC is equivalent to the sensing direction of the integrated AMR sensor, which coincides with the long catheter axis. The rotation of the ISAC relative to source one is described with a single angle α (Figure **4.17**a), giving the sensitivity direction $\vec{S}$ the form

$$\vec{S} = \begin{pmatrix} \cos(\alpha) \\ \sin(\alpha) \end{pmatrix} \qquad \text{Eq. 4.9}$$

The response of the integrated AMR sensors is linear for small fields. Assuming the sources generate equally strong fields $B_X = B_Y = B$, the expected sensor output V_{Signal} can be described as proportional to the scalar product of the external magnetic field and the device orientation

$$V_{\text{Signal}} = k \cdot \vec{B} \cdot \vec{S}$$

$$= k \cdot B \cdot \begin{pmatrix} \cos(\omega t) \\ \sin(\omega t) \end{pmatrix} \cdot \begin{pmatrix} \cos(\alpha) \\ \sin(\alpha) \end{pmatrix}$$

$$= k \cdot B \cdot (\cos(\omega t) \cdot \cos(\alpha) + \sin(\omega t) \cdot \sin(\alpha))$$

$$= k \cdot B \cdot \cos(\omega t - \alpha) \qquad \text{Eq. 4.10}$$

where the final transformation uses the cosine addition theorem. As it is now clear from Equation 4.10, rotation of an ISAC is directly evident from the phase lag emerging between the supply signal of the respective source and the sensor signal. It should be noted that the derivation of rotation tracking assumes ideally homogeneous magnetic reference fields. The thereby imposed limitations as well as corrective measures are discussed in Section 4.3.6.

a Configuration for angular tracking

$B(t) = B_X + B_Y$

$\vec{S}$ α

$B_X(t) \sim \cos(2\pi f \cdot t)$

$B_Y(t) \sim \sin(2\pi f \cdot t)$

b Generation of rotating reference field

Time

Signals
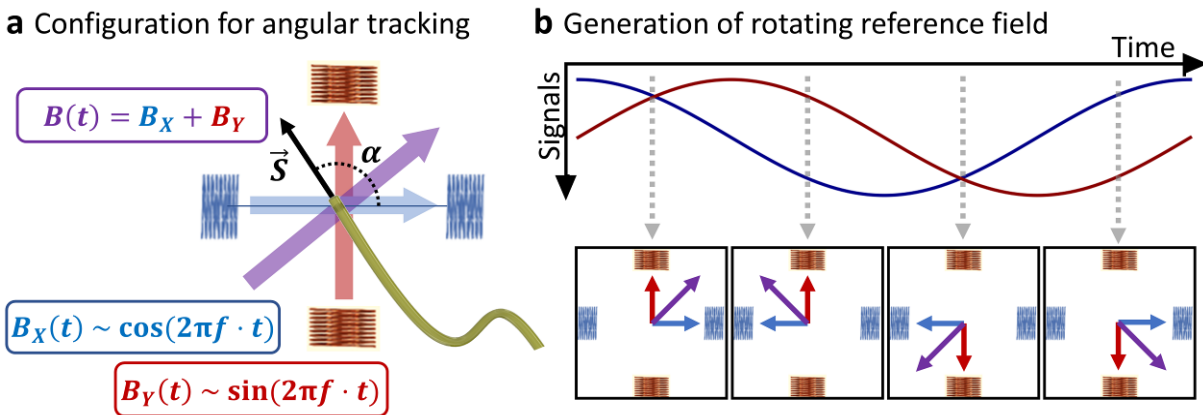
Figure 4.17: Generation of rotating magnetic field using two source pairs: (a) Two source pairs are driven with phase-shifted alternating currents. The generated fields superimpose to form a resulting field. **(b)** Two 90° phase-shifted currents yield a rotating superimposed magnetic field.

4.3.4 EXPERIMENTAL REALIZATION

This section reports the implementation and validation of the tracking schemes for 1d translation and rotation of ISACs as introduced in Section 4.3.3. Electro-magnetic source coils (750 windings, 20 mH) were prepared using 3D printed polymer frames and enamel copper wire. An image of a source coil is displayed in Figure **4.18**a and its impedance curve in Figure **4.18**b. When supplied with an AC current (1 A peak-to-peak, 100 Hz to 1000 Hz), these coils generated magnetic fields that decayed with increasing distance and have safe levels, e.g. of 0.2 mT root mean square (r.m.s.) at a distance of 5 cm, as was measured with a calibrated Hall sensor (Figure **4.18**c).
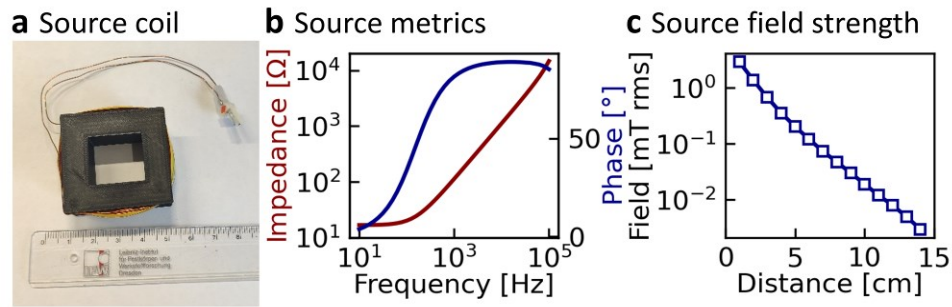
Figure 4.18: Electro-magnetic source coils for navigation: (a) Image of custom-made coils with 750 windings. **(b)** Impedance curve of source coil. **(c)** Strength of magnetic field generated with source coil. Figure adapted from [193].

To assemble the experimental setup, two or four source coils, depending on the application, were mounted on an optical table as shown in the photograph in Figure **4.19**a. A schematic of the experimental setup is displayed in Figure **4.19**b.
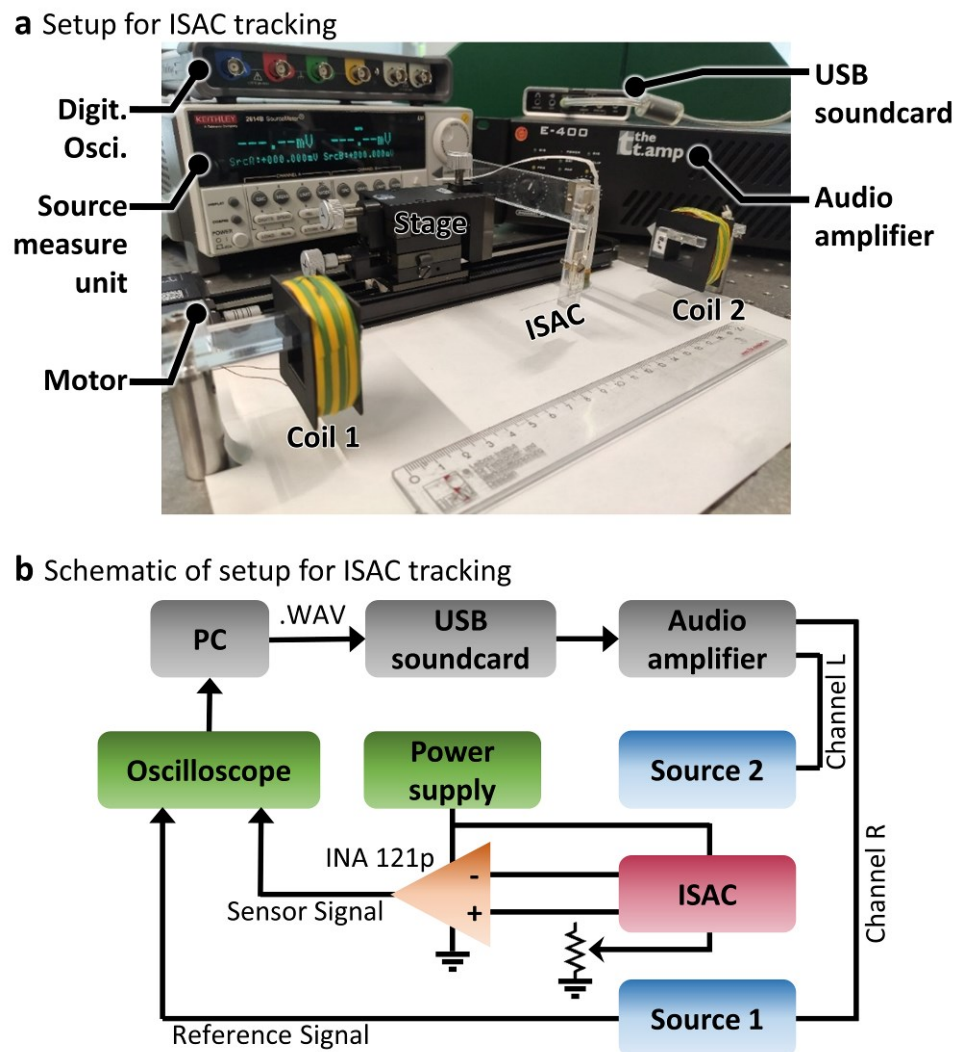
Figure 4.19: Experimental setup for ISAC navigation: (a) Image of setup **(b)** Schematic. Figure adapted from [193].

To produce the supply currents for the source coils, a simple and cost-effective approach was chosen: First, a digital sound file (.WAV, 44.1 kHz sample frequency, 15-bit

resolution) with two channels (left and right) that contained the two sine signals with a phase delay was generated. During tracking experiments, a commercial USB sound card was used to convert the digital file into analog signals. The signals were then amplified with a commercial audio amplifier (t.amp E-400, Thomann, Germany) and supplied to the sources. ISACs were attached to a PMMA sample holder that was mounted on a precise linear motor stage positioned outside the working volume. The signal of the integrated AMR sensor was amplified with an INA 121P instrument amplifier (Texas Instruments, USA) with a gain of 100. A PicoScope 5000 digital oscilloscope (PicoTech, UK) was used to record the amplified sensor signal and the current through one of the source coils (reference signal). Both the sensor and the instrument amplifier were supplied with 2.5 V to 5 V using a SMU (Keithley 2614B, Keithley Instruments, USA) and the current through the AMR sensor was limited to 2 mA with a potentiometer.

To validate the predicted phase-position relationship derived in Section 4.3.3, an ISAC was moved through the working area over a distance of 14 cm with steps of 5 mm. At each step, the sensor and reference signals were recorded. A selection of amplified sensor signals as they were recorded by the oscilloscope, as well as the reference signals that were supplied to the source coils, are displayed in the left column in Figure **4.20**.
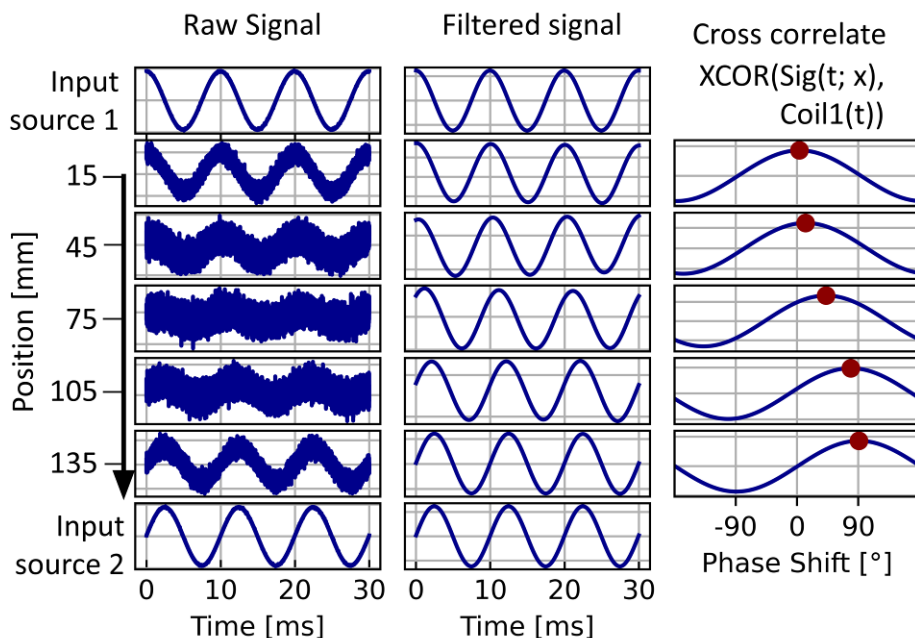
Figure 4.20: Raw and processed sensor data during tracking: (Left column) Supply signals of sources one and two, and signals detected by the integrated magnetic sensor at various locations. **(Center column)** Reference and sensor signals processed with a Butterworth bandpass filter. **(Right column)** Cross-correlation of the position-dependent sensor signal and reference. The shifting peak indicates a position-dependent phase shift. Figure adapted from [193].

By design, the input of source 1 and 2 have a quarter period offset. The depicted sensor signals were recorded at different positions as indicated by the position axis. The signal to noise ratio (SNR) naturally decreases towards the center due to the smaller field strengths. The middle column in Figure **4.20** depicts all signals after they were processed with a Butterworth bandpass filter (Section 3.4.1). The filtered signals show a position-dependent phase offset relative to the input of source one that increases with distance. The exact phase shift can be determined via cross-correlation (Section 3.4.2). The right column in Figure **4.20** displays the cross-correlate of the source 1 input and the sensor signals at different locations. All correlates show a clear maximum (red dots), which transitions from 0° to 90° when the ISAC is moved through the working volumes. Plotting all phase lags that were obtained across the working volume (Figure **4.21**a) reveals the expected unambiguous relationship between position and phase lag. The experimentally obtained phase-distance curve can be fitted with the model as derived in Equation 4.7, as indicated in Figure **4.21**a as well.
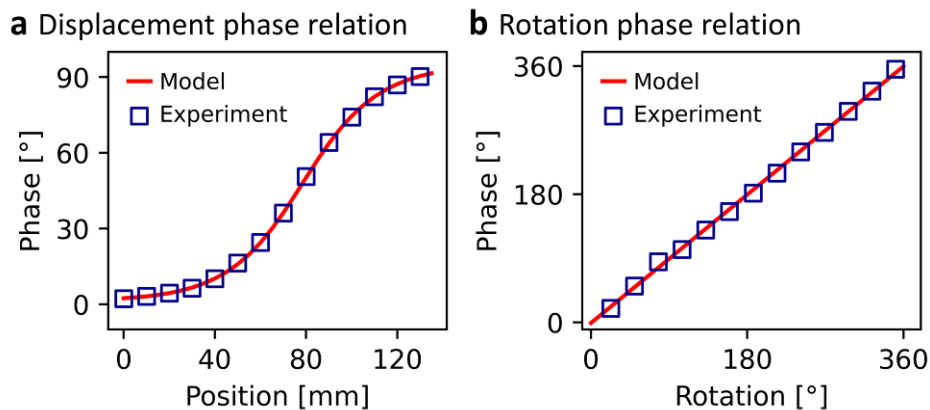
Figure 4.21: Measurement of position and orientation dependent phase shifts: (a) Phase shift during parallel displacement with model fit. Figure adapted from [193]. **(b)** Phase shift during rotation with linear fit.

The fit agrees well with the measured phase lags, confirming the general validity of magnetic phase-encoding for 1d tracking of ISACs. Similarly, the phase-encoding of ISAC rotation angles was verified. Four source coils were arranged and supplied as described in Section 4.3.3 and Figure **4.17** to generate a rotating magnetic field. The orientation of an ISAC was controlled using a micro-stepper motor to exactly adjust its angle in a range of 360°. The measured phase offset is depicted in Figure **4.21**b. As expected based on Equation 4.10, the angle between the ISAC and the reference axis directly translates into a phase offset, leading to a linear relation.

After providing the proof of principle for displacement and angle resolved tracking, its precision requires closer investigation. In the case of displacement tracking, the magnetic phase encodes a location. Consequently, a steep phase gradient is necessary to achieve high spatial resolution. The highest resolution that can be achieved theoretically depends on two parameters: (i) the phase gradient, and (ii) the sampling rate f_{ADC} with which sensor data is obtained, in relation to the frequency of the reference magnetic field f_{Signal}. The sampling rate is limited by the employed measuring electronics, specifically the ADC. Using cross-correlation to determine the phase offset between two signals, the smallest distinguishable offset is

$$\Delta\phi_{\text{min}} = 360° \cdot \frac{f_{\text{Signal}}}{f_{\text{ADC}}} \qquad \text{Eq. 4.11}$$

where the factor of 360° converts the period-fraction-per-sample to a phase angle. Equation 4.11, in simple terms, implies that the smallest measurable phase offset depends on how many measurement points are obtained in each signal period. The lower phase limit $\Delta\phi_{\text{min}}$ is converted into a spatial resolution Δx_{min} via

$$\Delta x_{\text{min}} = \left(\frac{\delta\phi}{\delta x}\right)^{-1} \cdot \Delta\phi_{\text{min}} \qquad \text{Eq. 4.12}$$

where $\delta\phi/\delta x$ is the position-dependent phase gradient. The measured phase depicted in Figure **4.21**a shows a steep gradient in the center, where the phase changes by $\delta\phi = 60°$ over a distance of $\delta x = 50$ mm. Since the measurement was carried out with a reference signal of $f_{\text{Signal}} = 100$ Hz and a sampling rate of $f_{\text{ADC}} = 1$ MHz, the theoretical spatial resolution in this experiment is $\Delta x_{\text{min}} = \frac{50 \text{ mm}}{60°} \cdot 360° \cdot \frac{100 \text{ Hz}}{1 \text{ MHz}} = 30$ µm. It should be noted that this high resolution, at first glance, is not achievable throughout the entire working volume, but only within the center with the steep phase gradient. This critical limitation is addressed with an extension of the herein proposed strategy in Section 4.3.6. The theoretical resolution for angle resolved tracking is found in a similar fashion. Here, a full rotation of $\delta\alpha = 360°$ is encoded by a phase shift of $\delta\phi = 360°$, and hence a ratio $\frac{\delta\alpha}{\delta\Phi} = 1$. With the sampling resolution as above, the lower limit for angular resolution is $\Delta\alpha_{\text{min}} = 1 \cdot 360° \cdot \frac{100 \text{ Hz}}{1 \text{ MHz}} = 0.036°$.

These estimations of achievable resolution assume ideal measurement conditions. Real signals, however, are heavily distorted by noise, which introduces some additional uncertainty. Such adverse effects can be reduced, to some degree, through signal

processing techniques such as cross-correlation. Here, multiple periods of an oscillating signal are considered to average out probabilistic distortions. The precision of the obtained phase lag improves, when the number of included periods increases, leading to a trade of between resolution and temporal performance. To estimate the resolution that can be achieved under realistic conditions, a magnetic reference field was measured 200 times with a static ISAC, and the phase lag was estimated using 200 to 1000 signal periods. The measured time lags have a spread due to measurement inaccuracies, as depicted in the series of histograms in Figure **4.22**a. One time lag unit corresponds to a minimal displacement $\Delta x_{\mathrm{min}} = 30$ µm or minimal rotation $\Delta\alpha_{\mathrm{min}} = 0.036°$ as derived above. The standard deviation (SD) of the datasets in Figure **4.22**a were used to define an uncertainty and converted to an estimated error using the Δx_{min} and $\Delta\alpha_{\mathrm{min}}$. The resulting resolutions are summarized in Figure **4.22**b.
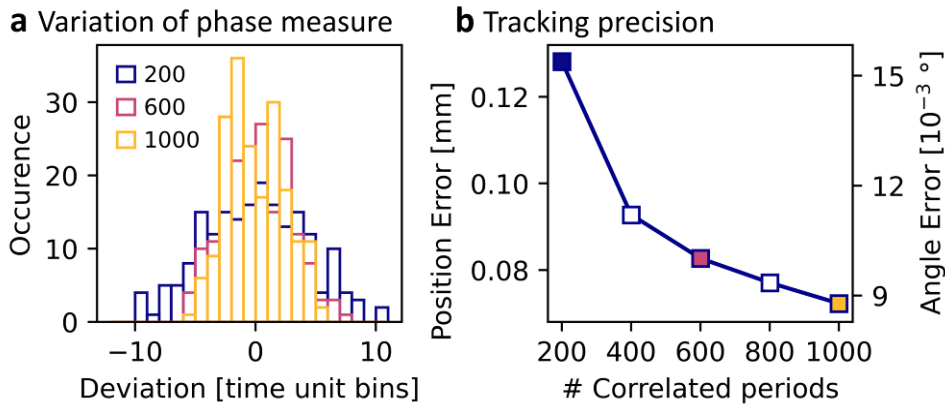
Figure 4.22: Resolution of magnetic tracking: (a) Histogram showing spread of phase measurements at same position. **(b)** Experimentally achieved resolution depending on acquired signal length. Figure adapted from [193].

When only 200 signal periods are used, the standard error is about four times the theoretical optimum, yielding 0.13 mm and 0.16° for displacement and rotation, respectively. The precision improves when 400 and 600 periods are included. The return on increasing signal length diminished above 600 periods and saturates towards 1000 periods, where a resolution of 72 µm and 0.086° is achieved.

As demonstrated both with computational estimations and experimental measurements, magnetic phase-encoded tracking can enable very high resolution both for parallel displacement and rotation. A comparison with established tracking technologies and a discussion on future perspectives is provided in Section 4.3.6.

4.3.5 SIMULTANEOUS MAGNETIC AND ULTRASOUND TRACKING

The previous estimation of ISAC tracking performance was carried out under idealized conditions. This section assesses the new navigation approach in a more realistic model environment.

Magnetic phase-encoding can provide precise location data but needs to be supplemented with anatomic information to offer meaningful navigation. In future applications, such additional information should be provided by medical imaging techniques, including magnetic resonance imaging or computed tomography, in the form of anatomic maps. Here, the compatibility of ISAC tracking and US imaging is investigated. US is a widely applied technique to image soft anatomies, e.g. in the abdomen or throat region. Since US is reflected by mechanically dense tissue, this approach is not ideal to investigate body parts that are surrounded by bones, such as the brain. To further assess ISAC tracking, a model environment consisting of an agar block (40 x 35 x 20 mm^3) with a hollow channel (ø 0.7 mm) was prepared as described in Section 3.3.4 and placed in a water tank. The phantom setup was then arranged between a pair of source coils and the channel was aligned with the tracking axis (Figure **4.23**a).
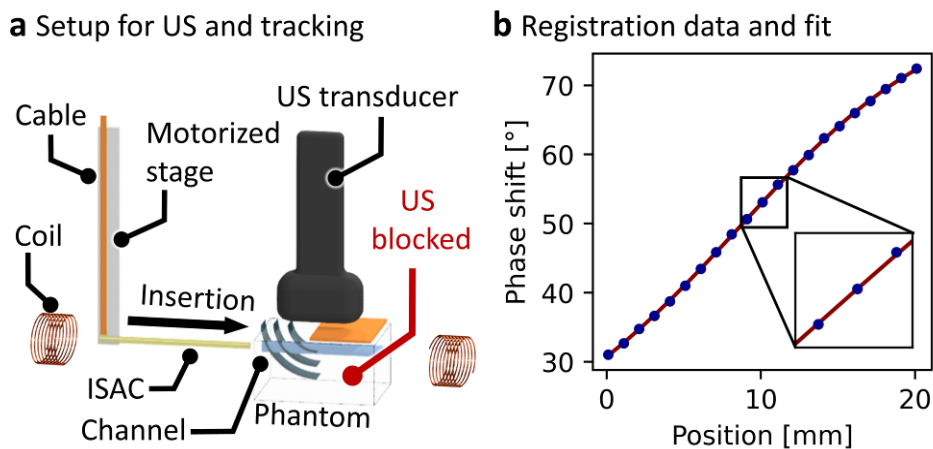
Figure 4.23: Setup for simultaneous magnetic and US tracking: **(a)** Illustration of setup. **(b)** Calibration curve with model fit linking positions to unique phase shifts. Figure adapted from [193].

A commercial US imaging system (FUJIFILM VisualSonics, Kanada) was positioned above the phantom to monitor the channel. US imaging was performed by Azaam Aziz (Leibniz IFW Dresden). The transducer was equipped with a 256-element transducer array and operated with 21 MHz central frequency. An ISAC was again mounted on a holder that was controlled by a precise linear motor stage.

As it is commonplace in EMT, a registration step is required at first. The integrated sensor is scanned through the working volume to prepare a calibration function linking

measured signals to positions. The ISAC is inserted stepwise into the water-filled phantom channel to record the phase with a step size of 1 mm, five times at each position. The measured phase shifts, as well as a fit with the model (Equation 4.7), is displayed in Figure **4.23**b. To perform simultaneous magnetic and US tracking, an ISAC is inserted stepwise into the phantom. The device is well visible under US and appears as a dark line in the image series in Figure **4.24**a. The frame-to-frame progression as observed by US agrees well with the real displacements, as defined by the motorized stage and indicated with red arrows. Additionally, the position of the ISAC tip is determined via magnetic tracking and the previously prepared calibration curve. It is depicted with threefold blue boxes, indicating one, two, and three SDs around the estimated position. The measurement was performed using a frequency of 100 Hz and 300 signal periods. The estimated and real positions show excellent agreement within one SD in four, and two SDs in one case.
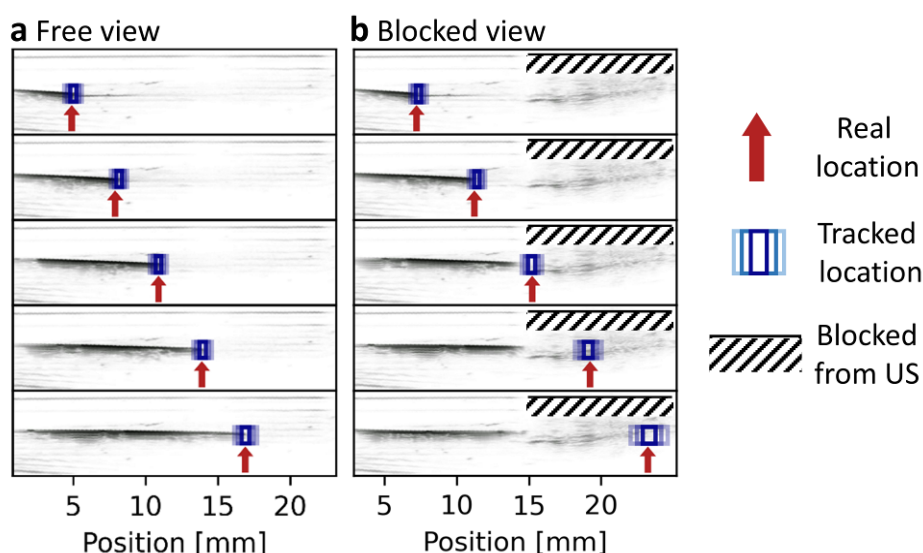
Figure 4.24: Simultaneous magnetic and US tracking: (a) US images of an ISAC being inserted into an agar phantom channel. **(b)** The right half of the observed area is obstructed from US imaging by a dense object. US imaging was performed by Azaam Aziz (Leibniz IFW Dresden). Figure adapted from [193].

To emulate a scenario in which US imaging is obstructed by a dense object (e.g. skull bones), copper foil was placed over half the phantom. The dense barrier blocks US waves from reaching the underlying region. Consequently, the resulting US images display a noisy and blank area. The insertion and tracking experiment was then repeated as shown in Figure **4.24**b. The ISAC is well visible in the left half of the observed area, but not detectable by US in the right half below the copper foil. In contrast, magnetic tracking continues to reliably predict the tip position of the ISAC within one SD in all five measured locations. It should be noted that the increase of position uncertainty with greater

insertion depths in Figure **4.24**b originates from the flattening phase gradient towards the edge of the working area, which naturally reduces the tracking resolution.

This study proves that ISACs can be operated and tracked in combination with US and hints at the complementary character of this setup: While US can provide 'anatomic' information, e.g. the location of the channel and the dense object, magnetic tracking reliably predicts the device position even when the complementing technique is obstructed.

4.3.6 DISCUSSION, LIMITATIONS, AND PERSPECTIVES

The performance of ISAC tracking by means of magnetic phase-encoding was introduced, proven conceptually, characterized, and demonstrated in a model environment. Table **4.2** compares the proposed navigation approach to previously available technologies from the commercial and research sectors. Parameters chosen for comparison are the resolution, the working volume, and the size of the employed sensors[48,200]. Available navigations systems operate in working volumes with typical sizes of 300 mm to 500 mm where they offer tracking accuracies usually between 0.5 mm and 1.5 mm, and > 0.2° of orientation tracking resolution. Higher tracking accuracies can be achieved at the cost of smaller working volumes. In contrast, ISACs offer very high tracking resolutions, undercutting the leading commercial system by a factor of seven regarding position tracking.

Table 4.2: Comparison of electro-magnetic tracking systems

Model	Working volume [mm x mm x mm]	Position accuracy [mm r.m.s.]	Orientation accuracy [degree r.m.s.]	Sensor length and diameter [mm x mm]
Aurora 5DOF[#]	500 x 500 x 500	0.70	0.20°	ø0.45 x 8.20[$]
Aurora 6DOF[#]	500 x 500 x 500	0.48	0.30°	ø0.92 x 9.40
3D Guidance[#]	310 x 460 x 300	1.40	0.50°	ø0.56 x 12.0
Anser EMT[‡]	250 x 250 x 250	1.14	0.09°	ø0.50 x 8.0
This work	**ø200[%]**	**0.07[&]**	**0.09°**	**ø0.12 x 0.4**

[#]Northern Digital Incorporated[54,200] ‡Anser EMT is an open-source EMT platform[48]. $Most precise sensor according to the manufacturer. Alternatives are available with diameters ≥ 0.3 mm or lengths ≥ 5.5 mm. %Diameter of spherical working volume. &Achieved in high phase-gradient area.

The significant downside of ISAC tracking is the small working volume, which is defined as the size of a hypothetical sphere that fits between the source coils, which are 200 mm

apart. A remarkable advantage of ISACs is the much smaller size of the sensor (ø 0.12 mm x 0.36 mm), which is thinner than the thinnest EMT probe on the market (Aurora 5DOF, ø 0.30 mm), and much shorter than any alternative[54]. Since conventional thin EMT probes rely on electro-magnetic induction and pick-up coils[48], the probes need to accommodate a certain amount of wire windings and cannot be miniaturized beyond this constrain. Here, ISACs with integrated AMR sensor can offer an attractive alternative to develop highly flexible probes for the navigation of surgical tools. This unique combination of small sensor size and high tracking resolution of ISACs is ideally positioned to complement available EMT technologies in modular systems, specifically regarding interventions within the brain: Conventional probes might be used to navigate a host catheter from the insertion site in the groin, through the abdomen and thorax into the brain, where an ISAC is deployed to navigate the tortuous sub-millimeter vessels, synergistically combining the advantages of multiple technologies. To realize this vision, however, a number of challenges remain to be addressed.

The temporal performance of ISAC tracking is one of them. The comparison in Table **4.2** excludes parameters such as refresh rates or latency. In this regard, commercial solutions are highly optimized to offer frequent updates, often with tens of frames every second, and vanishing time lags. Using ISACs, in contrast, it currently takes multiple seconds to first record sufficient signal periods and then to compute the cross-correlation. The second step can be reduced to an instant through dedicated hardware, e.g. applications specific integrated circuits (ASICs). To reduce the first and major component, i.e. the signal acquisition time, while maintaining the resolution, reference fields with higher frequencies in combination with faster readout electronics can be used. The signal frequency must be chosen carefully, considering the available signal sources, potential cross-talk with readout electronics, and bio-compatibility and safety aspects[201].

The effective working volume and resolution for the tracking of ISACs is another important aspect. A high tracking resolution is only achievable in regions with a steep phase gradient, which applies to only a quarter of the working area, as seen in Figure **4.21**a. This can be addressed through real-time modifications to the reference magnetic field. According to Equation 4.7, the position of the steep gradient depends on the ratio between $M_{1,0}$ and $M_{2,0}$, which represent the magnetic field strengths emitted by the two sources. The gradient appears in the center when both coils are supplied equally, but shifts towards the weaker signal source when one of the supply currents is changed

(Figure **4.25**a). The option to shift the high-resolution area for tracking deterministically was validated experimentally. An ISAC was used to map out the position dependent phase landscapes that were generated with varying source supply ratios $M = M_{2,0}/M_{1,0}$. As displayed in Figure **4.25**b, the gradient region shifts in accordance with the predictions, allowing to adjust the phase landscape such that most of the area can be covered with a step gradient.
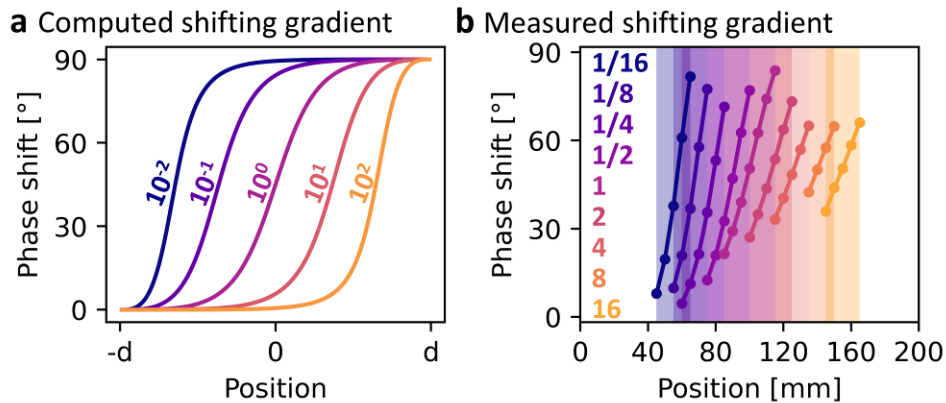

Figure 4.25: Adaptation of magnetic reference field: (a) Controlled shift of phase gradient according to model computations. **(b)** Experimental demonstration of the shifted phase gradient. The numbers indicate the relative current strengths of the source coils during each measurement.

Another limitation affects the assessment of orientation. The strategy provided by Equation 4.10 assumes a homogeneous magnetic field, with equally strong field components in both planar directions. This cannot be realized easily with only two coils. The strict relation between the device orientation and the measured phase is only guaranteed in the center of the working volume. As displayed in Figure **4.26**, the linear relation deteriorates when the measurement is repeated at off-center locations.
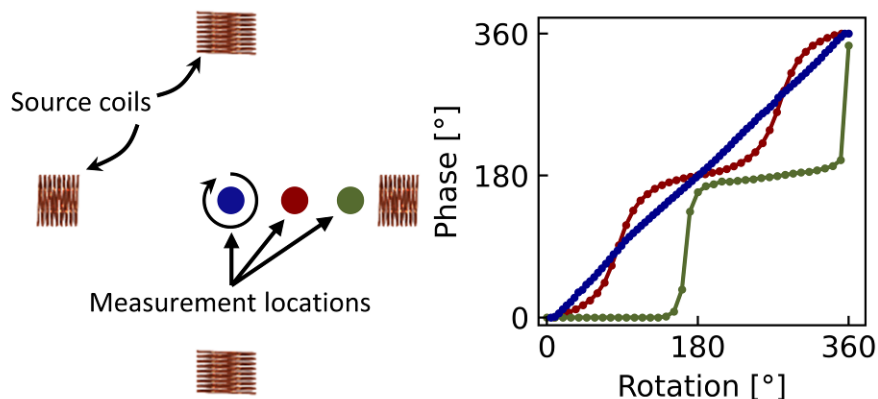
Figure 4.26: Orientation tracking in an inhomogeneous reference field: Orientation tracking was performed at different locations indicated in the schematic. Off-center positions with unequal field strength contributions yield distorted angular encoding.

Therefore, upcoming iterations of the tracking setup will need to include more source coils to generate homogeneous reference fields. The same applies regarding the extension

of ISAC tracking into multiple spatial dimensions, and the parallel tracking of position and orientation. Multiple source pairs in a 3D arrangement around the working volume will be required to provide enough information for position and orientation reconstruction with 5 DOF.

5 RESHAPEABLE MICRO-ELECTRONIC DEVICES

Flexible electronics are attractive for bio-medical tools that interface and interact with biological tissues on various length scales[20,63,85,86]. However, it remains challenging to precisely adapt the shape of flexible implants to irregular target anatomies, such as microscopic nerve bundles, for interfacing and manipulation. This chapter is dedicated to the development and evaluation of **r**eshapeable **m**icro-**e**lectronic **d**evices (RMEDs). As illustrated in Figure **5.1**a, RMEDs are based on a microscale PI carrier platform (500 x 360 μm^2) that is equipped with PPy actuators. These biocompatible 'artificial muscles' (Section 3.1.4) can reshape the device and control its curvature. Moreover, RMEDs integrate sensors that are used to monitor their shape or orientation. An external controller implements a feedback loop, which monitors the electrical signals from the sensors to compute an actuator bias accordingly.
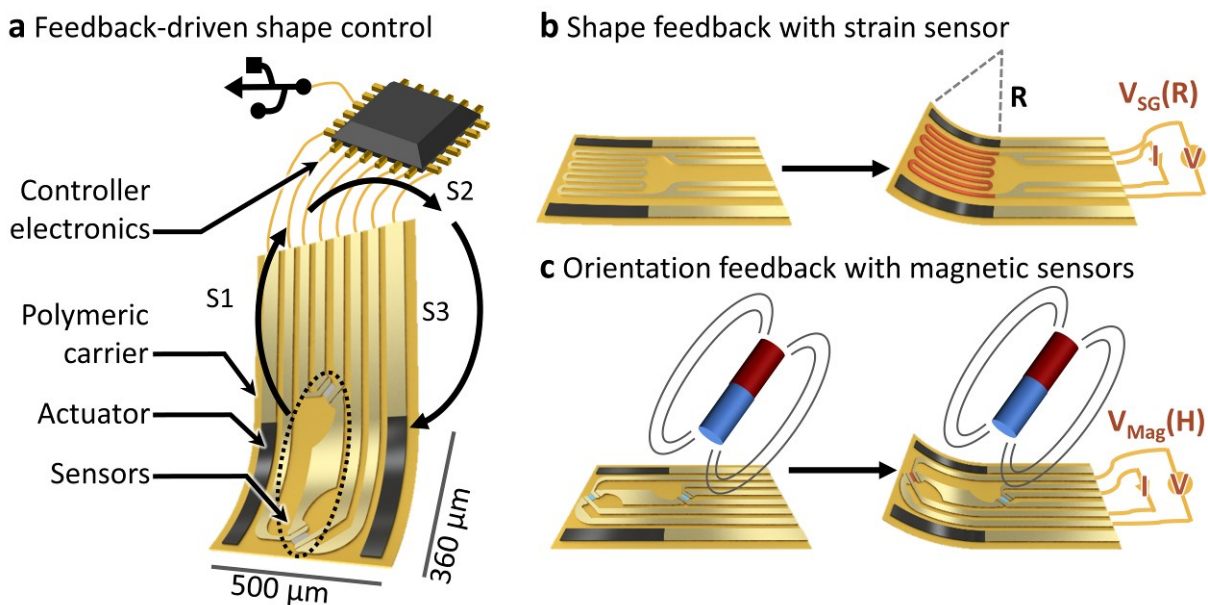
Figure 5.1: Concept of reshapeable micro-electronic devices: (a) A polymeric carrier platform supports sensors and actuators. The sensor signal is evaluated by external electronics to compute and apply an appropriate actuator bias. **(b)** Integrated strain sensors measure the curvature of RMEDs directly. **(c)** Magnetic sensors probe external reference fields to assess device orientation. Figure adapted from [202].

The integration of actuators, sensors, and a feedback control loop allows RMEDs to perceive their environment and interact with it, e.g. by mechanically detecting an object that hinders actuation. In this thesis, two complementary sensor technologies are integrated into RMEDs, namely gold stripe strain gauges (GSSG)[174] that assess the device curvature directly (Figure **5.1**b), and SVMS[125] (Section 2.3.1) that detect their orientation relative to an external magnetic field (Figure **5.1**c).

In this chapter, the design considerations, fabrication, and the electronics and software required to operate RMEDs are reported in Section 5.1, and the performance of actuators is investigated in Section 5.2. Magnetic feedback control of device orientation is introduced in Section 5.3. Section 5.4 then reports the application of GSSG for curvature control and object detection. Parts of the results presented in this chapter have been published in the journal Advanced Intelligent Systems (B. Rivkin, C. Becker, F. Akbar, R. Ravishankar, D. D. Karnaushenko, R. Naumann, A, Mirhajivarzaneh, M. Medina Sánchez, D. Karnaushenko, and O. G. Schmidt, 'Shape-Controlled Flexible Microelectronics Facilitated by Integrated Sensors and Conductive Polymer Actuators', *Adv. Intell. Syst.* 3, 6, 2000238, 2021) and reproduced under the conditions of the creative commons license (CC-BY 4.0).

5.1 DESIGN AND FABRICATION

RMEDs constitute a novel type of integrated system, in which PPy actuators can reshape a flexible device while covering only 20 % of its area. To achieve a greater range of reshapeability and higher curvatures, the device architecture and manufacturing parameters require careful consideration. The remaining free area of the PI carrier platform is then available to accommodate additional electronic components.

5.1.1 ESTIMATION OF OPTIMAL FABRICATION PARAMETERS

To enable an efficient transformation of electro-chemically induced strain to mechanical reshaping, the thicknesses in a curving multi-layer system need to be defined with care. During actuation, PPy expels hydrated ions to transform a stack of PI/Au/PPy from a flat geometry to its curled-up state with a curvature radius $R = \kappa^{-1}$ (Figure **5.2**a). The highest achievable curvature in these systems is determined by the thicknesses and mechanical properties of the components and can be expressed using the curvature coefficient c_κ as introduced in Section 2.2.1. Expected values for c_κ can be computed using Equation 2.6[118]. While the Young's moduli of Au, Al_2O_3, and PI are readily available from previous reports[86,118,203], mechanical properties of PPy can vary widely depending on the exact fabrication conditions. In this thesis, the stiffness of PPy used in this work was determined to be about 0.5 GPa using atomic force microscopy (AFM) microindentation, which agrees with commonly reported values[118,204]. AFM measurements were carried out by Rachappa Ravishankar and supervised by Dr. Volker Neu (both Leibniz IFW Dresden). Equation 2.6 was further modified to account for the different areas of PI, Al_2O_3,

and Au by multiplying their moduli with factors of 5, 3, and 3, respectively. Considering layer thickness ranges of 0.2 μm to 1.2 μm for PI, and 0.1 μm to 5 μm for PPy, Equation 2.6 was evaluated as summarized with the color-coded map in Figure **5.2**b. For each layer thickness of the PI carrier, there is an optimal PPy thickness that maximizes the curvature coefficient, as indicated with a white line. Thinner and thicker actuator layers both lead to smaller achievable curvatures. Optimal actuation is achieved with a ratio of PI and PPy that corresponds to $h_{PPy} = 3.6 \cdot h_{PI} + 0.2$ μm. These estimations and observations agree with previously reported studies[117]. It should be further noted that the achievable curvature generally decreases with increasing layer thicknesses, implying that PPy actuators are most efficiently used in micro-scale, thin-film systems. Based on this computation, RMEDs were fabricated with a PI carrier thickness of 0.5 μm, which proved as decent compromise between robustness and flexibility. The optimization of the PPy actuators then consequently was oriented around 2 μm layer thickness.
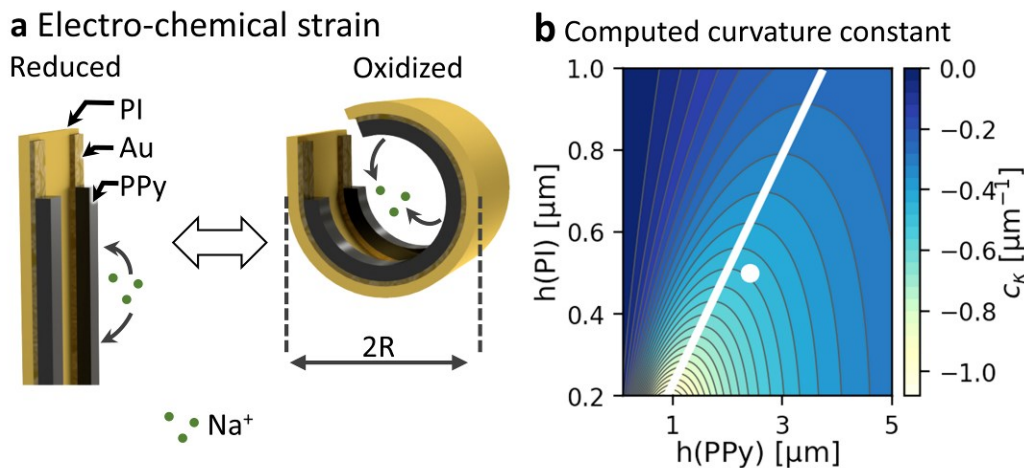
Figure 5.2: Definition and estimation of RMED curvature: (a) RMEDs reshape to form structures with curvature radius *R*. **(b)** Computed curvature coefficients for RMEDs with different combinations of PI and PPy layer thicknesses. The white line indicates which PPy thickness maximizes curvature for each PI thickness, the white dot indicates the parameters used for RMEDs in this work. Figure adapted from [202].

5.1.2 DEVICE FABRICATION

RMEDs were fabricated using recently developed polymeric materials (Section 3.1) and standard processing techniques (Section 3.2). To begin, glass substrates (50 x 50 mm²) were cleaned and coated with an adhesion layer. The subsequent micro-processing steps are illustrated in Figure **5.3**. Rectangular patches of SL were patterned from the precursor solution via spin-coating and photolithography. Then, the rectangular PI carried platform was processed such that it was anchored to the glass substrate from one side. To fabricate RMEDs with SVMS, GMR multi-layer stacks (Section 2.3.1) were processed with sputter

deposition ($2.4 \cdot 10^{-6}$ mbar base pressure, $1.4 \cdot 10^{-3}$ mbar Ar atmosphere, 100 W power) and patterned via lift-off, yielding elliptical structures (85 μm long axis, 55 μm short axis). Then, $Ti^{4\,nm}/Au^{30\,nm}$ electrodes that served as contacts for SVMS or as GSSG, as well as made up the electrodes for PPy deposition, were processed via e-beam evaporation and lift-off. Each RMED integrates two electronic components that are supposed to operate inside an electrolyte solution without cross-talk or other interference, making efficient chemical and electrical insulation indispensable. To reliably insulate integrated sensors from the environment, a layer of Al_2O_3 (20 nm) was processed to cover sensors and simultaneously mask the Au actuator electrodes to later achieve the desired coverage with PPy. The insulating layer was deposited via ALD (Section 3.2.4) and etched chemically (2.7 % TMAH, 10 min) through a PR mask.
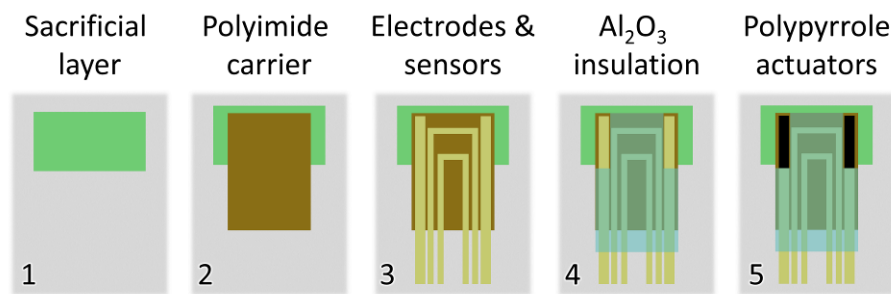
Figure 5.3: Fabrication of RMEDs. Figure adapted from [202].

To finalize RMEDs, glass substrates that each carried 22 devices (Figure **5.4**a) were diced and individual devices were connected with flexible cable connectors and ACF via hot press bonding. RMEDs carry two exposed Au electrodes (350 x 50 $μm^2$) along their edges. Using the electronic connections established in the previous step, these electrodes were connected as working electrodes in a three-electrode electro-chemical setup to deposit thin layers of PPy as introduced in Section 3.2.5. Deposition was performed with constant voltage of 500 mV and layer thicknesses were controlled through deposition time, e.g. 2.4 μm within 35 s. After PPy deposition (Figure **5.4**b), devices were rinsed with DI water and placed in an etching solution (2 % HCl_{aq}) to selectively remove the SL and release the free-standing part of the PI carrier (350 x 500 $μm^2$) completely within 20 min (Figure **5.4**c). Formerly, it has been challenging to release bending PPy micro-actuator compounds from their handling substrates. Common techniques involved the exploitation of poor adhesion (e.g. Au on Si) that is notoriously unreliable, or metallic sacrificial layers that require strong and corrosive etchants that can damage other components[185]. In contrast, the procedure in this thesis involves a metal-organic SL (Section 3.1.1) and only mild acids for its removal, allowing gentle processing conditions with a high yield and no

apparent damage to the actuators. After release, RMEDs can be reshaped by applying small bias voltages (-1 V to 0.5 V vs Ag/AgCl) to the actuators and change their shape from a flat state (Figure **5.4**c) to various curvatures (Figure **5.4**d).
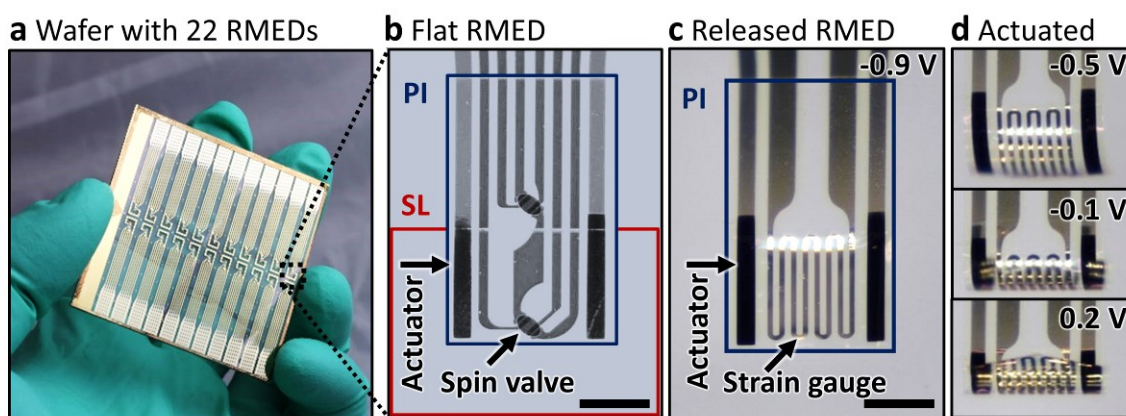
Figure 5.4: Realized RMEDs: (a) Image of glass wafer (50 x 50 mm²). **(b)** Micrograph of RMED with SVMS prior to release. Scale bar indicates 200 μm. RMEDs with SVMS were fabricated in collaboration with Christian Becker (Leibniz IFW Dresden). **(c)** RMED with GSSG after release in its flat state. Scale bar indicates 200 μm. **(d)** An RMED curls up when the actuator bias is adjusted. Figure adapted from [202].

5.1.3 CONTROL ELECTRONICS AND SOFTWARE

The operation of RMEDs requires the simultaneous readout and processing of sensor data, the interpretation of user input, and the computation and application of actuator bias voltages. The accomplishment of this task requires dedicated hardware and software. In this thesis, RMEDs were operated using a custom developed PCB (Figure **5.5**a, PCB designed and fabricated by Dr. Daniil Karnaushenko, Leibniz IFW Dresden) equipped with a microcontroller (Silicon Labs, USA) that drives an 8-channel differential 32-bit ADC, and an 8-channel 16-bit DAC, operating at 1 kHz. The microcontroller PCB was complemented with a graphical user interface (GUI) that was implemented in Python and PyQt5, allowing real time control of applied bias voltages and sensor readout (Figure **5.5**b). The GUI allowed to adjust DAC outputs controlling PPy actuators manually and observe and record sensor data. In addition, it implemented routines, e.g. to perform CV (Section 3.3.3) and PID control (Section 3.4.3). Additional adapters were prepared to connect RMEDs to the microcontroller PCB, which used active and passive electronic components. Sensors were operated using a low dropout constant current supply, providing 0.5 mA to 1 mA to drive magnetic and strain sensors in four-point resistance measurements (Section 2.3.2). Sensor voltages were filtered to reduce noise with a resistor-capacitor low-pass filter element (R = 1 kΩ, C = 1 μF) prior to recording. The bias voltage generated by DACs was

kept below 1.2 V with a safety diode, since even short unintended voltage bursts can permanently damage PPy actuators.
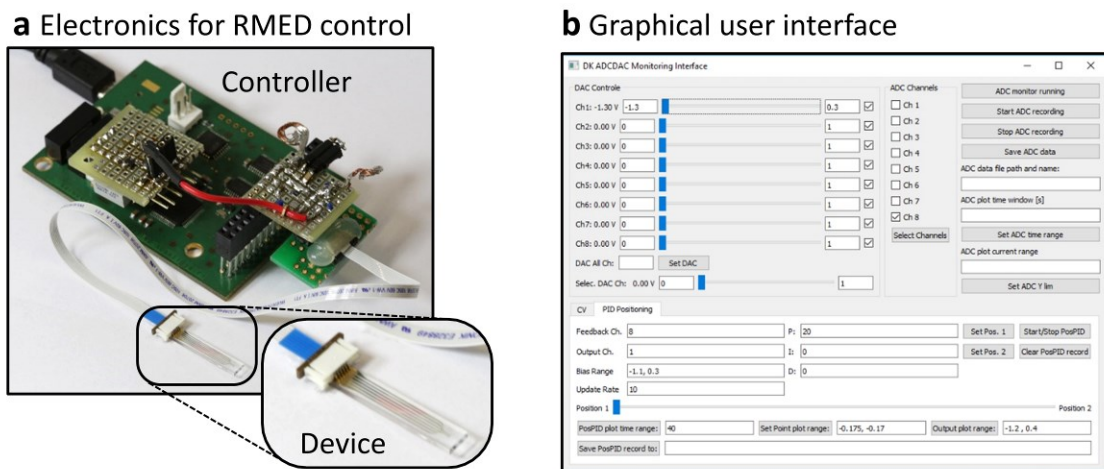
Figure 5.5: Hardware and software for the operation of RMEDs: (a) A custom-developed microcontroller PCB with eight sensing and eight voltage supply channels connects to an RMED via a flex-cable. PCB designed and fabricated by Dr. Daniil Karnaushenko (Leibniz IFW Dresden). **(b)** Custom developed software with a GUI controls the PCB in (a) to record signals, apply voltages, and execute procedures and algorithms. Figure adapted from [202].

5.2 PERFORMANCE OF ACTUATORS

PPy actuators allow to reshape RMEDs reversibly, gradually, and instantaneously. The small area requirement of the actuators makes RMEDs unique among actuated soft micro-systems. The actuation performance is assessed in this section.

5.2.1 BLOCKING FORCE, SPEED, AND DURABILITY

The *blocking force* of an actuator is a key metric, which describes the smallest counterforce that an actuator cannot overcome. Although high blocking forces are usually regarded desirable, the capability to excerpt excessive force or pressure can be a safety risk when manipulating sensitive tissue. The blocking force of RMEDs was estimated using a series of sample weights that were balanced on a semi-curled RMED (Figure **5.6**a). The RMED was able to support weights up to 0.33 mg, which corresponds to a gravitational force of 3.2 mN when corrected for buoyancy, and even lift it by 50 µm. The specific blocking force thus is 8.3 N cm^{-2} when normalized to the area of actuators, landing in the same ballpark as related reports[205], and is sufficient for the envisioned applications, e.g. as nerve clamp or nerve cuff. Importantly, these applications as actuated surgical tools require timely actuation with little delay. A camera operating at 30 frames per second was used to estimate the actuation speed of RMEDs. These recordings revealed that a full reshaping, i.e. full curling or flattening, can happen in as little as 1 s

(Figure **5.6**b). An RMED with an alternative layout, featuring three actuators and two sensors, was used for this study.
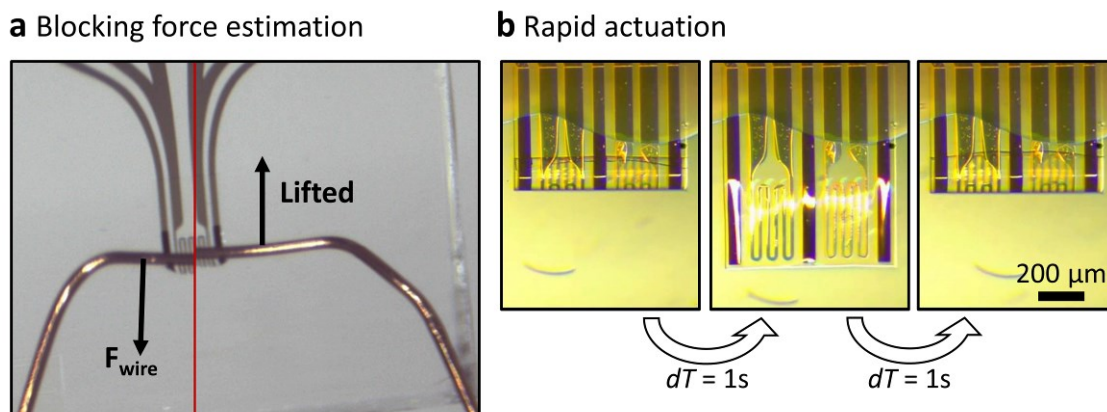
Figure 5.6: Force and speed of RMED actuators: (a) An RMED holds a sample weight against the gravitational force of 3.2 mN and lifts it by 50 µm. The device width is 500 µm. **(b)** An RMED transforms from fully curled to flat, and reverse, within less than 1 s for each transformation. Figure adapted from [202].

Besides force and speed, durability is an important property for tools that are envisioned for robot-assisted surgery. An RMED was operated continuously for 5 h, during which the bias voltage was cycled with a frequency of 0.05 Hz, or a total of 900 actuation cycles. The scan rate of 100 mV s^{-1} was chosen as it is commonly used for CP actuator characterization throughout available literature. As depicted in Figure **5.7**a, no catastrophic degradation of the electrical performance can be observed. The slight decrease of actuator currents can be likely attributed to minor delamination of PPy from its electrodes[152], or chemical changes within the polymer network[177] (Section 3.3.3). Besides, no critical failure, such as complete PPy delamination that is not uncommon in similar material systems, was observed.
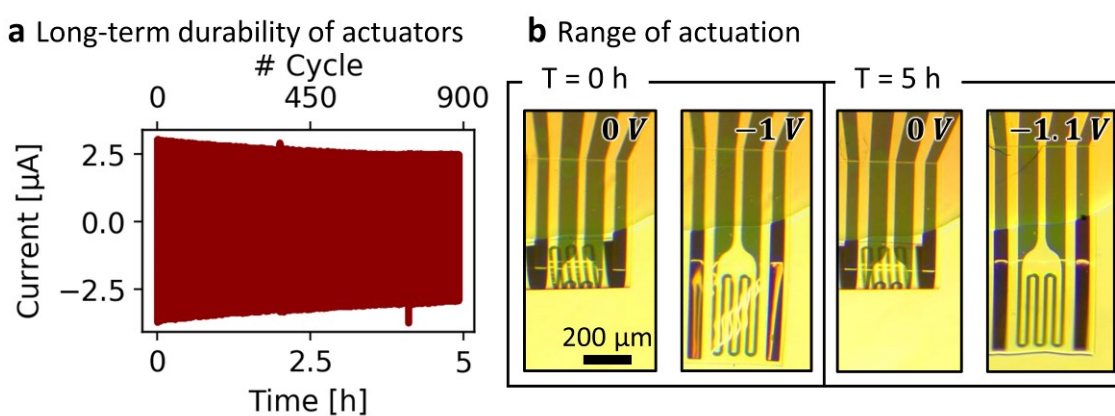
Figure 5.7: Durability of RMEDs: (a) Current consumption of an RMED that was continuously operated for 5 hours, performing 900 actuation cycles. **(b)** The range of actuation of RMEDs is preserved throughout 5 hours of continuous operation. Figure adapted from [202].

The observed stability of RMED actuators is possibly enabled by the ultra-thin layers and the resulting small strain (≈ 0.15 %) at the Au/PPy interface. The range of actuation is mostly preserved even after 900 actuation cycles as shown in the micrographs in Figure **5.7**bAlthough actuator durability is evidently not a limiting factor for RMEDs, electrode surface modifications could be adopted from published reports to further increase their lifespan, including the intentional roughening of Au electrodes to promote adhesion[152].

5.2.2 CURVATURE

To assess the range of actuation of RMEDs, actuator biases in the range between -0.8 V and 0.2 V were applied with increments of 0.1 V to stepwise reshape an RMED. The actuation was monitored electrically (Figure **5.8**a) and observed from the side with a microscope to measure curvature radii. After each change in bias voltage, a small current of about 2 µA to 12 µA is drawn to reshape the device at an instant. The transition from a fully flat to fully curled state required only 1.6 µJ of electrical energy.
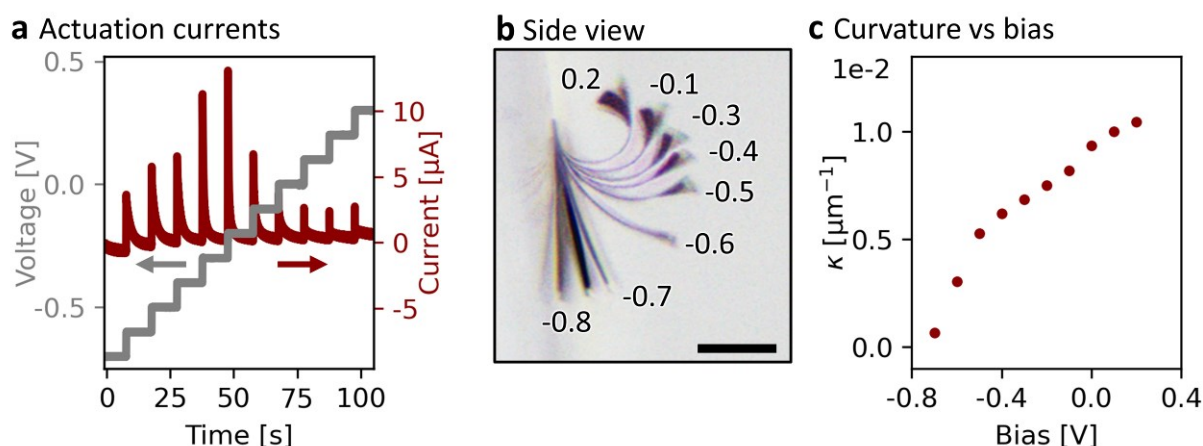
Figure 5.8: Curvature control of RMEDs: (a) Current consumption of RMEDs during stepwise change of bias voltage. **(b)** Overlay of micrographs showing one RMED with different curvatures and actuator biases displayed in volts. Scale bar indicates 200 µm. **(c)** Voltage-dependence of the curvature of one RMED derived from micrographs in (b). Figure adapted from [202].

Figure **5.8**b displays an overlay of micrographs taken during these individual actuation steps. The view from the side allows to measure the curvature at each step, as summarized in Figure **5.8**c. The RMED is completely flat at -0.8 V. Small changes of the bias voltage increase the curvature substantially, especially around the oxidation peak of PPy around -0.5 V. The rate of curvature change diminishes afterwards and the highest curvature of $\kappa = (90\ \mu m)^{-1} \approx 0.01\ \mu m^{-1}$ is achieved around 0.2 V. These curvatures are similar to those that have been achieved with PPy actuated compounds and thick support

layers, but smaller than those with only thin platforms[117].The efficient shape transformation displayed in Figure **5.8**b was achieved with optimized device that had PPy layer thicknesses between 2 µm and 2.4 µm, very similar to what was expected based from the computation in Section 5.1.1. Other devices that were fabricated during device optimization with PPy thicknesses of 1.2, 1.7, 3.0, and 3.7 µm yielded far smaller curvatures, achieving only one quarter circles. In contrast, optimized RMEDs can reshape to three-quarter circles, which is the required shape for the firm grasping of microscopic objects, such as nerve bundles.

5.3   ORIENTATION CONTROL WITH MAGNETIC SENSORS

It should be noted that an explicit relationship between actuation bias and device curvature, as provided in Figure **5.8**c, is only valid for individual devices and short time periods. Factors including fabrication conditions, operational conditions, actuator hysteresis, and degradation can decisively impact the actuation performance of CP-based actuators. To achieve reliable and reproducible shape control, integrated sensors are required to provide real-time feedback about the curvature state. Among various potential sensor technologies, magnetic sensors are particularly attractive. These micro-electronic components can sense their orientation in space relying solely on weak and bio-compatible magnetic fields. When integrated in actuated surgical tools, this functionality can be useful, e.g. in robotic end effector stabilization to compensate for hand tremble and other human error. This section, for the first time, reports the feedback control of CP actuators using integrated magnetic sensors, namely spin vales. RMEDs with SVMS discussed in this chapter were conceptualized, fabricated, and characterized in collaboration with Christian Becker (Leibniz IFW Dresden), who has optimized and reported these sensors previously[125].

5.3.1 MAGNETIC SENSORS ON ACTUATED DEVICE

Figure **5.9** illustrates how orientation feedback for RMEDs can be obtained using integrated magnetic sensors. RMEDs are equipped with two SVMS that exploit the GMR effect, one anchored to the substrate as reference (sensor 1), the other on the free-standing, actuated carrier (sensor 2). An external magnetic field has a certain projection onto the planes of sensors 1 and 2, and the sensor signal depends on the angle between the projections field vector and the sensor's reference layer orientation

(Section 2.3.1). When an RMED is actuated, the changing projection of sensor 2, compared to sensor 1, changes the sensor signal and can be used as deflection feedback.
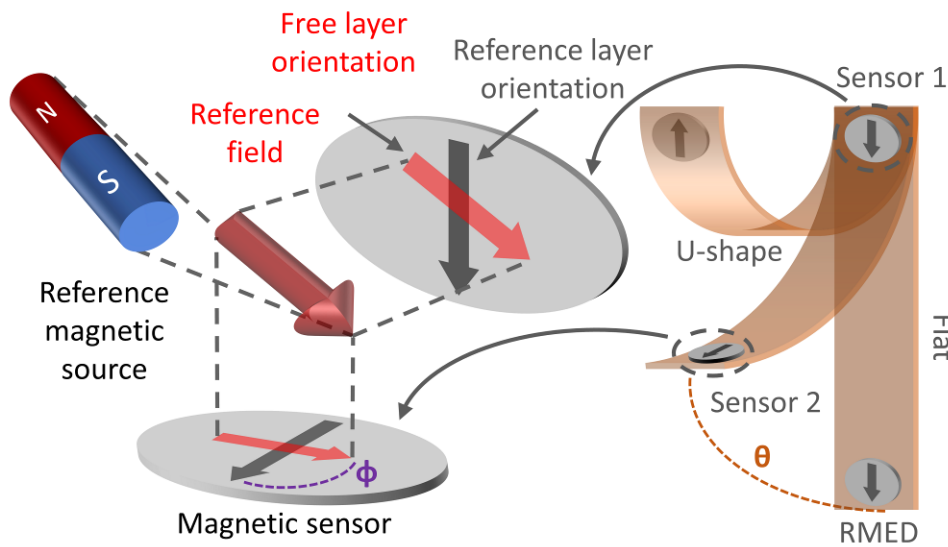
Figure 5.9: Illustration of magnetic orientation tracking: Spin valve magnetic sensors assess an external reference magnetic field. When the RMED is actuated to an angle θ, the free layer orientation aligns with the external magnetic field. The resulting angle between ϕ between the free and reference layers is measured electrically and converted into an actuation angle. A second sensor is stationary and serves as reference. Figure adapted from [202].

To characterize RMEDs with integrated SVMS, a permanent magnet was attached to a rotating stepper motor and placed such that the field was parallel to the flat device. The resulting magnetic field rotated in the plane of the RMED (≈ 10 mT, 90 rpm). This constellation yields synchronous sinusoidal responses from both sensors (Figure **5.10**a) and thus shows that both components perceive the external field identically in the flat device state. The field strength was sufficient to saturate the sensors and use them in their operational regime (5 to 60 mT). The response, i.e. the sensor resistance, is lowest when the external field and the reference layer are parallel (p.), and highest when antiparallel (a.p.), as indicated in Figure **5.10**a, in agreement with the basic working principles of spin valves (Section 2.3.1). The SVMS can be characterized by analyzing their response in the rotating field. Upon rotation, the resistances change form 16.02 Ω and 16.86 Ω to 16.62 Ω and 17.53 Ω for sensors 1 and 2, respectively. The peak-to-peak difference translates to a dynamic range of about 5 % and an SNR of about 100, which is comparable to previous reports[125]. With the same rotating magnetic field applied, the RMED was actuated to form a U-shape as depicted in Figure **5.9**. In this experiment, both sensors are processed such that their reference direction is oriented at 45° to the axis of actuation to prevent ambiguities in the rotating magnetic field. In this configuration, sensor 2 is inverted upon actuation and faces the reference sensor with a tilt of approximately 90°. The responses

of sensors 1 and 2 consequently show a phase offset of about 90°, corresponding to the geometric tilt (Figure **5.10**b). Besides the expected phase offset, sensor 2 still shows the characteristic sinusoidal response, thereby demonstrating that CP actuators and magnetic sensors can be operated in one integrated system.
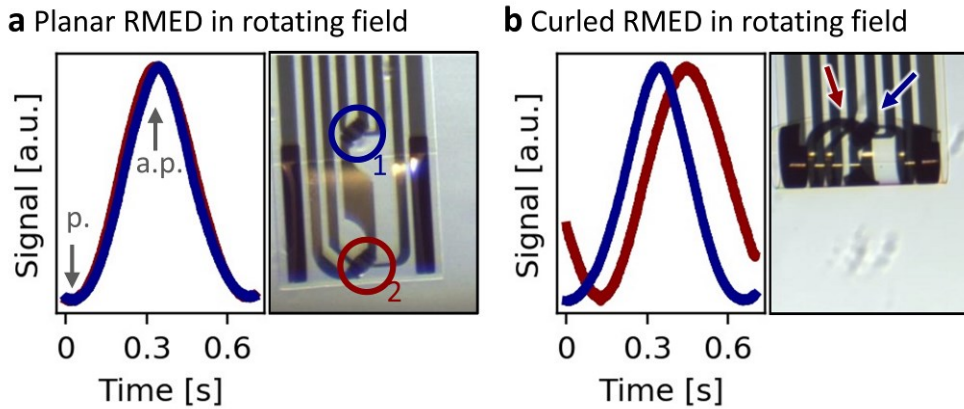
Figure 5.10: Simultaneous operation of SVMS and PPy actuators: (a) Both integrated SVMSs perceive a rotating magnetic field identically when the RMED is flat. **(b)** When curved to a U-shape, the SVMSs face each other with an approximately 90° tilt of reference layer magnetizations and a corresponding phase shift emerges in the sensor signals. The device width is 500 µm. RMEDs with SVMS were fabricated in collaboration with Christian Becker (Leibniz IFW Dresden). Figure adapted from [202].

5.3.2 REFERENCE MAGNETIC FIELD

If arranged in a suitable way, a static magnetic field is sufficient to enable orientation feedback with SVMS. These sensors will yield a unique response for any relevant actuation angle if two conditions are met: (i) the sensor-plane projection should be sufficiently strong (5 - 100 mT) to keep the SVMS saturated for all actuation angles, and (ii) the angle between the projection field vector and the reference layer should be unique for each actuation angle. To identify a suitable configuration, the projection angle Φ and the projection field strength $B_{Projected}$ were estimated for actuation angles $0 < \theta < 180°$ using geometric computations. This study considers an RMED that is actuated through a field with one out of three alternative orientations as depicted in Figure **5.11**a: $\vec{B}_X$ oriented along the actuation axis (x-axis), $\vec{B}_Z$ oriented orthogonal to the actuation axis (z-axis), and $\vec{B}_{XZ}$ that is tilted between the x and z-axis at 45°. In this study, the sensor was processed such that the reference layer magnetization was orthogonal to the actuation axis, i.e. aligned with the z-axis, to maximize the dynamic range. The first computation considers $\vec{B}_X$ as reference. In this case, the sensor reference and the field are always at 90° for any actuation angle and both ϕ and $B_{Projected}$ are constant (Figure **5.11**b and c), thus violating both criteria. The second computation assumes $\vec{B}_Z$ as magnetic reference field. As

displayed in Figure **5.11**b, the angle ϕ is constant $\phi = 0°$ for $\theta < 90°$ and jumps at an instant to $\phi = 180°$ at $\Theta = 90°$. The projection field strength (Figure **5.11**c) drops to zero when the external fields and the sensor are orthogonal at $\theta = 90°$, again violating both criteria. In contrast, $\vec{B}_{XZ}$ is a suitable reference field. Here, ϕ gradually and monotonically shifts from 45° to 135° upon actuation, and the projection is at least 70 % of the full reference field, sufficient to keep SVMSs saturated in physiologically safe external fields of e.g. 10 mT (Figure **5.11**b and c). With both criteria met, this configuration offers an unambiguous map between the sensor response and the RMED actuation angle $0 < \theta < 180°$, which can be used for magnetic orientation feedback.
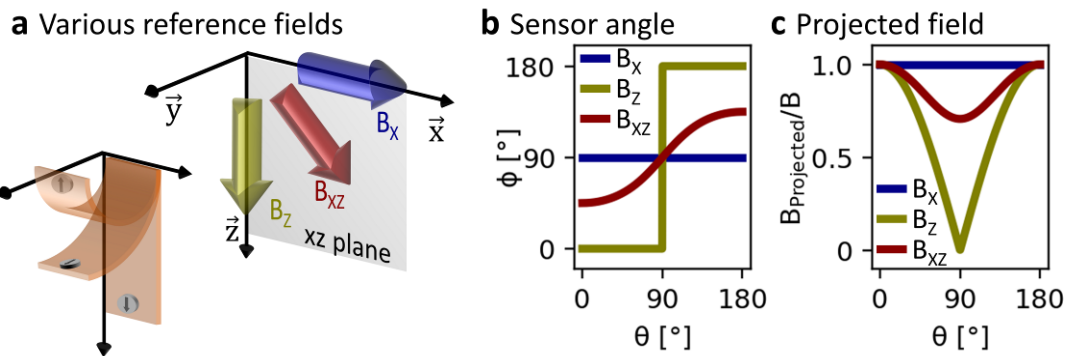
Figure 5.11: Effects of different reference field orientations: (a) Reference field orientations along the x-axis (B_X), z-axis (B_Z), or tilted by 45° (B_{XZ}). **(b)** Estimated sensor angles of the free layer for different actuation angles. **(c)** Estimated normalized strengths of in-plane projected reference fields. Figure adapted from [202].

5.3.3 FEEDBACK CONTROL

To exploit the response of SVMSs for orientation control, a PID feedback loop (Section 3.4.3) was implemented using custom-developed hardware and software as described in Section 5.1.3. The sensor signal was used as feedback and the output of the control algorithm was supplied as actuation bias to the RMED. The setpoint was manipulated to actuate the RMED from a flat to curved state. This trial used the simplest variant of a PID controller where the integral and derivative components are set to zero. Figure **5.12** shows the SP, FB, and OP curves of a two positioning attempts. Using a small proportional gain parameter $K_P = 15$, the controller recognizes the SP change at $t = 0$ and adjusts the OP slowly with a rate of 0.14 V s^{-1}. The FB remains almost unchanged throughout the first 5 s, then approaches the new SP within 3 s and overshoots by about 25 %. During the next 20 s, the FB slowly creeps towards the setpoint. This slow performance is easily improved by increasing the constant gain parameter. With $K_P = 50$, the controller adjusts the output rapidly with up to 2.4 V s^{-1} after a SP change, leading to

a swift actuation. The FB crosses the SP after only 0.65 s, more than 10-fold faster than previously. After an overshoot of approximately 35 %, the FB equilibrates at the new SP after a total of about 1.6 s.
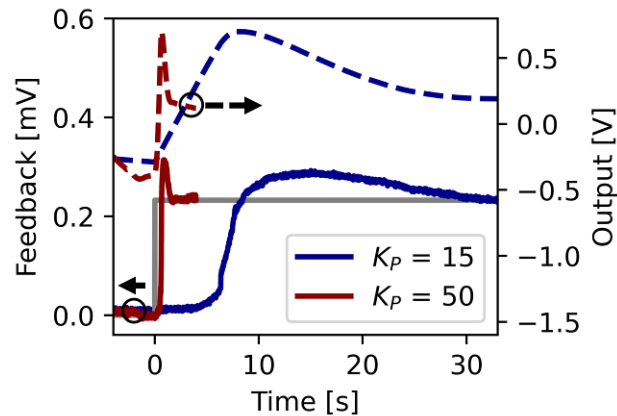
Figure 5.12: Feedback driven orientation control of RMEDs: The solid lines indicate the sensor signal (feedback) while the dashed lines represent the actuator bias voltage (output). Figure adapted from [202].

This experiment demonstrates for the first time the feedback control of CP actuators in an integrated micro-system using a simple PID control scheme. The performance, namely the equilibration time and overshoot, should be further improved with dedicated control algorithms that can be selected based on the specific requirements of future applications. A combined approach using feedback and physics driven models[155] could adequately consider the non-linearity of PPy actuators and facilitate rapid and precise control.

5.4   SHAPE CONTROL WITH INTEGRATED STRAIN SENSORS

Future micro-robotic surgical tools and adaptive implants need to actively monitor their shape during interventions to ensure reliable and reproducible actuation and prevent accidental tissue damage. One standard approach to assess the curvature of flexible devices rely on GSSGs as introduced in Section 2.3.2.

5.4.1 STRAIN GAUGE CURVATURE SENSORS

RMEDs integrate GSSGs for the direct assessment of their curvature. Here, a GSSG is formed by a Au trace with a width of 15 µm and a total length of 1.2 mm. Its resistance is measured in a pseudo four-terminal setup and 1 mA probing current, revealing a total resistance of about 270 Ω when the RMED is flat. When the device is actuated, the GSSG experiences compressive strain and its resistance decreases. Figure **5.13**a depicts the relative resistance change of up to $\Delta R/R \approx 0.37$ % for all curvature states that were observed in the previously discussed measurement of RMED curvature (Section 5.2.2).

Since the surface strain of RMEDs can be estimated to be about 0.15%, the resistance change agrees with an expected GF of 2 for thin-film metals. The SNR for this measurement is about 12 and could be improved with high GF materials, e.g. Si[175], if a higher resolution is deemed necessary. This sensor additionally has a temperature dependence of 0.45 Ω K^{-1} and thus requires a temperature reference if stable operation conditions cannot be ensured.
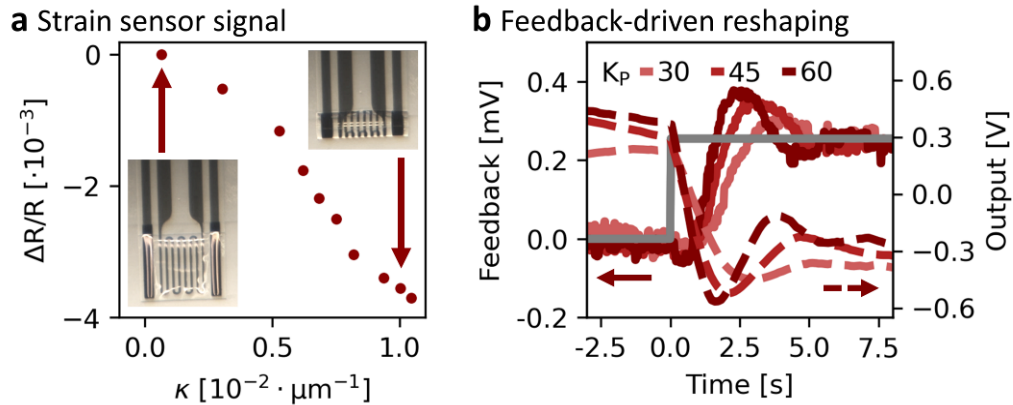
Figure 5.13: Shape feedback and control with integrated strain sensors: (a) Curvature-dependent signal of an integrated strain sensor. **(b)** PID feedback-driven shape control with different gain parameters. Figure adapted from [202].

5.4.2 FEEDBACK CONTROL

These integrated GSSG enable a direct and unambiguous estimation of the real curvature of RMEDs and are readily used for feedback driven shape control, similar to the previous demonstration with magnetic sensors. PID control loops with constant gain parameters K_P of 30, 45, and 60 were implemented to adjust the RMED curvature after a user input changed the SP at $t = 0$. Figure **5.13**b displays the corresponding feedback and output curves. The control loop adjusts the output at an instant and the FB reaches the SP for all settings within 2 s to 3 s, where higher gains yielded slightly faster actuation. All FB curves feature a slight overshoot and an equilibration after less than 6 s. The configuration with $K_P = 60$ led to slight oscillations after the SP was reached, as they are typical for overly aggressive controller settings. Again, more elaborate and dedicated control algorithms can be implemented to further improve the rise and settling times.

5.4.3 OBSTACLE DETECTION

Feedback-driven shape control can be especially beneficial in dynamic operation environments, e.g. where an unforeseen obstacle might obstruct actuation as displayed in Figure **5.14**a. This scenario was studied in three variations, including the reference case

of free actuation as well as with either a hard or soft obstacle that was placed in front of an RMED. Figure **5.14**b displays the strain sensor signal during actuation in these three cases, where the bias voltage was swept from -0.3 V to 0.4 V to reshape the device from its flat to curved state. With no obstacle, the sensor signal changes gradually and monotonously as in the previous cases of free actuation. In the following analysis, this sensor signal obtained during free actuation serves as reference curve. It should be noted, however, that such a reference has a limited life span since the relation between actuator bias and curvature is preserved only temporarily as discussed in Section 5.3. Prolonged operation thus might require calibrating the system multiple times.
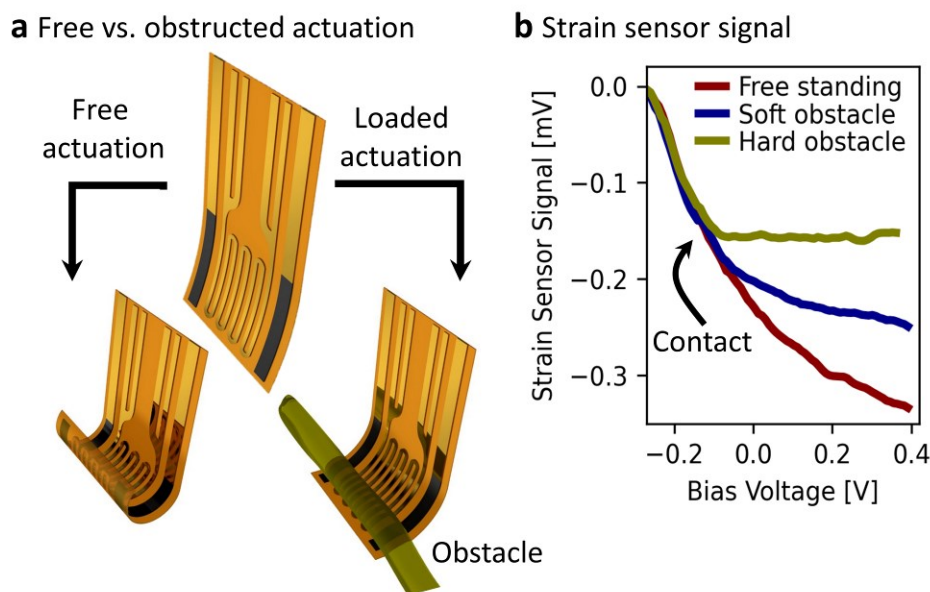
Figure 5.14: Obstructed actuation: (a) The path of actuation can be either free or obstructed by an obstacle. **(b)** The response of an integrated strain sensor during free and obstructed actuation. Obstacles inhibit the reshaping, which is indicated by the sensor signal. Figure adapted from [202].

To study obstructed actuation, a microtiter pipette was positioned in front of the same RMED to serve as a hard obstacle. When sweeping the actuator bias, the sensor signal coincides with the reference curve until the RMED touches the obstacle and remains constant afterwards, indicating that the obstacle prevents further shape changes. The sensor signal features a sharp kink where the RMED touches the obstacle. A soft obstacle leads to a third type of response. In this iteration, a sciatic nerve fiber that was derived from a mouse model (Section 3.3.4) is used to mimic the application case of neuronal surgery. With such a soft obstacle in front of the RMED, the sensor signal initially follows the reference, but then gradually diverges from the free actuation reference curve, indicating a smaller actuation amplitude compared to the free case. This behavior is related to the low stiffness of the nerve bundle, as it does not completely block actuation

immediately after contact, but is compressed by the RMED to some degree. During a surgical intervention, an RMED should automatically detect an obstacle, even one as soft as a nerve bundle, to adjust its actuation and prevent damage from the sensitive tissue. This feature would enable smart surgical tools that assist surgeons and might prevent human error when treating tissues that cannot withstand high pressures.

An automated object detection is implemented as additional condition into a PID control loop. Prior to obstructed actuation, the RMED was fully reshaped without mechanical load to obtain a reference curve, allowing to generate a calibration that related each bias voltage to a strain sensor signal ('Free standing' case in Figure **5.14**a). Then, an obstacle was placed in the path of actuation of the same RMED and feedback driven shape control was carried out as in Section 5.4.2. To detect an obstacle, the adjusted algorithm compared the measured strain sensor signal with the 'free actuation' reference for each actuation bias level. This comparison was made in each iteration step of the control loop. When a deviation of 20 % between reference and measured signal occurred, the controlling software flagged an obstacle detection. At this instant, the actuation was halted by permanently fixing the OP at the present level, which effectively kept the RMED in a constant shape. First, obstacle detection was performed using the hard obstacle, i.e. the microtiter pipette, which was placed in front of a flat RMED. Figure **5.15**a displays the SP, FB, and OP curves of two positioning attempts. At first, obstacle detection was deactivated and the SP was changed to reshape the RMED into its curved state. As expected, the FB cannot reach the SP and consequently, the OP is increased until it reaches a predefined safety limit of 0.4 V. Figure **5.15**b-1 shows a micrograph of this situation. The pipette prevents the RMED from reshaping despite the actuator bias change, leading to an undesired off-axis deformation. Automated object detection was activated for the second run. Now, the algorithm detects the unexpected sensor response and swiftly halts the actuation by fixing the OP at about −0.2 V. The corresponding FB curve indicates a smaller curvature while the corresponding micrograph (Figure **5.15**b-2) shows a mostly flat RMED. Such swiftly halted actuation attempts might prevent damage from RMEDs when encountering hard obstacles.

a Actuation with hard obstacle

b Constrained actuation
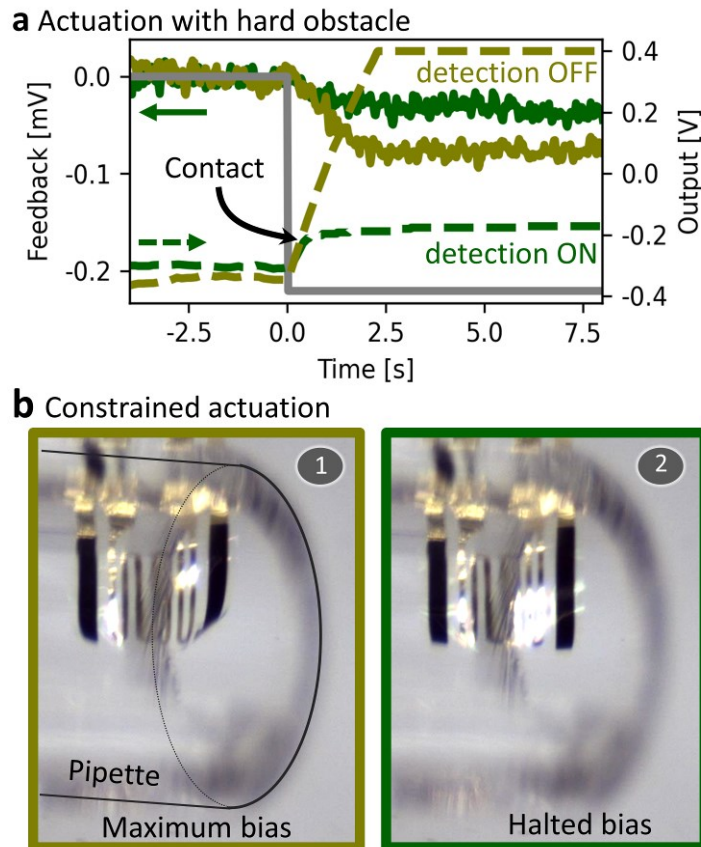
Figure 5.15: Feedback controlled actuation with hard obstacle: (a) Feedback-controlled actuation obstructed with a hard object with and without obstacle detection. **(b)** Micrograph of a microtiter pipette obstructing the actuation of an RMED. The controller applies the maximum actuator bias (1) or halts the actuation once the obstacle is detected (2). The device width is 500 μm. Figure adapted from [202].

In a second experiment, the nerve bundle was placed in front of the RMED. Figure **5.16**a displays a positioning attempt without obstacle detection. The strain sensor signal, i.e. FB, indicates a considerable deformation of the RMED despite the soft obstacle. Since the SP again cannot be reached, the controller applied the maximum actuator bias and actuators proceeded to compress the soft tissue with maximal pressure, thus potentially endangering the nerve to suffer mechanical damage. The micrograph in Figure **5.16**b-1 shows the grasped nerve being forcefully compressed. This is prevented when the automated obstacle detection is activated for a second run. The controller recognizes the obstacle in less than a second after the SP is adjusted and fixes the OP at the current level (Figure **5.16**a). The FB changes just slightly from the initial level and the micrograph (Figure **5.16**b-2) confirms that the RMED adjusted its shape to gently hold the tissue without compressing it. In a potential application of RMEDs as nerve clamps, these instruments should similarly detect soft tissues and hold them in place with as little force as possible.

a Actuation with soft obstacle

b Grasping of nerve fiber bundle
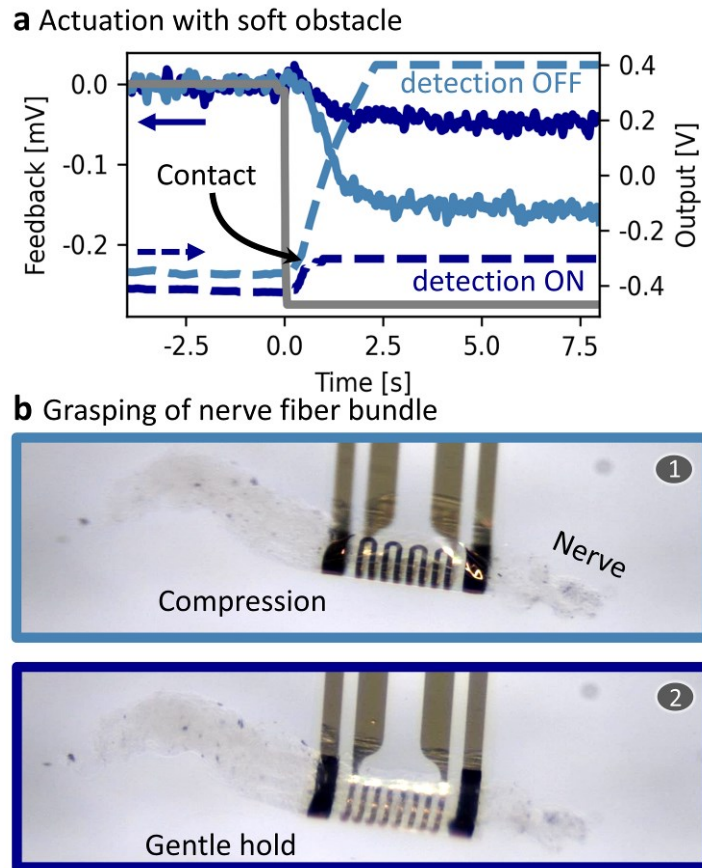
Figure 5.16: Feedback controlled actuation with soft obstacle: (a) Feedback-controlled grasping of a nerve bundle with and without obstacle detection. **(b)** Micrographs of an RMED compressing the grasped nerve fiber with maximal force (1) or holding it gently after the object was automatically detected (2). The device width is 500 µm. Figure adapted from [202].

5.5 HETEROGENOUS INTEGRATION WITH ACTIVE ELECTRONICS

A key challenge in the development of electronic micro-systems with high integration density is the accommodation of electronic components as well as their metallic interconnects. In addition, an increasing number of components that rely on external hardware, e.g. for signal detection or the supply of power, require equally more complex control electronics to enable parallel operation. Both the developments of ISACs and RMEDs would be impeded if future systems would require individual connections and hardware channels for each embedded component, limiting the number of components that each device can carry. A superior approach takes advantage of integrated circuits that enable on-board multiplexing, i.e. the targeted opening and closing of connections to address individual components. Such functionalities are offered by active-matrix (AM) circuits[206,207], for instance those using thin-film transistors (TFTs)[208,209]. AMs are used in a variety of devices to manage high numbers of electronic components with a significantly smaller number of external hardware channels and interconnects, most prominently in displays such as AM liquid-crystal displays (LCDs)[210] and active-matrix

organic light emitting diodes (AMOLEDs)[211], where thousands of individual opto-electronic devices, the pixels, need to be operated in parallel. The combination of TFT-AMs and electro-chemical devices to carry out dissimilar site-selective electro-chemical processes, however, has not been previously explored. In this thesis, digital electro-chemistry is developed to deposit and control up to 64 integrated PPy actuators in a TFT-AM circuit. The AM relies on amorphous indium gallium zinc oxide (a-IGZO) TFTs[212,213] that allow to address individual actuators from a set of devices that are arranged in a chess-board pattern as shown in Figure **5.17**a. The TFT-AM is connected to a microcontroller PCB as in Section 5.1.3 and immersed in a water bath together with a counter electrode that is connected to the electrical ground (Figure **5.17**b).
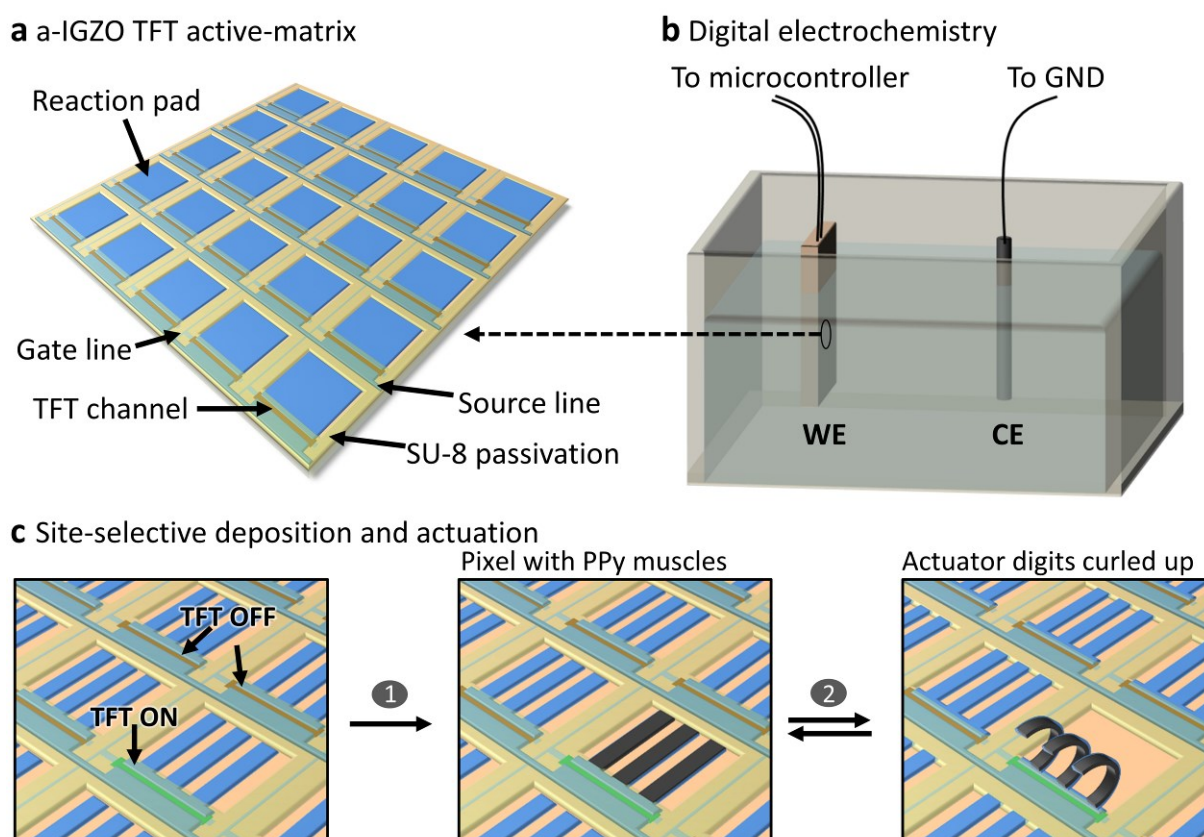
Figure 5.17: Concept of digital electro-chemistry: (a) An TFT-AM comprises source lines and gate lines. TFTs are located at their intersections. **(b)** Setup for digital electro-chemistry **(c)** A pixel is exposed to the source voltage of the corresponding line when its TFT is opened through a bias of the corresponding gate line. The source bias can control CP deposition (1) or actuation (2). Figure adapted from [214].

The operation of active electronic devices inside an electrolyte solution required dedicated insulation measures to ensure operational and long-term stability[215]. Each pixel within the AM is located at the intersection of a source line and a gate line and implements a TFT, acting as a switch that can be opened or closed. To supply a specific actuator with the desired bias voltage, the associated gate line is used to open the

corresponding TFT, exposing the actuator to the voltage applied through the corresponding source line. Using this approach, PPy can be deposited and actuated in a site-selective manner (Figure **5.17**c). Individual actuators as well as entire subsets of the matrix can be controlled in parallel.

The results presented in this section have been achieved in collaboration with Dr. Bin Bao (Leibniz IFW Dresden), who fabricated, characterized, and optimized a-IGZO TFT-AMs, and have been published in the journal Advanced Materials (B. Bao, B. Rivkin, F. Akbar, D. D. Karnaushenko, V. Bandari, L. Teuerle, C. Becker, S. Baunack, D. Karnaushenko, O. G. Schmidt, 'Digital Electrochemistry for On-Chip Heterogeneous Material Integration', *Adv. Mater.* 33, 26, 2101272, 2021). The reproduction of published results in this thesis is permitted under the conditions of the creative commons license (CC BY 4.0).

5.5.1 Fabrication and properties of active matrices

Multiple TFT-AMs with eight source lines, eight gate lines, and consequently 64 individually addressable electro-chemical devices were fabricated on glass wafers (Figure **5.18**a) using standard micro-processing techniques (Figure **5.18**b). After cleaning and surface treatment of the glass substrates (Section 5.1.2), a continuous layer of SU-8 was applied to smoothen the glass surface and serve as buffer. Ti back-gate electrodes (gate lines) were patterned via wet-etching (0.1 M NaF and 0.1 M $(NH_4)_2S_2O_8$) from DC magnetron-sputtered layers (100 nm). The gate lines were covered with a sandwich structure of $HfO_2^{6.2\,nm}/Al_2O_3^{3.5\,nm}/HfO_2^{6.2\,nm}$ using ALD to serve as gate dielectric. It was pattered with reactive ion etching (RIE) to expose the gate contact pads. The sandwich composition takes advantage of the high band gap of Al_2O_3 and the high dielectric constant of HfO_2, resulting in TFTs little leakage, high breakdown voltages, and little hysteresis. The semiconducting compound, namely a-IGZO (15 nm), was deposited via magnetron sputtering and wet etched in a 4 %$_{wt}$ oxalic acid solution. Prior to the processing of source and drain electrodes, an SU-8 interlayer was patterned to protect the semi-conductor channel during following processing steps. Onto the interlayer, source and drain electrodes were processed from RF magnetron sputtered layers of $Ti^{30\,nm}/Au^{30\,nm}$ and patterned using CF_4/Ar chemistry in a RIE process. The source and gate electrodes were designed to create TFTs with 200 µm long and 6.5 µm wide channels. Rectangles of SL were applied as discussed in Section 5.1.2 and covered with patterned Au digits that would later serve as actuator electrodes. The devices were finalized with a cover layer of SU-8 to mask the Au electrodes for CP deposition and improve

environmental stability through further encapsulation. Before operation, devices were hard baked at 200 °C to completely cross-link the SU-8 layers and improve electrode conductivity.

a Glass wafer with 12 TFT-AMs   **b** Layer stacks of TFT pixel with PPy actuators

c Transfer curve of a-IGZO TFT   **d** Output curve
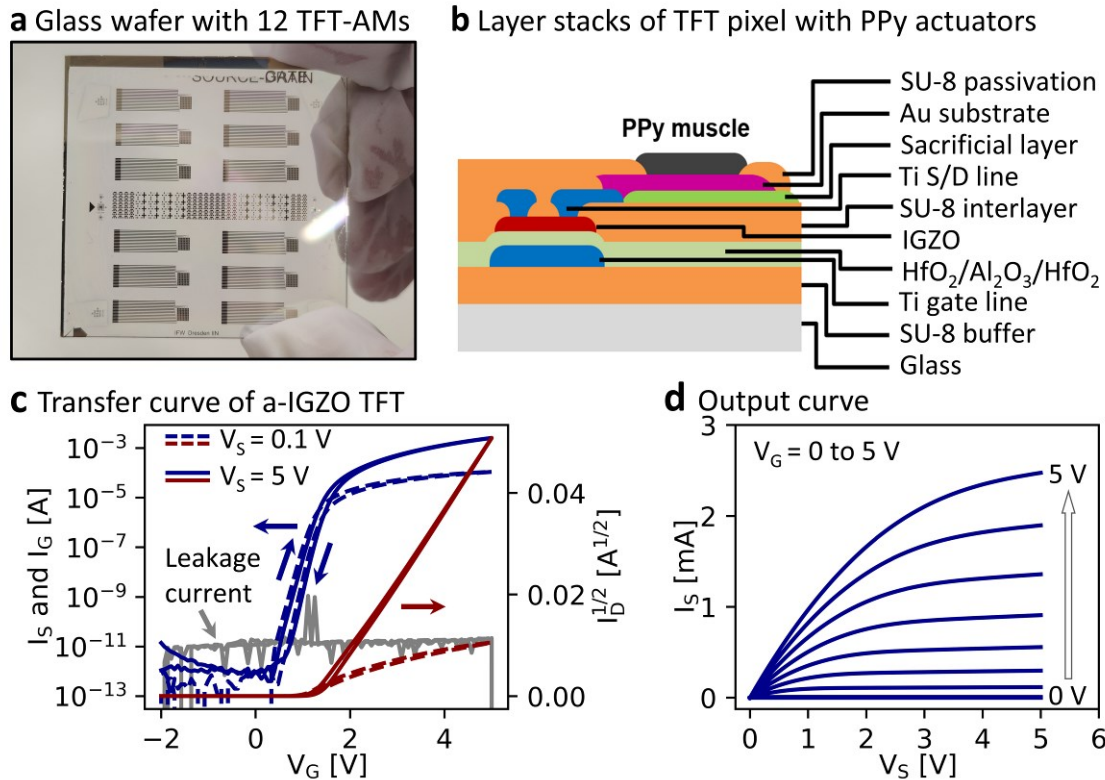
Figure 5.18: Properties of a-IGZO TFTs: (a) A 50 x 50 mm^2 glass substrate with 12 TFT-AMs and several test structures. **(b)** Layer stack of an individual pixel. **(c)** Typical transfer curve of a-IGZO TFT. The gate voltage was swept while the source voltage was kept constant. **(d)** Output curves of typical TFT. The Source-drain voltage was swept while the gate voltage was kept constant. TFT fabrication and characterization was performed by Dr. Bin Bao (Leibniz IFW Dresden). Figure adapted from [214].

Transfer curves of a typical TFT, i.e. the source current I_S and gate current I_G in dependence of the gate voltage V_G are depicted in Figure **5.18**c. The TFT offers an on-current of up to 2 mA and an off-current in the pA range, yielding an on/off ratio of almost 10^8, allowing the TFT to effectively act as a switch. The on-current is sufficiently high to deposit and operate micro-scale actuators as characterized in Section 5.2. The minor sub-threshold hysteresis visible in the transfer curve is inconsequential for the envisioned low-frequency applications. To obtain the output characteristics of TFTs, I_S was recorded in dependence on V_S while V_G was fixed at constant levels between 0 V and 5 V. Figure **5.18**d reveals the typical transistor behavior with a linear regime at first and a saturation beyond the pinch-off point. The fabrications yield of TFTs was around 98 %, which is sufficient for the application in AMs with only one transistor per pixel. The fabricated TFTs have an average mobility of (10.5 ± 0.8) cm^2 V^{-1} s^{-1}, that is consistent with

previous reports of a-IGZO transistors. The threshold voltage V_{th} of (1.1 ± 0.1) V allows to operate at low voltage, e.g. above 1.8 V.

5.5.2 FABRICATION AND OPERATION OF PPY ACTUATORS

To process PPy onto exposed Au electrode digits, the gate and source lines of an TFT-AM were connected to SMU and immersed in a monomer solution (Figure **5.19**a) that was prepared as discussed in Section 3.2.5. A counter electrode was immersed into the same electrolyte and connected to ground. To demonstrate the switching capability of the integrated TFTs, a constant bias voltage of V_S = 0.6 V was applied between the source lines and the counter electrode (ground). Then, a gate voltage V_G = 5.0 V was applied periodically every 5 s. It should be noticed that, in this configuration, the gate voltage is applied between the back-gate electrode and the counter electrode, hence the TFT is gated through the electrolyte solution. As displayed in Figure (Figure **5.19**b), the TFT effectively controls the deposition process, conducting the desired deposition current in the μA range when opened (V_G = 5.0 V) and reducing it to nA when closed (V_G = 0 V).
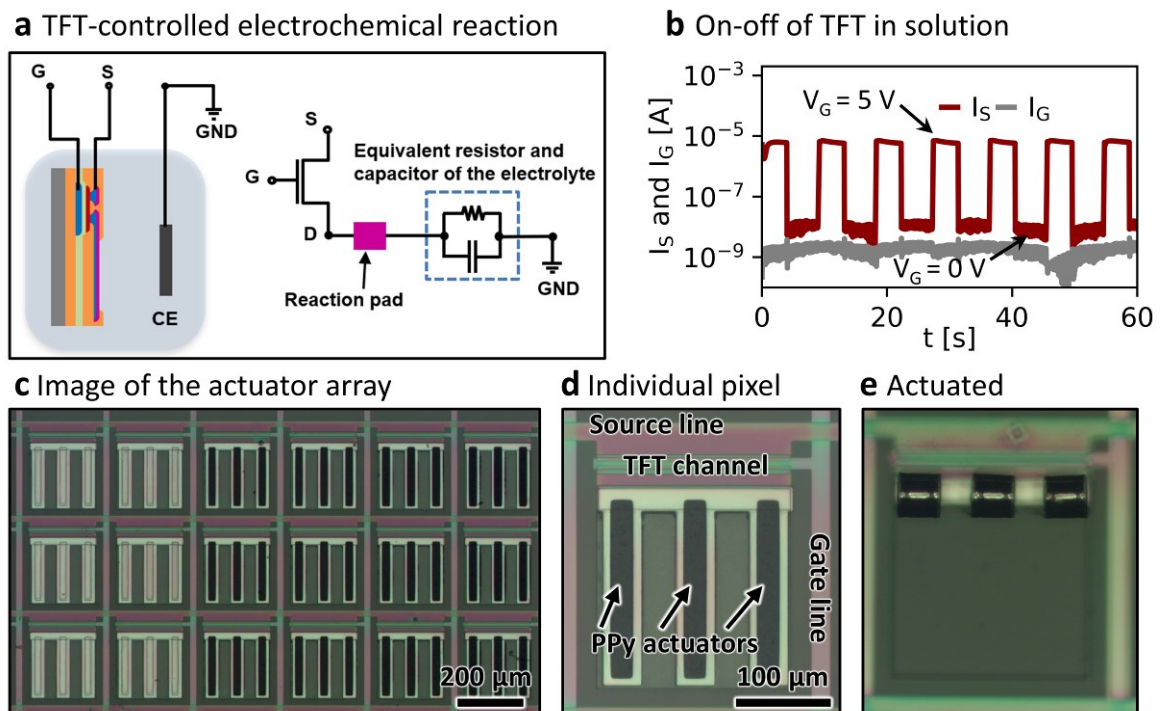
Figure 5.19: Deposition and actuation of PPy in an TFT-AM: (a) Circuit schematic of TFT-AM for digital electro-chemistry. **(b)** The deposition current is controlled with the TFT that is switched on and off with the gate bias. **(c)** Array of actuator pixels that are partially coated with PPy. **(d)** Individual actuator pixel with three PPy coated digits. **(e)** PPy actuator digits in their curled-up state. TFT-AMs with PPy were fabricated in collaboration with Dr. Bin Bao (Leibniz IFW Dresden). Figure adapted from [214].

In this configuration, PPy layers of about 2.8 μm were deposited onto the exposed Au electrode digits (175 x 20 μm^2) as displayed in Figure **5.19**c, where four columns of pixels are already coated. Figure **5.19**d shows an individual pixel with its corresponding source line, gate line, the TFT, and three PPy coated digits prior to release. After PPy deposition, the actuator compounds were released by selectively removing the SL in diluted HCl, rinsed with DI water, and transferred into a 0.1 M solution of NaDBS. After an initial voltage cycling to activate the PPy actuators, their shape could be varied between a flat state, and completely rolled-up (Figure **5.19**e) by applying voltages between – 1.3 V and 0.2 V, respectively.

5.5.3 SITE-SELECTIVE ACTUATION

To address individual pixels in an 8 x 8 AM, the source lines were connected to a microcontroller PCB with an 8–channel DAC and the gate lines were connected to an 8-stage shift register. The shift register could apply 5 V to open, or 0V to close all TFTs along a gate line. The controller electronics were operated from a custom-made GUI that allowed to apply gate voltages, define source voltages, and execute programmable sequences (Section 5.1.3). It should be noted that the application of a voltage to a gate line opens all eight TFTs along the corresponding column, while the application of a bias voltage to a source line affects all eight pixels in the corresponding row. An individual pixel is addressed, when both its associated source and gate lines are biased.

Figure **5.20** shows the site selection capabilities of this setup, highlighting a sub-matrix of 4 x 2 pixels. To flatten a single actuator in Figure **5.20**a, the TFTs in the leftmost column are opened and – 1.3 V are applied to the upper source line. The other pixels remain curled up since they are either exposed to 0 V (bottom left pixel) or their TFTs are closed. A negative bias of – 1.3 V is then applied to the bottom source line to flatten the second actuator as well in Figure **5.20**b. Similarly, an entire row of actuators can be flatted by opening all TFTs and applying the negative bias to the upper and 0 V to the lower row (Figure **5.20**c). All actuators are flattened by opening all TFTs and applying the negative bias to all source lines (Figure **5.20**d). It should be noted that more complex actuation patterns can be achieved by rapidly sweeping through the columns and applying the desired source biases on a time scale much faster than the rate of self-discharge of PPy actuators, which is in the order of tens of seconds.
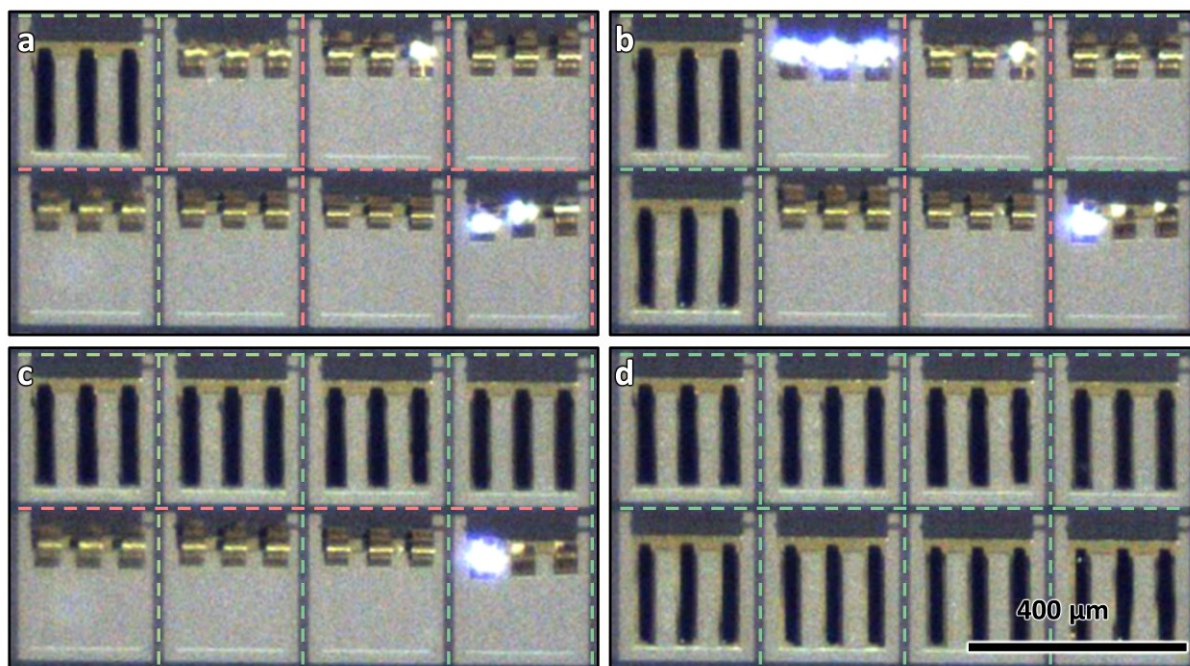
Figure 5.20: Site-selective actuation in a TFT-AM: The colors indicate the voltage applied to a specific line. Red indicates 0 V. Green indicates 5 V for gate lines (columns) and -1.3 V for source lines (rows). **(a)** One pixel is addressed by biasing one gate line and one source line. **(b)** One column is addressed by biasing one gate line and all source lines. **(c)** One row is addressed by biasing all gate lines and one source line. **(d)** All pixels are addressed by biasing all gate lines and all source lines. TFT-AMs with PPy were fabricated in collaboration with Dr. Bin Bao (Leibniz IFW Dresden). Figure adapted from [214].

This implementation demonstrates site-selective actuation with CP compounds. Future flexible micro-robotic devices will integrate similar heterogeneous circuits to achieve densely integrated actuator systems and enable complex shape control.

6   DISCUSSION AND OUTLOOK

6.1   INTEGRATED SELF-ASSEMBLED CATHETERS

This thesis introduces micro-catheters that offer electronic functionalities enabled by embedded electronic components. This integration effort is made possible through the combination of established techniques for sensing and actuation, as well as modern 3D self-assembly strategies. The application of self-rolling micro-patterned polymer structures can lead to a paradigm shift in the manufacturing of integrated micro-catheters.

ISACs are connected to micro-fluidic systems that allow to deliver liquid payloads in artificial and natural *ex vivo* environments in a targeted manner. A micro-manipulator is integrated at the tip of ISACs and can open and close rapidly and on demand. Its bio-compatibility and softness positions the manipulator ideally to grasp, transport, and release sensitive micro-sized objects. The ambitious goal to track the location and orientation of ISACs with high resolution and without harmful radiation and contrast agents was realized with the integrated sensing capabilities and a purpose-developed tracking strategy. ISACs constitute the first micro-catheters with monolithically integrated magnetic sensors, which were optimized to offer high sensitivity despite their tiny size. The considerable miniaturization of the magnetic sensor, compared to previously reported magnetic tracking strategies, was achieved through the integration and consequent omission of redundant packaging, conditioning circuits and internal connections. The multiple windings of the Swiss-roll architecture allowed to accommodate more magnetically sensitive material on a small device footprint. Using weak and low frequency alternating magnetic fields, position tracking of ISACs was demonstrated in 1D, within a limited working volume, and under laboratory conditions, but with an unprecedented spatial resolution, both in air and a water-filled phantom channel.

6.1.1 OUTLOOK

The navigation strategy developed specifically for ISACs should be extended to allow tracking with 5 DOF. Multiple sources will need to emit reference signals in sequential or parallel fashion to enable highly resolved position and orientation sensing throughout the

entire working volume. The real-time adjustment of the reference field and signal analysis should be driven by dedicated feedback-control algorithms and hardware[216].

The next step on the path towards the clinical application of ISACs requires comprehensive studies of bio-compatibility and performance under physiological conditions. All incorporated materials that are in contact with the environment, i.e. PPy, PI, and HG, have been previously found to be bio-compatible through cytotoxicity tests[124]. However, further investigations with *ex vivo* tissues are necessary to assess the mechanical performance of ISACs, while trials in animal models can examine physiological interactions such as hemocompatibility, immune response, acute irritation, and toxicity, as well as device handling and deployment.

Upcoming developments of ISACs should further integrate sensing capabilities that provide a comprehensive set of physiological parameters obtained *in situ*. Relevant measurements can include physiological parameters (blood flow, pressure, temperature, pH), blood gas analysis (O_2, CO_2), and the concentration of drugs and bio-molecules (inflammation markers, sugars, metabolism products).

The polymer platform, which is the basis of ISACs, requires further development before these devices can efficiently navigate intricate blood vessel networks. The compatibility of the shapeable polymer stack and CP micro-actuators was established in this thesis. The next objective should be to integrated a distributed system of independent micro-actuators along the entire micro-catheter to allow site selective shape control with multiple DOFs. These instruments would be able to actively adjust their shape to the traversed vessels, steer towards a desired direction, or even move autonomously to advance within a vessel without relying on outside forces. The Swiss-roll architecture of the polymer platform needs to be reworked to use the force of CP actuators efficiently, for instance by integrating joints with the ability to fold as they are known from origami[217].

The accommodation of numerous sensors and actuators will constitute a further challenge due to the limited surface area of these instruments. ISACs need to be equipped with sophisticated active electronics, including active matrices and shift registers[15,103,218], to address specific electronic components. Preliminary investigations into the heterogeneous integration of PPy actuators and active electronics were already presented in this thesis. The interplay of active electronics, sensors, and actuators will enable a new generation of surgical tools, namely integrated micro-robotic catheters.

6.2 Reshapeable micro-electronic devices

This thesis reports a strategy to fabricate flexible micro-scale devices that integrate soft actuators and sensors for feedback-driven actuation and shape control. This development achieves a long-standing goal of the micro-actuator field and forms a strong basis for the further development of flexible micro-robotics, shape-controlled FE, and soft micro-robotic surgical instruments. RMEDs were achieved by integrating multiple electronic components onto an ultra-thin and flexible polymer carrier platform that is processed in a monolithic wafer-scale fashion. The partial release of micro-patterned devices from the handling substrate, which has been previously regarded as technological challenge, was addressed through the incorporation of a metal-organic sacrificial layer. The rapid and controllable reshaping of RMEDs is realized using the established PPy-on-gold material system. The optimized geometry of RMEDs, whose realization was driven by a computational analysis, facilitates the efficient usage of actuator force and allows to minimize their footprint requirements. This adaptation allows to use as much as 80% of the device area for additional electronic components. This work demonstrates feedback-control of RMEDs with two complementary sensing strategies that offer themselves for different application scenarios. Magnetic sensors assess their orientation relative to an external field, allowing to position an RMED in absolute space. Alternatively, strain sensors assess the curvature of RMEDs directly. The real-time analysis of sensor signals with custom-developed external electronics allowed to implement an algorithm for automated obstacle detection. This functionality was demonstrated by automatically detecting contact with soft biological tissue during manipulation with an RMED. Moreover, digital electrochemistry was introduced to achieve the heterogeneous integration of CP actuators and active electronics. This effort resulted in a TFT-AM with 64 integrated PPy actuators, capable to address and actuate each device individually or in subsets.

6.2.1 Outlook

The feedback-controlled actuation of RMEDs relied on a simple PID algorithm. Although this approach is sufficient for an initial demonstration and simple positioning tasks, it is not well suited for such non-linear systems that might evolve in time. Dedicated control algorithms, which consider the specific properties of PPy[155], should be combined with sensor feedback to improve the performance of RMED shape control.

The presented RMEDs can serve as tools for grasping and manipulation. Upcoming iterations will integrate further electronic components, specifically additional sensors. The integration of passive or even actively amplified capacitive sensing electrodes, for instance, would transform RMEDs into shape and force-tunable cuff-implants for neural interfacing[85,86]. Taking advantage of the active shape control, these implants will be more compact, yet easier to handle, compared to their mechanically passive counterparts. Further intriguing opportunities for minimally invasive interventions will be offered by integrated pressure sensors[219], radio-frequency ablation electrodes[89], US transducers[18], and opto-electronic components[220] for sensing and stimulation. The integration of numerous electronic components is restricted by the limited device area. On-board multiplexing using active matrices or shift register circuits will be crucial to use valuable surface area efficiently and accommodate more electronic components. The basis for these developments was achieved in this thesis through the heterogeneous integration of PPy actuators into a TFT-AM.

While the integration of PPy actuators with electronic sensors was explored in this thesis, intriguing perspectives arise from devices that further embed an energy source and control unit. Such systems would not rely on external power supply and data evaluation, and might be developed into untethered and motile micro-systems, for instance as medical micro-bots. A preliminary investigation towards such a system was recently reported by our group, where a self-assembled system featured PPy actuators, an on-board energy source, and electro-mechanical feedback to autonomously generate mechanical oscillation[221].

This work is centered around RMEDs that are processed in planar and offer one dimension of feedback-driven shape control. Future micro-robotic systems, in contrast, should take on elaborated 3D shapes and integrate a distributed system of sensors and actuators for precise shape control with many DOFs. The transformation of planar layer stacks into robust 3D structures will be achieved through self-assembly strategies, including folding, buckling, and rolling, allowing to create complex 3D micro-robotic systems.

7 CONCLUSION

This thesis explores strategies for the fabrication of micro-scale instruments with electronic and mechanical functionalities. The integration of various stimuli responsive materials that reshape according to orthogonal triggers enables devices that, starting from initial 2D structures, first take on 3D shapes to then offer active shape control. This actuation of mechanically functional 3D devices leads the way towards tethered micro-robotic instruments. Self-assembling instruments, while in their planar state, are compatible with standard micro-fabrication and can thus benefit from the rich set of manufacturing schemes present in the semi-conductor and micro-electronics industry. The integration of components for actuation and sensing into combined micro-systems, however, demands specific measures to reconcile their processing and application conditions, both on a device and operational level. Micro-electronic integration facilitates mechanically functional instruments with embedded components that offer electro-mechanical, electro-chemical, and electro-magnetic functionalities, giving rise to systems that perceive their environment and even interact with it. Instruments based on this paradigm might advance minimally invasive surgical interventions. The native shape control of micro-robotic instruments through embedded actuators replaces the requirement for external forces and mechanical force transmission, facilitating completely soft devices at small scales. On-board sensors allow to monitor the intervention, interface and probe surrounding tissue, and thereby compensate the surgeon's lost senses of sight and touch during MIS. Foreseeable developments might decisively contribute to MIS by expanding its reach into smaller anatomies, allowing for safe manipulation of the most sensitive tissues, reducing the operational difficulty for medical practitioners through comprehensive feedback, and could even provide a full account of the intervention through real-time analysis of physiological parameters. The presented devices form a strong basis for the future development of micro-robotic surgical instruments, which assess their environments to position themselves, manipulate tissues, administer drugs, and carry out interventions, all in a semi-autonomous fashion.

APPENDIX

A1 PROCESSING PARAMETERS FOR POLYMER STACK LAYERS

Material	Prebake	Exposure	Developer	Rinse	Hard bake
SL	10 min @ 35°C	250 mJ cm^{-1}	30 s @ DI water	20 s @ PMA[1]	10 min @ 220°C
HG	10 min @ 40°C	450 mJ cm^{-1}	2.5 min @ DEGMEE[2]	40 s @ PMA	10 min @ 220°C
PI	10 min @ 50°C	600 mJ cm^{-1}	3 min @ NEP[3]/DEGMEE/EtOH[4] (4:2:1)	5 s @ PMA	20 min @ 220°C

[1](1 methoxy 2 propyl) acetate [2] diethylene glycole monoethyl ether [3] N-ethyl pyrrolidone [4]ethanol

A2 DERIVATION OF MAGNETIC PHASE PROFILE IN 3D

Magnetic phase-encoded tracking can be performed in 3D to navigate tools with 5 DOF. The total field is again a superposition of two reference fields $\vec{B} = \vec{B_1} + \vec{B_2}$, that are generated by two source coils at positions $\pm\vec{D}$ as indicated in the illustration. The relative separation between source and sensor are $\vec{R_1} = \vec{P} + \vec{D}$ an $\vec{R_2} = \vec{P} - \vec{D}$. Using the model for magnetic dipoles in 3D (Equation 4.1), the constituent fields read

$$\vec{B}_{1/2}\left(\vec{P}; \vec{D}\right) = \frac{\mu_0}{4\pi} \cdot \frac{3\left(\vec{P} \pm \vec{D}\right)\left(\vec{M}_{1/2} \cdot \left(\vec{P} \pm \vec{D}\right)\right) - \vec{M}_{1/2}\left(\vec{P} \pm \vec{D}\right)^2}{(\vec{P} \pm \vec{D})^5} \qquad \text{Eq. A.1}$$

where $\vec{M}_{1/2}$ are the magnetizations of the source coils. By design, the source magnetizations align with the source position vector $\vec{D}$. When supplied with two phase-shifted currents as above, the source magnetizations are

$$\vec{M}_1 = M_{1,0} \cdot \sin(\omega t) \frac{\vec{D}}{\sqrt{D^2}} \qquad \text{Eq. A.2}$$

$$\vec{M}_2 = M_{2,0} \cdot \sin(\omega t + 90°) \frac{\vec{D}}{\sqrt{D^2}} \qquad \text{Eq. A.3}$$

where $M_{1,0}$ and $M_{2,0}$ indicate the magnetization amplitude that is defined by the supply current.

$\pm D$	- Positions of source coils from center
R_1, R_2	- Relative separation of sources and sensor
P	- Position of sensor (ISAC tip)
S	- Orientation of sensor (ISAC long axis)
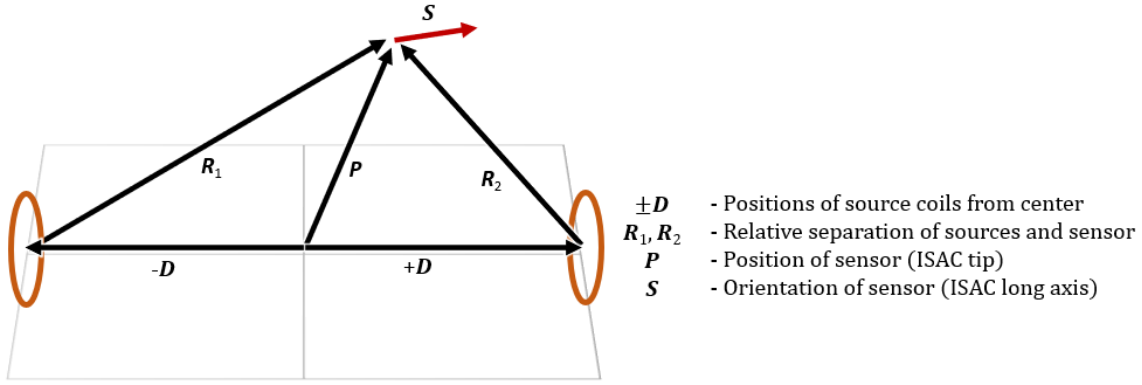
When measuring a weak magnetic field (< 1mT), the integrated AMR sensor detects the projection onto the sensing axis, i.e. the component of the field vector that aligns with the sensitive axis. In ISACs, the AMR sensing axis aligns with long catheter axis, i.e. its orientation. The sensor output O is thus proportional to the dot-product of an external field $\vec{B}(\vec{P})$ at the sensor position $\vec{P}$ and the ISAC orientation $\vec{S}$

$$O = s \cdot \vec{B}(\vec{P}) \cdot \vec{S} \qquad \text{Eq. A.4}$$

with the constant s linking sensor properties and electronic output, and using the sensor orientation described by the unit vector $\vec{S}$. Inserting Equations A.2 and A.3, the sensor output is

$$O = s \cdot \vec{B}(\vec{P}) \cdot \vec{S} = s \cdot (\vec{B}_1(\vec{P}, t; \vec{D}) \cdot \vec{S}) + (\vec{B}_2(\vec{P}, t; \vec{D}) \cdot \vec{S})$$

$$= \frac{s\,\mu_0 M_{1,0}\sin(\omega t)}{4\pi} \left(\frac{3(\vec{P}+\vec{D})\left(\frac{\vec{D}}{\sqrt{D^2}} \cdot (\vec{P}+\vec{D}) \right) - \frac{\vec{D}}{\sqrt{D^2}}(\vec{P}+\vec{D})^2}{(\vec{P}+\vec{D})^5} \right) \cdot \vec{S}$$

$$+ \frac{s\,\mu_0 M_{2,0}\sin(\omega t + 90°)}{4\pi} \left(\frac{3(\vec{P}-\vec{D})\left(\frac{\vec{D}}{\sqrt{D^2}} \cdot (\vec{P}-\vec{D}) \right) - \frac{\vec{D}}{\sqrt{D^2}}(\vec{P}-\vec{D})^2}{(\vec{P}-\vec{D})^5} \right) \cdot \vec{S} \quad \text{Eq. A.5}$$

The relative orientation and position of the sensors and source coils can be summarized in the geometry factors g_1 and g_2 corresponding to source coil one and two, respectively

$$g_1 = \frac{s \cdot \mu_0}{4\pi} \sum_{k \in (1,2,3)} \left(\frac{3(\vec{P}+\vec{D})_k \left(\frac{\vec{D}}{\sqrt{D^2}} \cdot (\vec{P}+\vec{D}) \right) - \frac{D_k}{\sqrt{D^2}}(\vec{P}+\vec{D})^2}{(\vec{P}+\vec{D})^5} \right) \cdot S_k \quad \text{Eq. A.6}$$

$$g_2 = \frac{s \cdot \mu_0}{4\pi} \sum_{k \in (1,2,3)} \left(\frac{3(\vec{P} - \vec{D})_k \left(\frac{\vec{D}}{\sqrt{\vec{D}^2}} \cdot (\vec{P} - \vec{D}) \right) - \frac{D_k}{\sqrt{\vec{D}^2}} (\vec{P} - \vec{D})^2}{(\vec{P} - \vec{D})^5} \right) \cdot S_k \qquad \text{Eq. A.7}$$

Summarizing Equation A.5 with the harmonic addition theorem (Equation 4.5), the expected sensor signal reads

$$O = \frac{s \cdot \mu_0}{4\pi} \sqrt{\left(M_{1,0} \cdot g_1 \right)^2 + \left(M_{2,0} \cdot g_2 \right)^2} \cdot \sin(\omega t + d\phi) \qquad \text{Eq. A.8}$$

with

$$d\phi = d\phi(\vec{P}, \vec{S}; \vec{D}) = \arctan\left(\frac{M_{2,0}}{M_{1,0}} \cdot \frac{g_2}{g_1} \right) \qquad \text{Eq. A.9}$$

Equation A.9 implies that the phase shift $d\phi$, which can be measured experimentally, depends on the known positions of the source coils $\vec{D}$ = (D1, D2, D3), and the unknown position $\vec{P}$ = (P1, P2, P3) and orientation $\vec{S}$ = (S1, S2, S3) of the ISAC tip. This equation includes a total of six unknown variables, which is reduced by one, since by definition $S_3 = \sqrt{1 - S_1^2 - S_2^2}$. To identify the position and orientation of an ISAC with 5 DOF, i.e. solve Equation A.9 for $\vec{P}$ and $\vec{S}$, at least five measurements of $d\phi$ with different source pairs, i.e. five different $\vec{D}$, are required. In practice, additional source pairs should be used for redundancy. It should be noted that the special case $\vec{D}$ = (d, 0, 0), $\vec{P}$ = (p, 0, 0), and $\vec{S}$ = (1, 0, 0) where all vectors align with the x-axis and Equation A.9 reduces to the known 1D case found in Equation 4.7.

BIBLIOGRAPHY

[1]   M. Siddaiah-Subramanya, K. Tiang, M. Nyandowe, *Surg. J.* **2017**, *03*, e163.

[2]   J. Piek, G. Lidke, T. Terberger, *Zentralbl. Neurochir.* **2011**, *72*, 42.

[3]   M. Sachs, J. Bojunga, A. Encke, *World J. Surg.* **1999**, *23*, 1088.

[4]   D. Murrell, MNT Editorial Team, Modern medicine: Infectious diseases, timelines, and challenges, (https://www.medicalnewstoday.com/articles/323538) (accessed 17. 12. 2021).

[5]   K. K. M. Ng, J. P. Y. Cheung, *J. Orthop. Surg.* **2017**, *25*, 230949901771625.

[6]   Z. Xia, X. Wu, J. Li, Z. Liu, F. Chen, L. Zhang, H. Zhang, X. Wan, Q. Cheng, *World Neurosurg.* **2018**, *115*, 266.

[7]   O. O. Akinduro, P. Kerezoudis, M. A. Alvi, J. W. Yoon, J. Eluchie, M. H. Murad, Z. Wang, S. G. Chen, M. Bydon, *World Neurosurg.* **2017**, *108*, 924.

[8]   V. K. Goel, "Tomorrow's Solutions to Today's Challenges in Minimally Invasive Surgery - Patient Safety & Quality Healthcare," (https://www.psqh.com/analysis/tomorrows-solutions-to-todays-challenges-in-minimally-invasive-surgery/) (accessed 17. 12. 2021)

[9]   B. Avitall, *Catheter Deflection Control, US Patent No. US5441483A*, **1993**.

[10] W. F. Muller, *Spring Guide Manipulator, US Patent No. US3452740A*, **1969**.

[11] V. A. Andrushko, J. W. Verano, *Am. J. Phys. Anthropol.* **2008**, *137*, 4.

[12] H. v. Gersdorff, "Feldbüch der Wundartzney" (1497)

[13] Image courtesy of Brother UK Ltd. (https://www.brother.co.uk/business-solutions/healthcare/future-of-hospital-technology)

[14] J. Kim, M. Lee, H. J. Shim, R. Ghaffari, H. R. Cho, D. Son, Y. H. Jung, M. Soh, C. Choi, S. Jung, K. Chu, D. Jeon, S.-T. Lee, J. H. Kim, S. H. Choi, T. Hyeon, D.-H. Kim, *Nat. Commun.* **2014**, *5*, 5747.

[15] M. Kondo, M. Melzer, D. Karnaushenko, T. Uemura, S. Yoshimoto, M. Akiyama, Y. Noda, T. Araki, O. G. Schmidt, T. Sekitani, *Sci. Adv.* **2020**, *6*, 1.

[16] D. H. Kim, J. H. Ahn, M. C. Won, H. S. Kim, T. H. Kim, J. Song, Y. Y. Huang, Z. Liu, C. Lu, J. A. Rogers, *Science* **2008**, *320*, 507.

[17] H. U. Chung, A. Y. Rwei, A. Hourlier-Fargette, S. Xu, K. H. Lee, E. C. Dunne, Z. Xie, C. Liu, A. Carlini, D. H. Kim, D. Ryu, E. Kulikova, J. Cao, I. C. Odland, K. B. Fields, B. Hopkins, A. Banks, C. Ogle, D. Grande, J. Bin Park, J. Kim, M. Irie, H. Jang, J. H. Lee, Y. Park, J. Kim, H. H. Jo, H. Hahm, R. Avila, Y. Xu, M. Namkoong, J. W. Kwak, E. Suen, M. A. Paulus, R. J. Kim, B. V. Parsons, K. A. Human, S. S. Kim, M. Patel, W. Reuther, H. S. Kim, S. H. Lee, J. D. Leedle, Y. Yun, S. Rigali, T. Son, I. Jung, H. Arafa, V. R. Soundararajan, A. Ollech, A. Shukla, A. Bradley, M. Schau, C. M. Rand, L. E. Marsillio, Z. L. Harris, Y. Huang, A. Hamvas, A. S. Paller, D. E. Weese-Mayer, J. Y. Lee, J. A. Rogers, *Nat. Med.* **2020**, *26*, 418.

[18] C. Wang, X. Li, H. Hu, L. Zhang, Z. Huang, M. Lin, Z. Zhang, Z. Yin, B. Huang, H. Gong, S. Bhaskaran, Y. Gu, M. Makihata, Y. Guo, Y. Lei, Y. Chen, C. Wang, Y. Li, T. Zhang, Z. Chen, A. P. Pisano, L. Zhang, Q. Zhou, S. Xu, *Nat. Biomed. Eng.* **2018**, *2*, 687.

[19] Y. Lee, J. W. Chung, G. H. Lee, H. Kang, J.-Y. Kim, C. Bae, H. Yoo, S. Jeong, H. Cho, S.-G. Kang, J. Y. Jung, D.-W. Lee, S. Gam, S. G. Hahm, Y. Kuzumoto, S. J. Kim, Z. Bao, Y. Hong, Y. Yun, S. Kim, *Sci. Adv.* **2021**, *7*, abg9180.

[20] A. M. Cobo, C. E. Larson, K. Scholten, J. A. Miranda, S. Elyahoodayan, D. Song, V. Pikov, E. Meng, *J. Microelectromechanical Syst.* **2019**, *28*, 36.

[21] C. M. Boutry, L. Beker, Y. Kaizawa, C. Vassos, H. Tran, A. C. Hinckley, R. Pfattner, S. Niu, J. Li, J. Claverie, Z. Wang, J. Chang, P. M. Fox, Z. Bao, *Nat. Biomed. Eng.* **2019**, *3*, 47.

[22] Y. S. Choi, R. T. Yin, A. Pfenniger, J. Koo, R. Avila, K. Benjamin Lee, S. W. Chen, G. Lee, G. Li, Y. Qiao, A. Murillo-Berlioz, A. Kiss, S. Han, S. M. Lee, C. Li, Z. Xie, Y. Y. Chen, A. Burrell, B. Geist, H. Jeong, J. Kim, H. J. Yoon, A. Banks, S. K. Kang, Z. J. Zhang, C. R. Haney, A. V. Sahakian, D. Johnson, T. Efimova, Y. Huang, G. D. Trachiotis, B. P. Knight, R. K. Arora, I. R. Efimov, J. A. Rogers, *Nat. Biotechnol.* **2021**, *39*, 1228.

[23] L. Klinker, S. Lee, J. Work, J. Wright, Y. Ma, L. Ptaszek, R. C. Webb, C. Liu, N. Sheth, M. Mansour, J. A. Rogers, Y. Huang, H. Chen, R. Ghaffari, *Extrem. Mech. Lett.* **2015**, *3*, 45.

[24] C. Li, C. H. Ahn, L. A. Shutter, R. K. Narayan, *Biosens. Bioelectron.* **2009**, *25*, 173.

[25] J. H. Na, A. A. Evans, J. Bae, M. C. Chiappelli, C. D. Santangelo, R. J. Lang, T. C. Hull, R. C. Hayward, *Adv. Mater.* **2015**, *27*, 79.

[26] M. Han, H. Wang, Y. Yang, C. Liang, W. Bai, Z. Yan, H. Li, Y. Xue, X. Wang, B. Akar, H. Zhao, H. Luan, J. Lim, I. Kandela, G. A. Ameer, Y. Zhang, Y. Huang, J. A. Rogers, *Nat. Electron.* **2019**, *2*, 26.

[27] D. Karnaushenko, D. D. Karnaushenko, D. Makarov, S. Baunack, R. Schäfer, O. G. Schmidt, *Adv. Mater.* **2015**, *27*, 6582.

[28] D. D. Karnaushenko, D. Karnaushenko, D. Makarov, O. G. Schmidt, *NPG Asia Mater.* **2015**, *7*, e188.

[29] L. Dvali, S. Mackinnon, *Hand Clin.* **2007**, *23*, 73.

[30] M. G. Patti, A. H. Zureikat, A. Fichera, F. Schlottmann, Eds. , *Techniques in Minimally Invasive Surgery*, Springer International Publishing, Cham, **2021**.

[31] P. Lanzer, Ed. , *Textbook of Catheter-Based Cardiovascular Interventions*, Springer International Publishing, Cham, **2018**.

[32] Z. Yuan, Z. Woha, X. Weiming, *Clin. Neurol. Neurosurg.* **2013**, *115*, 57.

[33] M. Shimohira, H. Ogino, T. Kawai, A. Kushita, M. Watanabe, T. Kawaguchi, K. Kurono, Y. Shibamoto, *Br. J. Radiol.* **2011**, *84*, 184.

[34] D. F. Vollherbst, C. M. Sommer, C. Ulfert, J. Pfaff, M. Bendszus, M. A. Möhlenbruch, *Am. J. Neuroradiol.* **2017**, *38*, 1377.

[35] P. Maury, B. Monteil, L. Marty, A. Duparc, P. Mondoly, A. Rollin, *Arch. Cardiovasc. Dis.* **2018**, *111*, 456.

[36] W. Forssmann, *Klin. Wochenschr.* **1929**, *8*, 2085.

[37] V. K. Venkiteswaran, J. J. Palao, S. Misra, in *2021 IEEE/ASME Int. Conf. Adv. Intell. Mechatronics*, IEEE, **2021**, pp. 848–854.

[38] J. Lussi, M. Mattmann, S. Sevim, F. Grigis, C. De Marco, C. Chautems, S. Pané, J. Puigmartí-Luis, Q. Boehler, B. J. Nelson, *Adv. Sci.* **2021**, *8*, 2101290.

[39] Genesis robotic catheter system *Stereotaxis* (https://www.stereotaxis.com/products/) (accessed 17. 12. 2021)

[40] D. A. Stidd, D. K. Lopes, M. Chen, *Neurointervention* **2014**, *9*, 39.

[41] Thermcool RMT catheter *Biosense Webster* (https://www.jnjmedicaldevices.com/en-US/product/thermocool-rmt-catheter) (accessed 17. 12. 2021)

[42] H. A. Jaeger, P. Nardelli, C. O'Shea, J. Tugwell, K. A. Khan, T. Power, M. O'Shea, M. P. Kennedy, P. Cantillon-Murphy, *IEEE Trans. Biomed. Eng.* **2017**, *64*, 1972.

[43] T. Skála, M. Táborský, *Cor Vasa* **2015**, *57*, e470.

[44] Licensed under CC BY-SA 3.0 (https://commons.wikimedia.org/w/index.php?curid=5581124)

[45] Licensed under CC BY-SA 3.0 (http://www.scientificanimations.com/wiki-mages/)

[46] Image courtesy of Abbott Laboratories (https://www.cardiovascular.abbott/us/en/hcp/products/electrophysiology/ablation-technology/tacticath-se-ablation-catheter/about/compatible-products.html, https://www.cardiovascular.abbott/us/en/hcp/products/electrophysiology/ablation-technology/tacticath-se-ablation-catheter/about.html)

[47] A. M. Franz, T. Haidegger, W. Birkfellner, K. Cleary, T. M. Peters, L. Maier-Hein, *IEEE Trans. Med. Imaging* **2014**, *33*, 1702.

[48] H. A. Jaeger, A. M. Franz, K. O'Donoghue, A. Seitel, F. Trauzettel, L. Maier-Hein, P. Cantillon-Murphy, *Int. J. Comput. Assist. Radiol. Surg.* **2017**, *12*, 1059.

[49] D. Bhakta, J. M. Miller, *Indian Pacing Electrophysiol. J.* **2008**, *8*, 32.

[50] Y. H. Kim, S. A. Chen, S. Ernst, C. E. Guzman, S. Han, Z. Kalarus, C. Labadet, Y. J. Lin, L. W. Lo, A. Nogami, E. B. Saad, J. Sapp, C. Sticherling, R. Tilz, R. Tung, Y. G. Kim, M. K. Stiles, *J. Arrhythmia* **2020**, *36*, 215.

[51] M. Zaaroor, Y. Bejerano, Z. Weinfeld, S. Ben-Haim, *Neurosurgery* **2001**, *48*, 1100.

[52] A. Schwein, B. Kramer, P. Chinnadurai, N. Virmani, S. Walker, M. O'Malley, A. B. Lumsden, J. Bismuth, *J. Vasc. Surg.* **2018**, *67*, 1274.

[53] A. Hakime, F. Deschamps, E. G. M. De Carvalho, A. Barah, A. Auperin, T. De Baere, *Cardiovasc. Intervent. Radiol.* **2012**, *35*, 898.

[54] Aurora Sensors *Northern Digital Inc.* (https://www.ndigital.com/products/aurora/aurora-sensors) (accessed 17. 12. 2021).

[55] A. Gudeloglu, J. V. Brahmbhatt, S. J. Parekattil, *Semin. Plast. Surg.* **2014**, *28*, 11.

[56] C. S. Lai, C. Te Lu, S. A. Liu, Y. C. Tsai, Y. W. Chen, I. C. Chen, *Microsurgery* **2019**, *39*, 715.

[57] N. Enayati, E. De Momi, G. Ferrigno, *IEEE Rev. Biomed. Eng.* **2016**, *9*, 49.

[58] Image courtesy of Intuitive Surgical (https://www.intuitive.com/en-us/about-us/press/press-resources)

[59] L. W. Y. Chen, M. Goh, R. Goh, Y. K. Chao, J. J. Huang, W. L. Kuo, C. W. H. Sung, J.

Chuieng-Yi Lu, D. C. C. Chuang, T. N. J. Chang, *J. Reconstr. Microsurg.* **2021**, *37*, 503.

[60] J. T. Mortimer, W. F. Agnew, K. Horch, P. Citron, G. Creasey, C. Kantor, *IEEE Trans. Rehabil. Eng.* **1995**, *3*, 145.

[61] C. J. De Luca, L. J. Bloom, L. D. Gilmore, *Orthopedics* **1987**, *10*, 777.

[62] H. C. Powell, R. R. Myers, *Lab. Investig.* **1986**, *55*, 91.

[63] J. Reeder, M. Kaltenbrunner, T. Ware, D. Arreaga-Salas, A. Avendano-Bolivar, T. Yokota, Y. Inoue, M. Sekino, W. Voit, T. Sekitani, T. Someya, *Adv. Mater.* **2014**, *26*, 4967.

[64] Y. Zhang, L. Zhang, K. Cui, S. Ge, X. Cheng, M. Yan, J. Yu, H. Liu, *Adv. Mater.* **2018**, *30*, 1801588.

[65] D. Karnaushenko, D. Makarov, C. Yan, R. Streubel, O. G. Schmidt, *Adv. Mater.* **2012**, *24*, 4518.

[66] M. Amjadi, M. Sitti, *ACS Nano* **2016**, *10*, 10202.

[67] M. Kaltenbrunner, T. Sekitani, J. Reeder, T. Yokota, K. Kuribara, T. Tokuhara, M. Drack, R. Schwödiauer, I. Graz, S. Bauer-Gogonea, S. Bauer, T. Someya, *Nature* **2013**, *499*, 458.

[68] T. Baëtens, E. Pallecchi, V. Thomy, S. Arscott, *Sci. Rep.* **2018**, *8*, 2045.

[69] G. Lanzara, N. Salowitz, Z. Guo, F. K. Chang, *Adv. Mater.* **2010**, *22*, 4643.

[70] N. Münzenrieder, D. Karnaushenko, L. Petti, G. Cantarella, C. Vogt, L. Büthe, D. D. Karnaushenko, O. G. Schmidt, D. Makarov, G. Tröster, *Adv. Electron. Mater.* **2016**, *2*, 1600188.

[71] Z. Xiang, S. C. Yen, N. Xue, T. Sun, W. M. Tsang, S. Zhang, L. De Liao, N. V. Thakor, C. Lee, *J. Micromechanics Microengineering* **2014**, *24*, 065015.

[72] J. T. Reeder, T. Kang, S. Rains, W. Voit, *Adv. Mater.* **2018**, *30*, 1706733.

[73] M. S. Mannoor, H. Tao, J. D. Clayton, A. Sengupta, D. L. Kaplan, R. R. Naik, N. Verma, F. G. Omenetto, M. C. McAlpine, *Nat. Commun.* **2012**, *3*, 1.

[74] H. G. Yoo, S. Kim, K. J. Lee, *RSC Adv.* **2014**, *4*, 20017.

[75] J. Biggs, J. Myers, J. Kufel, E. Ozer, S. Craske, A. Sou, C. Ramsdale, K. Williamson, R. Price, S. White, *Nature* **2021**, *595*, 532.

[76] J. Liang, L. Li, X. Niu, Z. Yu, Q. Pei, *Nat. Photonics* **2013**, *7*, 817.

[77] B. H. Kim, K. Li, J. T. Kim, Y. Park, H. Jang, X. Wang, Z. Xie, S. M. Won, H. J. Yoon, G. Lee, W. J. Jang, K. H. Lee, T. S. Chung, Y. H. Jung, S. Y. Heo, Y. Lee, J. Kim, T. Cai, Y. Kim, P. Prasopsukh, Y. Yu, X. Yu, R. Avila, H. Luan, H. Song, F. Zhu, Y. Zhao, L. Chen, S. H. Han, J. Kim, S. J. Oh, H. Lee, C. H. Lee, Y. Huang, L. P. Chamorro, Y. Zhang, J. A. Rogers, *Nature* **2021**, *597*, 503.

[78] Kenry, J. C. Yeo, C. T. Lim, *Microsystems Nanoeng.* **2016**, *2*, 16043.

[79] D. H. Keum, S.-K. Kim, J. Koo, G.-H. Lee, C. Jeon, J. W. Mok, B. H. Mun, K. J. Lee, E. Kamrani, C.-K. Joo, S. Shin, J.-Y. Sim, D. Myung, S. H. Yun, Z. Bao, S. K. Hahn, *Sci. Adv.* **2020**, *6*, eaba3252.

[80] G. S. Cañón Bermúdez, D. D. Karnaushenko, D. Karnaushenko, A. Lebanov, L. Bischoff, M. Kaltenbrunner, J. Fassbender, O. G. Schmidt, D. Makarov, *Sci. Adv.*

2018, *4*, eaao2623.

[81] H. Hu, X. Zhu, C. Wang, L. Zhang, X. Li, S. Lee, Z. Huang, R. Chen, Z. Chen, C. Wang, Y. Gu, Y. Chen, Y. Lei, T. Zhang, N. H. Kim, Y. Guo, Y. Teng, W. Zhou, Y. Li, A. Nomoto, S. Sternini, Q. Zhou, M. Pharr, F. L. Di Scalea, S. Xu, *Sci. Adv.* **2018**, *4*, eaar3979.

[82] C. Wang, B. Qi, M. Lin, Z. Zhang, M. Makihata, B. Liu, S. Zhou, Y. hsi Huang, H. Hu, Y. Gu, Y. Chen, Y. Lei, T. Lee, S. Chien, K. I. Jang, E. B. Kistler, S. Xu, *Nat. Biomed. Eng.* **2021**, *5*, 749.

[83] Image courtesy of Northwestern University (https://news.northwestern.edu/ stories/2021/september/microflier-winged-microchip-is-smallest-ever-human-made-flying-structure/)

[84] L. Jones, A. Hui, C.-M. Phan, M. L. Read, D. Azar, J. Buch, J. B. Ciolino, S. A. Naroo, B. Pall, K. Romond, P. Sankaridurg, C. M. Schnider, L. Terry, M. Willcox, *Contact Lens Anterior Eye* **2021**, *44*, 398.

[85] M. A. González-González, A. Kanneganti, A. Joshi-Imre, A. G. Hernandez-Reynoso, G. Bendale, R. Modi, M. Ecker, A. Khurram, S. F. Cogan, W. E. Voit, M. I. Romero-Ortega, *Sci. Rep.* **2018**, *8*, 16390.

[86] D. Karnaushenko, N. Münzenrieder, D. D. Karnaushenko, B. Koch, A. K. Meyer, S. Baunack, L. Petti, G. Tröster, D. Makarov, O. G. Schmidt, *Adv. Mater.* **2015**, *27*, 6797.

[87] J. Carey, A. Fahim, M. Munro, *J. Biomed. Mater. Res. - Part B Appl. Biomater.* **2004**, *70*, 73.

[88] D. H. Kim, N. Lu, R. Ghaffari, Y. S. Kim, S. P. Lee, L. Xu, J. Wu, R. H. Kim, J. Song, Z. Liu, J. Viventi, B. De Graff, B. Elolampi, M. Mansour, M. J. Slepian, S. Hwang, J. D. Moss, S. M. Won, Y. Huang, B. Litt, J. A. Rogers, *Nat. Mater.* **2011**, *10*, 316.

[89] M. Han, L. Chen, K. Aras, C. Liang, X. Chen, H. Zhao, K. Li, N. R. Faye, B. Sun, J. H. Kim, W. Bai, Q. Yang, Y. Ma, W. Lu, E. Song, J. M. Baek, Y. Lee, C. Liu, J. B. Model, G. Yang, R. Ghaffari, Y. Huang, I. R. Efimov, J. A. Rogers, *Nat. Biomed. Eng.* **2020**, *4*, 997.

[90] C. Li, P. M. Wu, J. Han, C. H. Ahn, *Biomed. Microdevices* **2008**, *10*, 671.

[91] C. Li, Z. Wu, K. Limnuson, C. Cheyuo, P. Wang, C. H. Ahn, R. K. Narayan, J. A. Hartings, *Biomed. Microdevices* **2016**, *18*, 1.

[92] N. L. Opie, S. E. John, G. S. Rind, S. M. Ronayne, Y. T. Wong, G. Gerboni, P. E. Yoo, T. J. H. Lovell, T. C. M. Scordas, S. L. Wilson, A. Dornom, T. Vale, T. J. O'Brien, D. B. Grayden, C. N. May, T. J. Oxley, *Nat. Biomed. Eng.* **2018**, *2*, 907.

[93] V. McMains, L. Nelson, *Updated Classification System Captures Many More People at Risk for Heart Attack* - 01/11/2017, (https://www.hopkinsmedicine.org /news/media/releases/updated_classification_system_captures_many_more_peo ple_at_risk_for_heart_attack) (accessed 17. 12. 2021).

[94] J. D. Paulsen, V. Démery, C. D. Santangelo, T. P. Russell, B. Davidovitch, N. Menon, *Nat. Mater.* **2015**, *14*, 1206.

[95] Y. Zhang, Z. Yan, K. Nan, D. Xiao, Y. Liu, H. Luan, H. Fu, X. Wang, Q. Yang, J. Wang, W. Ren, H. Si, F. Liu, L. Yang, H. Li, J. Wang, X. Guo, H. Luo, L. Wang, Y. Huang, J. A. Rogers, *Proc. Natl. Acad. Sci.* **2015**, *112*, 11757.

[96] W. Lee, Y. Liu, Y. Lee, B. K. Sharma, S. M. Shinde, S. D. Kim, K. Nan, Z. Yan, M. Han, Y. Huang, Y. Zhang, J. H. Ahn, J. A. Rogers, *Nat. Commun.* **2018**, *9*, 1417.

[97] R. Lakes, *Appl. Phys. Lett.* **2007**, *90*, 221905.

[98] O. G. Schmidt, K. Eberl, *Nature* **2001**, *410*, 168.

[99] Y. Mei, G. Huang, A. A. Solovev, E. B. Ureña, I. Mönch, F. Ding, T. Reindl, R. K. Y. Fu, P. K. Chu, O. G. Schmidt, *Adv. Mater.* **2008**, *20*, 4085.

[100] C. N. Saggau, F. Gabler, D. D. Karnaushenko, D. Karnaushenko, L. Ma, O. G. Schmidt, *Adv. Mater.* **2020**, *32*, 2003252.

[101] D. Singh, A. T. Kutbee, M. T. Ghoneim, A. M. Hussain, M. M. Hussain, *Adv. Mater. Technol.* **2018**, *3*, 1700192.

[102] L. P. Chia Gómez, P. Bollgruen, A. I. Egunov, D. Mager, F. Malloggi, J. G. Korvink, V. A. Luchnikov, *Lab Chip* **2013**, *13*, 3827.

[103] D. Karnaushenko, T. Kang, O. G. Schmidt, *Adv. Mater. Technol.* **2019**, *4*, 1800692.

[104] T. S. Shim, S. H. Kim, C. J. Heo, H. C. Jeon, S. M. Yang, *Angew. Chemie - Int. Ed.* **2012**, *51*, 1420.

[105] J. C. Breger, C. Yoon, R. Xiao, H. R. Kwag, M. O. Wang, J. P. Fisher, T. D. Nguyen, D. H. Gracias, *ACS Appl. Mater. Interfaces* **2015**, *7*, 3398.

[106] V. Magdanz, G. Stoychev, L. Ionov, S. Sanchez, O. G. Schmidt, *Angew. Chemie - Int. Ed.* **2014**, *53*, 2673.

[107] S. Ma, Y. Zhang, Y. Liang, L. Ren, W. Tian, L. Ren, *Adv. Funct. Mater.* **2020**, *30*, 1908508.

[108] E. Smela, O. Inganäs, I. Lundström, *Science* **1995**, *268*, 1735.

[109] L. Ionov, *Soft Matter* **2011**, *7*, 6786.

[110] L. Ionov, *Mater. Today* **2014**, *17*, 494.

[111] R. M. Erb, J. S. Sander, R. Grisch, A. R. Studart, *Nat. Commun.* **2013**, *4*, 1.

[112] A. R. Studart, R. M. Erb, *Soft Matter* **2014**, *10*, 1284.

[113] W. Fan, C. Shan, H. Guo, J. Sang, R. Wang, R. Zheng, K. Sui, Z. Nie, *Sci. Adv.* **2019**, *5*, aav7174.

[114] T. G. Leong, C. L. Randall, B. R. Benson, N. Bassik, G. M. Stern, D. H. Gracias, *Proc. Natl. Acad. Sci.* **2009**, *106*, 703.

[115] E. W. H. Jager, O. Inganäs, I. Lundström, *Science* **2000**, *288*, 2335.

[116] A. I. Egunov, Z. Dou, D. D. Karnaushenko, F. Hebenstreit, N. Kretschmann, K. Akgün, T. Ziemssen, D. Karnaushenko, M. Medina-Sánchez, O. G. Schmidt, *Small* **2021**, *17*, 2002549.

[117] M. Christophersen, B. Shapiro, E. Smela, *Sensors Actuators, B Chem.* **2006**, *115*, 596.

[118] P. Du, X. Lin, X. Zhang, *Sensors Actuators, A Phys.* **2010**, *163*, 240.

[119] D. Grimm, C. C. Bof Bufon, C. Deneke, P. Atkinson, D. J. Thurmer, F. Schäffel, S. Gorantla, A. Bachmatiuk, O. G. Schmidt, *Nano Lett.* **2013**, *13*, 213.

[120] R. Herzer, A. Gebert, U. Hempel, F. Hebenstreit, S. Oswald, C. Damm, O. G. Schmidt,

M. Medina-Sánchez, *Small* **2021**, *17*, 2005527.

[121] O. G. Schmidt, N. Schmarje, C. Deneke, C. Muandller, N. Y. Jin-Phillipp, *Adv. Mater.* **2001**, *13*, 756.

[122] R. Sharma, C. C. B. Bufon, D. Grimm, R. Sommer, A. Wollatz, J. Schadewald, D. J. Thurmer, P. F. Siles, M. Bauer, O. G. Schmidt, *Adv. Energy Mater.* **2014**, *4*, 1301631.

[123] M. Medina-Sánchez, B. Ibarlucea, N. Pérez, D. D. Karnaushenko, S. M. Weiz, L. Baraban, G. Cuniberti, O. G. Schmidt, *Nano Lett.* **2016**, *16*, 4288.

[124] Y. Lee, V. K. Bandari, Z. Li, M. Medina-Sánchez, M. F. Maitz, D. Karnaushenko, M. V. Tsurkan, D. D. Karnaushenko, O. G. Schmidt, *Nat. Commun.* **2021**, *12*, 4967.

[125] C. Becker, D. Karnaushenko, T. Kang, D. D. Karnaushenko, M. Faghih, A. Mirhajivarzaneh, O. G. Schmidt, *Sci. Adv.* **2019**, *5*, eaay7459.

[126] F. Li, J. Wang, L. Liu, J. Qu, Y. Li, V. K. Bandari, D. Karnaushenko, C. Becker, M. Faghih, T. Kang, S. Baunack, M. Zhu, F. Zhu, O. G. Schmidt, *Adv. Sci.* **2019**, *6*, 1901051.

[127] D. D. Karnaushenko, D. Karnaushenko, H. J. Grafe, V. Kataev, B. Büchner, O. G. Schmidt, *Adv. Electron. Mater.* **2018**, *4*, 1800298.

[128] P. Lepucki, A. I. Egunov, M. Rosenkranz, R. Huber, A. Mirhajivarzaneh, D. D. Karnaushenko, A. P. Dioguardi, D. Karnaushenko, B. Büchner, O. G. Schmidt, H. J. Grafe, *Adv. Mater. Technol.* **2021**, *6*, 2000679.

[129] V. K. Bandari, Y. Nan, D. Karnaushenko, Y. Hong, B. Sun, F. Striggow, D. D. Karnaushenko, C. Becker, M. Faghih, M. Medina-Sánchez, F. Zhu, O. G. Schmidt, *Nat. Electron.* **2020**, *3*, 172.

[130] P. Mucksavage, D. C. Kerbl, D. L. Pick, J. Y. Lee, E. M. Mcdougall, M. K. Louie, *J. Endourol.* **2011**, *25*, 523.

[131] G. Kofod, W. Wirges, M. Paajanen, S. Bauer, *Appl. Phys. Lett.* **2007**, *90*, 081916.

[132] T. Xu, J. Zhang, M. Salehizadeh, O. Onaizah, E. Diller, *Sci. Robot.* **2019**, *4*, eaav4494.

[133] Y. Kim, G. A. Parada, S. Liu, X. Zhao, *Sci. Robot.* **2019**, *4*, 1.

[134] W. Choi, M. Akbarian, V. Rubtsov, C. J. Kim, *IEEE Trans. Ind. Electron.* **2009**, *56*, 1005.

[135] J. Paek, I. Cho, J. Kim, *Sci. Rep.* **2015**, *5*, 10768.

[136] K. P. Ashwin, A. Ghosal, *J. Mech. Robot.* **2019**, *11*, 61004.

[137] S. Li, D. M. Vogt, D. Rus, R. J. Wood, *Proc. Natl. Acad. Sci.* **2017**, *114*, 13132.

[138] H. Zeng, O. M. Wani, P. Wasylczyk, R. Kaczmarek, A. Priimagi, *Adv. Mater.* **2017**, *29*, 1701814.

[139] P. Martins, D. M. Correia, V. Correia, S. Lanceros-Mendez, *Phys. Chem. Chem. Phys.* **2020**, *22*, 15163.

[140] A. Fannir, R. Temmer, G. T. M. Nguyen, L. Cadiergues, E. Laurent, J. D. W. Madden, F. Vidal, C. Plesse, *Adv. Mater. Technol.* **2019**, *4*, 1800519.

[141] H. S. Wang, J. Cho, D. S. Song, J. H. Jang, J. Y. Jho, J. H. Park, *ACS Appl. Mater. Interfaces* **2017**, *9*, 21998.

[142] K. Rohtlaid, L. Seurre, G. T. M. Nguyen, G. Curley, C. Soyer, S. Grondel, F. Vidal, C.

Plesse, E. Cattan, *Smart Mater. Struct.* **2020**, *29*, 09LT01.

[143] K. K. C. Lee, N. R. Munce, T. Shoa, L. G. Charron, G. A. Wright, J. D. Madden, V. X. D. Yang, *Sensors Actuators, A Phys.* **2009**, *153*, 230.

[144] E. D. Daneshvar, E. Smela, *Adv. Healthc. Mater.* **2014**, *3*, 1026.

[145] D. Melling, J. G. Martinez, E. W. H. Jager, *Adv. Mater.* **2019**, *31*, 1808210.

[146] R. H. Baughman, L. W. Shacklette, R. L. Elsenbaumer, E. Plichta, C. Becht, in Conjugated Polymeric Materials: Opportunities in Electronics, Optoelectronics, and Molecular Electronics., Springer Netherlands, Dordrecht, **1990**, pp. 559–582.

[147] E. W. H. Jager, C. Immerstrand, K. H. Peterson, K. E. Magnusson, I. Lundström, O. Inganäs, *Biomed. Microdevices* **2002**, *4*, 177.

[148] E. W. H. Jager, E. Smela, O. Inganas, *Science* **2000**, *290*, 1540.

[149] Y. Hanayama, K. Kikuchi, S. Tsuchitani, in *2011 IEEE/SICE Int. Symp. Syst. Integr.*, IEEE, **2011**, pp. 863–868.

[150] T. Shoa, J. D. Madden, N. R. Munce, V. Yang, *Polym. Int.* **2010**, *59*, 343.

[151] D. Melling, S. Wilson, E. W. H. Jager, *Smart Mater. Struct.* **2013**, *22*, 104021.

[152] D. Melling, S. A. Wilson, E. W. H. Jager, *RSC Adv.* **2015**, *5*, 84153.

[153] Y. Liu, Q. Gan, S. Baig, E. Smela, *J. Phys. Chem. C* **2007**, *111*, 11329.

[154] N. Q. Khuyen, Z. Zondaka, M. Harjo, J. Torop, T. Tamm, R. Kiefer, *Polymers.* **2019**, *11*, 849.

[155] C. M. Druitt, G. Alici, *2013 IEEE/ASME Int. Conf. Adv. Intell. Mechatronics Mechatronics Hum. Wellbeing, AIM 2013* **2013**, 373.

[156] S. W. John, G. Alici, C. D. Cook, *IEEE/ASME Trans. Mechatronics* **2010**, *15*, 149.

[157] K. Kruusamäe, A. Punning, A. Aabloo, K. Asaka, *Actuators* **2015**, *4*, 17.

[158] K. K. Leang, Y. Shan, S. Song, K. J. Kim, *IEEE/ASME Trans. Mechatronics* **2012**, *17*, 345.

[159] H. Cheng, F. Zhao, J. Xue, G. Shi, L. Jiang, L. Qu, *ACS Nano* **2016**, *10*, 9529.

[160] K. Kruusamäe, P. Brunetto, S. Graziani, A. Punning, G. Di Pasquale, A. Aabloo, *Polym. Int.* **2010**, *59*, 300.

[161] M. Pyo, C. C. Bohn, E. Smela, J. R. Reynolds, A. B. Brennan, *Chem. Mater.* **2003**, *15*, 916.

[162] S. Foong, K. M. Lee, K. Bai, *Proc. - IEEE Int. Conf. Robot. Autom.* **2010**, 5447.

[163] B. G. A. Lambrecht, H. Kazerooni, *Proc. - IEEE Int. Conf. Robot. Autom.* **2009**, 639.

[164] M. C. Carrozza, A. Persichetti, C. Laschi, F. Vecchi, R. Lazzarini, P. Vacalebri, P. Dario, *IEEE/ASME Trans. Mechatronics* **2007**, *12*, 1.

[165] J. A. Baldoni, B. B. Yellen, *IEEE Trans. Magn.* **2007**, *43*, 2430.

[166] Vehicle Detection Using AMR Sensors *Honeywell* (https://aerospace.honeywell.com/content/dam/aerobt/en/documents/ learn/products/sensors/application-notes/ AN218_Vehicle_Detection_Using_AMR_Sensors.pdf) (accessed 17. 12. 2021).

[167] HMC1021S-TR Compass IC *Honeywell* (https://www.digikey.com/en/

products/detail/honeywell-aerospace/HMC1021S-TR/334158) (accessed 17. 12. 2021).

[168] G. S. Cañón Bermúdez, H. Fuchs, L. Bischoff, J. Fassbender, D. Makarov, *Nat. Electron.* **2018**, *1*, 589.

[169] D. F. He, M. Shiwa, *Rev. Sci. Instrum.* **2011**, *82*, 094703.

[170] Y. Guo, Y. Ouyang, N. Sato, C. C. Ooi, S. X. Wang, *IEEE Sens. J.* **2017**, *17*, 3309.

[171] D. L. Partin, J. Heremans, C. M. Thrush, L. Green, *Tech. Dig. IEEE Solid-State Sens. Actuator Work.* **1992**, *115*, 35.

[172] U. Dibbern, *Sensors and Actuators* **1986**, *10*, 127.

[173] F. Rottmann, F. Dettmann, *Sensors Actuators A. Phys.* **1991**, *27*, 763.

[174] A. T. Inc, *Strain Gages* **1999**, 102.

[175] S. Yang, N. Lu, *Sensors (Basel).* **2013**, *13*, 8577.

[176] M. Li, X. Lin, *Phys. Rev. B - Condens. Matter Mater. Phys.* **2010**, *81*, 153102.

[177] M. Zhou, M. Pagels, B. Geschke, J. Heinze, *J. Phys. Chem. B* **2002**, *106*, 10065.

[178] S. Ramanavicius, A. Ramanavicius, *Polymers (Basel).* **2021**, *13*, 1.

[179] E. Smela, N. Gadegaard, *J. Phys. Chem. B* **2001**, *105*, 9395.

[180] M. Zhou, J. Heinze, *Electrochim. Acta* **1999**, *44*, 1733.

[181] S. Maw, E. Smela, K. Yoshida, P. Sommer-Larsen, R. B. Stein, *Sensors Actuators, A Phys.* **2001**, *89*, 175.

[182] M. Ohring, *A Review of Materials Science*, Elsevier, **1992**.

[183] S. Sadki, P. Schottland, N. Brodie, G. Sabouraud, *Chem. Soc. Rev.* **2000**, *29*, 283.

[184] M. Zhou, J. Heinze, *J. Phys. Chem. B* **1999**, *103*, 8451.

[185] E. W. H. Jager, O. Inganäs, in *Ref. Modul. Mater. Sci. Mater. Eng.*, Elsevier, **2016**, pp. 1–5.

[186] N. Elgrishi, K. J. Rountree, B. D. McCarthy, E. S. Rountree, T. T. Eisenhart, J. L. Dempsey, *J. Chem. Educ.* **2018**, *95*, 197.

[187] I. V. Soldatov, R. Schäfer, *Rev. Sci. Instrum.* **2017**, *88*, 073701.

[188] I. V. Soldatov, J. Zehner, K. Leistner, T. Kang, D. Karnaushenko, R. Schäfer, *J. Magn. Magn. Mater.* **2021**, *529*, 167889.

[189] F. Striggow, M. Medina-Sánchez, G. K. Auernhammer, V. Magdanz, B. M. Friedrich, O. G. Schmidt, *Small* **2020**, *16*, 2000213.

[190] A. Aziz, M. Medina-Sánchez, J. Claussen, O. G. Schmidt, *Nano Lett.* **2019**, *19*, 6612.

[191] K. Johan Åström, R. M. Murray, *Feedback Systems: An Introduction for Scientists and Engineers*, **2010**.

[192] C. Moonla, K. Y. Goud, H. Teymourian, T. Tangkuaram, J. Ingrande, P. Suresh, J. Wang, *Talanta* **2020**, *218*, 121205.

[193] B. Rivkin, C. Becker, B. Singh, A. Aziz, F. Akbar, A. Egunov, D. D. Karnaushenko, R. Naumann, R. Schäfer, M. Medina-Sánchez, D. Karnaushenko, O. G. Schmidt, *Sience Adv.* **2021**, *7*, 51, eabl5408.

[194] E. Nader, S. Skinner, M. Romana, R. Fort, N. Lemonne, N. Guillot, A. Gauthier, S. Antoine-Jonville, C. Renoux, M. D. Hardy-Dessources, E. Stauffer, P. Joly, Y. Bertrand, P. Connes, *Front. Physiol.* **2019**, *10*, 1329.

[195] J. Peltier, A. Nowtash, P. Toussaint, C. Desenclos, H. Deramond, D. Le Gars, *Neurochirurgie* **2004**, *50*, 454.

[196] E. C. Lin, *Mayo Clin. Proc.* **2010**, *85*, 1142.

[197] A. S. Narain, F. Y. Hijji, K. H. Yom, K. T. Kudaravalli, B. E. Haws, K. Singh, *World J. Orthop.* **2017**, *8*, 524.

[198] W. Su, Z. Wang, T. Wen, Z. Hu, J. Wu, Z. Zhou, M. Liu, *IEEE Electron Device Lett.* **2019**, *40*, 969.

[199] F. Armstrong, W. Teo, *Electricity and Magnetism*, Cambridge University Press, Cambridge, **2020**.

[200] A. Sorriento, M. B. Porfido, S. Mazzoleni, G. Calvosa, M. Tenucci, G. Ciuti, P. Dario, *IEEE Rev. Biomed. Eng.* **2020**, *13*, 212.

[201] *SASB/SCC39 – SCC39 – International Committee on Electromagnetic Safety, C95.1-2019 – IEEE Standard for Safety Levels with Respect to Human Exposure to Electric, Magnetic, and Electromagnetic Fields, 0 Hz to 300 GHz, IEEE, New York, 2019*

[202] B. Rivkin, C. Becker, F. Akbar, R. Ravishankar, D. D. Karnaushenko, R. Naumann, A. Mirhajivarzaneh, M. Medina-Sánchez, D. Karnaushenko, O. G. Schmidt, *Adv. Intell. Syst.* **2021**, *3*, 2000238.

[203] J. F. Shackelford, Y.-H. Han, S. Kim, S.-H. Kwon, *CRC Materials Science and Engineering Handbook*, **2016**.

[204] G. M. Spinks, L. Liu, G. G. Wallace, D. Zhou, *Adv. Funct. Mater.* **2002**, *12*, 437.

[205] E. Smela, M. Kallenbach, J. Holdenried, *J. Microelectromechanical Syst.* **1999**, *8*, 373.

[206] A. Ganguli, Y. Watanabe, M. T. Hwang, J. C. Huang, R. Bashir, *Biomed. Microdevices* **2018**, *20*, 45.

[207] J. M. Rothberg, W. Hinz, T. M. Rearick, J. Schultz, W. Mileski, M. Davey, J. H. Leamon, K. Johnson, M. J. Milgrew, M. Edwards, J. Hoon, J. F. Simons, D. Marran, J. W. Myers, J. F. Davidson, A. Branting, J. R. Nobile, B. P. Puc, D. Light, T. A. Clark, M. Huber, J. T. Branciforte, I. B. Stoner, S. E. Cawley, M. Lyons, Y. Fu, N. Homer, M. Sedova, X. Miao, B. Reed, J. Sabina, E. Feierstein, M. Schorn, M. Alanjary, E. Dimalanta, D. Dressman, R. Kasinskas, T. Sokolsky, J. A. Fidanza, E. Namsaraev, K. J. McKernan, A. Williams, G. T. Roth, J. Bustillo, *Nature* **2011**, *475*, 348.

[208] F. A. Shaik, S. Ihida, Y. Ikeuchi, A. Tixier-Mita, H. Toshiyoshi, *Biosens. Bioelectron.* **2020**, *169*, 112546.

[209] A. Tixier-Mita, S. Ihida, D. Blanchard, M. Shinohara, A. C. Eiler, G. A. Cathcart, P. M. Faure, T. Kohno, Y. Sakai, T. Lévi, H. Toshiyoshi, *IEEJ Trans. Electr. Electron. Eng.* **2019**, *14*, 1280.

[210] J. S. Park, W. J. Maeng, H. S. Kim, J. S. Park, *Thin Solid Films* **2012**, *520*, 1679.

[211] M. Nag, A. Bhoolokam, S. Smout, M. Willegems, R. Muller, K. Myny, S. Schols, M. Ameys, J. Genoe, T. H. Ke, P. Vicca, T. Ellis, B. Cobb, A. Kumar, J. L. P. J. Van Der Steen, G. Gelinck, Y. Fukui, K. Obata, G. Groeseneken, P. Heremans, S. Steudel, *J.*

Soc. Inf. Disp. **2014**, *22*, 509.

[212] K. Nomura, H. Ohta, A. Takagi, T. Kamiya, M. Hirano, H. Hosono, *Nature* **2004**, *432*, 488.

[213] E. Fortunato, P. Barquinha, R. Martins, *Adv. Mater.* **2012**, *24*, 2945.

[214] B. Bao, B. Rivkin, F. Akbar, D. D. Karnaushenko, V. K. Bandari, L. Teuerle, C. Becker, S. Baunack, D. Karnaushenko, O. G. Schmidt, *Adv. Mater.* **2021**, *33*, 2101272.

[215] C. Wang, S. J. Cho, N. Y. Kim, *Mater. Manuf. Process.* **2013**, *28*, 947.

[216] T. Gaier, P. Kangaslahti, B. Lambrigtsen, I. Ramos-Perez, A. Tanner, D. McKague, C. Ruf, M. Flynn, Z. Zhang, R. Backhus, D. Austerberry, in *2016 IEEE Int. Geosci. Remote Sens. Symp.*, IEEE, **2016**, pp. 2021–2023.

[217] R. V. Martinez, C. R. Fish, X. Chen, G. M. Whitesides, *Adv. Funct. Mater.* **2012**, *22*, 1376.

[218] D. Karnaushenko, T. Kang, V. K. Bandari, F. Zhu, O. G. Schmidt, *Adv. Mater.* **2020**, *32*, 1902994.

[219] J. Park, J. K. Kim, D. S. Kim, A. Shanmugasundaram, S. A. Park, S. Kang, S. H. Kim, M. H. Jeong, D. W. Lee, *Sensors Actuators, B Chem.* **2019**, *280*, 201.

[220] W. Lu, W. Bai, H. Zhang, C. Xu, A. M. Chiarelli, A. Vázquez-Guardado, Z. Xie, H. Shen, K. Nandoliya, H. Zhao, K. H. Lee, Y. Wu, D. Franklin, R. Avila, S. Xu, A. Rwei, M. Han, K. Kwon, Y. Deng, X. Yu, E. B. Thorp, X. Feng, Y. Huang, J. Forbess, Z. D. Ge, J. A. Rogers, *Sci. Adv.* **2021**, *7*, eabe0579.

[221] F. Akbar, B. Rivkin, A. Aziz, C. Becker, D. D. Karnaushenko, M. Medina-Sánchez, D. Karnaushenko, O. G. Schmidt, *Sci. Adv.* **2021**, 7, eabj0767

LIST OF FIGURES AND TABLES

ACKNOWLEDGEMENTS

THESES

1. Currently available small-scale surgical instruments do not offer electronic functionalities to support medical practitioners during minimally invasive surgery (MIS).

2. Upcoming intelligent instruments should compensate the lost haptic and optic feedback that is not available during MIS, compared to classical surgery, and provide further insights using integrated micro-electronics.

3. The development of electronically integrated micro-scale instruments for MIS is impeded by the prevalent fabrication paradigm that presumes the enhancement of classical surgical instruments with separately manufactured electronic components.

4. Modern strategies for micro-scale shape control can transform batch-processed micro-patterned structures into mechanically and electronically functional small-scale devices.

5. Established strategies for the self-rolling of polymer layers can be evolved to create free-standing, high aspect ratio tubular structures with integrated electronic components that can serve as platforms for electronically integrated micro-catheters.

6. Micro-catheters based on self-rolling polymer films are mechanically robust and preserve their shape and integrity after being bent.

7. The combination of various stimuli-responsive materials that are susceptible to different triggers offers strategies to develop complex micro-robotic systems, which first self-assemble from planar structures and then actuate to carry out robotic tasks.

8. Self-rolled micro-catheters can be designed to carry actuated opposing digits to efficiently manipulate microscopic objects.

9. Self-rolled micro-catheters can be connected to fluidic systems to carry out targeted fluid delivery through microscopic channels or collect fluids for liquid biopsy.

10. Self-rolled micro-catheters are sufficiently rigid to be inserted into artificial or natural channels, yet flexible enough to adjust their shape and comply to the channel geometry.

11. Available technologies using electro-magnetic reference fields to track surgical instruments within patients rely on field sensors with sizes that are not compatible with microscopic and highly flexible surgical instruments.

12. Electronically integrated micro-catheters can carry embedded magnetic sensors to detect external reference fields for position and orientation tracking.

13. Electro-magnetic coils can generate magnetic fields with a controllable spatial phase profile, which can be used for navigation with high precision.

14. The curvature of microscopic polymer sheets can be controlled with embedded CP actuators that occupy only a fraction of the available platform area and leave space for other electronic components, giving rise to reshapeable micro-electronic devices (RMEDs).

15. The efficient control of RMED curvature requires a finely balanced device geometry and layer thicknesses, which can be initially estimated using mechanical computations.

16. The curvature of RMEDs is precisely defined at an instant through the application of an appropriate bias voltage.

17. When operating PPy actuators with a digital-to-analog converter as bias voltage supply, electronic components such as smoothing capacitors should be used to prevent potential damage caused by sudden voltage changes.

18. RMEDs that naturally operated in electrolyte solutions require effective insulation layers to prevent cross-talk between electronic actuators and sensors, for instance using ALD processed metal-oxide layers.

19. RMEDs can carry magnetic sensors to monitor their orientation using rotating or specially aligned static magnetic fields.

20. Integrated strain sensors can directly measure the curvature of RMEDs.

21. Data on RMED curvature or orientation obtained from integrated sensors can be used as real-time feedback in the closed-loop PID control of PPy actuators.

22. The algorithmic control of RMED curvature using strain sensor feedback allows to detect objects in the actuation path automatically and hold actuation upon contact.

23. Feedback-controlled RMEDs with automated object detection enable the gentle manipulation of soft biological tissues, such as nerve bundles, and pave the way towards smart surgical micro-tools.

24. PPy actuators can be deposited and operated using an electronic connection that is switched by an integrated a-IGZO thin-film transistor (TFT), for instance in an active-matrix (AM) configuration.

25. The amount of individual PPy actuators, and other components, that can be integrated into a given microsystem is drastically increased when using on-board multiplexing through TFT-AM circuitry, enabling higher complexity and integration density.

LIST OF PUBLICATIONS

- Christian Becker, Bin Bao, Dmitriy D. Karnaushenko, Vineeth Kumar Bandari, **Boris Rivkin**, Zhe Li, Maryam Faghih, Daniil Karnaushenko, and Oliver G. Schmidt, 'A new dimension for magnetosensitive e-skins: Active matrix integrated micro-origami sensor arrays', *Nature Communications*, 13, 2121, 2022

- **Boris Rivkin**, Christian Becker, Balram Singh, Azaam Aziz, Farzin Akbar, Aleksandr Egunov, Dmitriy D. Karnaushenko, Ronald Naumann, Rudolf Schäfer, Mariana Medina Sánchez, Daniil Karnaushenko, Oliver G. Schmidt, 'Electronically integrated micro-catheters based on self-assembling polymer films', *Science Advances*, 7, 51, eabl5408, 2021.

- Farzin Akbar, **Boris Rivkin**, Azaam Aziz, Christian Becker, Dmitriy D. Karnaushenko, Mariana Medina Sánchez, Daniil Karnaushenko, and Oliver G. Schmidt, 'Self-sufficient self-oscillating microsystem driven by low power at low Reynolds numbers', *Science Advances*, 7, 44, eabj0767, 2021.

- Bin Bao, **Boris Rivkin**, Farzin Akbar, Dmitriy D. Karnaushenko, Vineeth Kumar Bandari, Laura Teuerle, Christian Becker, Stefan Baunack, Daniil Karnaushenko, and Oliver G. Schmidt, 'Digital Electrochemistry for On-Chip Heterogeneous Material Integration', *Advanced Materials*, 33, 26, 2101272, 2021.

- **Boris Rivkin**, Christian Becker, Farzin Akbar, Rachappa Ravishankar, Dmitriy D. Karnaushenko, Ronald Naumann, Alaleh Mirhajivarzaneh, Mariana Medina-Sánchez, Daniil Karnaushenko, and Oliver G. Schmidt, 'Shape-Controlled Flexible Microelectronics Facilitated by Integrated Sensors and Conductive Polymer Actuators', *Advanced Intelligent Systems*, 3, 6, 2000238, 2021.